

Study the Effect of High Temperature Firing  
Process on Passivation Mechanism of  
Hydrogenated Amorphous  $SiN_x : H$  Layers with  
Focus on Hydrogen Effusion Measurements

Dissertation

zur Erlangung des Doktorgrades der Naturwissenschaften  
(Dr. rer. nat.)

der

Naturwissenschaftlichen Fakultät II  
Chemie, Physik und Mathematik

der Martin-Luther-Universität  
Halle-Wittenberg

Vorgelegt von

Frau Sahar Lausch (geb. Jafari)

Gutachter: Prof. Dr. Jörg Schilling, Prof. Dr. Ralf Wehrspohn,  
Prof. Dr. Johannes Heitman

Verteidigungsdatum: 27.09.2023



# Contents

|          |   |           |
|----------|---|-----------|
| <b>1</b> | <b>Introduction</b>   | <b>1</b>  |
| <b>2</b> | <b>Physical Fundamentals</b>                                | <b>5</b>  |
| 2.1      | Carrier recombination in crystalline silicon . . . . .      | 5         |
| 2.1.1    | Bulk recombination . . . . .                                | 6         |
| 2.1.2    | Surface recombination . . . . .                             | 7         |
| 2.2      | Surface passivation . . . . .                               | 9         |
| 2.3      | Hydrogenated amorphous silicon nitride . . . . .            | 9         |
| 2.3.1    | Chemical passivation . . . . .                              | 9         |
| 2.3.2    | Field-effect passivation . . . . .                          | 10        |
| 2.4      | Hydrogen in silicon . . . . .                               | 11        |
| <b>3</b> | <b>Experimental Methods</b>                                 | <b>13</b> |
| 3.1      | Substrate preparation . . . . .                             | 13        |
| 3.2      | Plasma-enhanced chemical vapor deposition (PECVD) . . . . . | 13        |
| 3.3      | Reactive ion etching (RIE) process . . . . .                | 14        |
| 3.4      | Rapid thermal anneal (RTA) process . . . . .                | 15        |
| 3.5      | DC Magnetron sputtering deposition . . . . .                | 16        |
| <b>4</b> | <b>Characterization Methods</b>                             | <b>17</b> |
| 4.1      | Fourier-transform infrared (FTIR) spectroscopy . . . . .    | 17        |
| 4.2      | Spectroscopic ellipsometry (SE) . . . . .                   | 18        |
| 4.3      | Photoconductance carrier lifetime tester . . . . .          | 19        |
| 4.4      | Capacitance-Voltage (C-V) measurements . . . . .            | 20        |
| 4.5      | Scanning electron microscopy (SEM) . . . . .                | 21        |
| <b>5</b> | <b>Effusion Mass Spectroscopy for PV Applications</b>       | <b>23</b> |
| 5.1      | Introduction . . . . .                                      | 23        |
| 5.1.1    | Aim of this work . . . . .                                  | 23        |
| 5.1.2    | State of the literature . . . . .                           | 23        |
| 5.2      | Development of effusion mass spectroscopy . . . . .         | 25        |
| 5.2.1    | System setup . . . . .                                      | 25        |
| 5.2.2    | Functional principles . . . . .                             | 26        |
| 5.2.3    | Data analysis . . . . .                                     | 26        |

|          |  |           |
|----------|--|-----------|
| 5.3      | Comparison of the effusion measurement with the rapid thermal firing process . . . . .   | 30        |
| 5.4      | Comparison of effusion mass spectroscopy with other established methods . . . . .  | 32        |
| 5.4.1    | Quantitative comparison with nuclear reaction analysis (NRA) . . . . .   | 32        |
| 5.4.2    | The advantages and the limits of effusion mass spectroscopy . . . . .  | 35        |
| 5.5      | Occurrence of hydrogen spikes and its correlation with void structure . . . . .  | 37        |
| 5.5.1    | Observation of sharp peak (SP) in effusion spectra of $a-Si_x:H$ . . . . .   | 37        |
| 5.5.2    | Discussion and modeling . . . . .  | 38        |
| <b>6</b> | <b>Investigation and Characterization of Amorphous <math>SiN_x:H</math> Passivation Layers Regarding Its Applications for Si Solar Cells</b> | <b>43</b> |
| 6.1      | Understanding the properties of PECVD deposited $SiN_x:H$ passivation layers . . . . .   | 43        |
| 6.1.1    | Results . . . . .  | 43        |
| I        | The study of deposition parameters by using Design of Experiment (DoE) . . . . .   | 43        |
| II       | The influence of gas flow ratio ( $R$ ) on $SiN_x:H$ properties . . . . .  | 45        |
| III      | The influence of substrate temperature ( $T_S$ ) on properties of $SiN_x:H$ layer . . . . .  | 51        |
| 6.1.2    | Discussion . . . . .   | 55        |
| I        | The influence of the two significant deposition parameters, $R$ and $T_S$ , on $SiN_x:H$ properties . . . . .                                | 55        |
| II       | Study of the hydrogen transport mechanisms in various $SiN_x:H$ layers . . . . .   | 60        |
| III      | Three major types of $SiN_x:H$ layers based on the film structure and compositional analysis . . . . .                                       | 64        |
| 6.2      | Examples of using hydrogen effusion measurements for PV applications . . . . .   | 73        |
| 6.2.1    | Composition-limited hydrogen effusion of $SiN_x:H$ layers stack <sup>[1]</sup> . . . . .   | 73        |
| I        | Results . . . . .  | 74        |
| II       | Discussion . . . . .   | 77        |
| 6.2.2    | Understanding LeTID in Si wafers using hydrogen effusion measurements <sup>[2]</sup> . . . . .   | 79        |
| I        | Experimental . . . . .   | 79        |
| II       | Results . . . . .  | 81        |
| III      | Discussion . . . . .   | 83        |
| <b>7</b> | <b>Impact of Plasma Texturing on Passivation Mechanism of <math>SiN_x:H</math> Layers</b>  | <b>89</b> |
| 7.1      | Motivation . . . . .   | 89        |
| 7.2      | Passivation of plasma-textured silicon wafers by $SiN_x:H$ layers . . . . .  | 90        |
| 7.2.1    | Fabrication of black Si using ICP+CCP processes . . . . .  | 90        |
| 7.2.2    | The influence of various gas flow ratio $R$ on passivation quality . . . . .   | 90        |
| 7.2.3    | The influence of various deposition temperature $T_S$ on $SiN_x:H$ passivation quality . . . . .   | 93        |
| 7.2.4    | Passivation of black Si surfaces by stack structure of $SiN_x:H$ layers . . . . .  | 94        |

---

|          |  |            |
|----------|--|------------|
| 7.3      | Discussion . . . . .   | 95         |
| 7.3.1    | Degradation of passivation quality of $SiN_x:H$ induced by surface texturing             | 95         |
|          | <i>I</i> Plasma-induced defects and impurities . . . . .                                 | 96         |
|          | <i>II</i> Effective surface enhancement . . . . .  | 97         |
| 7.3.2    | Mechanism of hydrogen release from $SiN_x:H$ layers deposited on black silicon . . . . . | 99         |
| 7.3.3    | Conclusion and outlook . . . . .   | 100        |
| <b>8</b> | <b>Summary</b>   | <b>101</b> |
| <b>A</b> | <b>Appendix</b>  | <b>105</b> |
|          | List of Figures . . . . .  | i          |
|          | List of Tables . . . . .   | vii        |
|          | Bibliography . . . . .   | xviii      |
|          | Abbreviations and Nomenclature . . . . .   | xix        |
|          | Acknowledgement . . . . .  | xxii       |
|          | List of Publications . . . . .   | xxiv       |
|          | Curriculum Vitae . . . . .   | xxvi       |



# Chapter 1

## Introduction

The United Nation (UN) reported in 2019 that after one century and a half of industrialization and large scale of agriculture and corresponding explosion of population, quantity of greenhouse gases in atmosphere have risen to record level not been seen within last three million years [3]. In October 2018, the Intergovernmental Panel on Climate Change (IPCC) published a report on the impacts of global warming of 1.5 °C including increase of oceans temperature, diminishing amounts of snow and ice and rise of sea levels. One of the measures needed to slowdown the global warming is to replace the fossil fuels with renewable energy sources. In 2020 renewable energy sources together covered 46 % of total electricity consumption in Germany including 9.3 % from photovoltaics (PV), with electricity output of 50 TWh [4].

Currently, 95 % of the PV market consists of silicon solar cells, with cell efficiency growing from 1 % in 1941 [5] to the record of about 26.5 % with heterojunction (HJT) solar cells in 2018 [6]. In parallel, the sharpest reduction of solar-generated electricity was observed over the last decade (2010-2019) by 82 % from 0.378 USD/KWh to 0.068 USD/KWh [7]. This includes 13 % reduction only in year 2019, which further boosts the position of photovoltaics as the most cost-effective energy source in the renewable energy sector.

Besides the rapid developments, PV technology still faces some existing challenges. The presence of defects and impurities on the surface or in the bulk of silicon is a major problem that suppresses the efficiency of solar cells through increased charge carrier recombination. Deactivation of the defects is therefore of great importance and can be achieved by the so-called passivation processes. Hydrogen is presumably the passivation species that can interact with almost all impurities, saturate the dangling bonds and form recombination-inactive complexes.

A source of hydrogen for Si solar cells is the hydrogenated silicon nitride ( $SiN_x : H$ ) film which is widely used as anti-reflective coating (ARC) due to its adjustable optical properties.  $SiN_x : H$  films deposited by direct plasma enhanced chemical vapor deposition (PECVD) technique can include up to 40 % of hydrogen [8] and also act as passivation layers. After deposition of the  $SiN_x : H$  layer, the solar cells undergo a rapid thermal annealing (RTA) process to form the front metal contacts also known as co-firing process. The high temperature during the firing process activates the hydrogen present in the silicon nitride for

further passivation of defects at the surface or in the bulk of Si. This property of  $SiN_x : H$  has led to many studies characterizing the hydrogen bonding configuration in silicon nitride as an amorphous material to gain better insight into the mechanism of hydrogen diffusion and passivation during firing [9] [10] [11]. The diffusivity of hydrogen can be influenced by different factors such as temperature, crystallography or concentration of defects. The hydrogen diffusion in silicon is relatively fast with diffusion coefficient of  $1.7 \times 10^{-4} \text{ cm}^2/\text{s}$  at  $1000 \text{ }^\circ\text{C}$  [12] [13].

With all extensive studies on the properties of hydrogen and its interactions in last decades, yet the mechanism of hydrogen passivation and its relation to the material structure are not fully understood. The problem arises from, (i) the difficulty of measuring and detecting hydrogen as the lightest element (ii) the possibility of atomic hydrogen interacting with the silicon lattice and all impurities and defects and (iii) at the same time many different reactions occur during solar cell production such as the RTA process.

The first problem requires highly sensitive methods for the detection of hydrogen, which are generally not widely available and are costly. Development of a laboratory accessible method with high sensitivity for hydrogen detection is necessary. For the other two issues, studying the composition of the host material, such as the  $SiN_x : H$  film is essential to track and model the hydrogen behavior at high temperatures such as the firing process in the PV production. Film structure and density as well as hydrogen bond configuration play important roles in diffusion mechanism of hydrogen. Furthermore, the type and the origin of the defects such as surface dangling bonds, plasma-induced defects or impurities in the bulk must be considered. In addition to a detailed compositional study, a temperature-dependent measurement method can be useful for analyzing the firing process and its influence on the passivation mechanism of hydrogen.

Therefore, this study was aimed to investigate the following objectives:

### Objectives of this work

1. In order to measure and detect hydrogen, a simplified effusion measurement setup was developed. It has to be proven (i) whether the measurement system can be used for accurate detecting of hydrogen and (ii) whether it is possible to use the effusion mass spectroscopy to study the hydrogen behavior during the firing process, although the time scales of the two processes are different.
  - Hypothesis (1): Since the diffusion of hydrogen is strongly material and temperature dependent and due to the reported quasi-instantly diffusion rate of hydrogen in silicon at high temperatures [13], the comparison of hydrogen effusion content at a constant heating rate can be compared with the hydrogen effusion content during RTA process.
2. As explained earlier,  $SiN_x : H$  layers are a source of hydrogen and used to passivate interfacial and bulk defects. Therefore, it is crucial to understand the role of the



stoichiometry and composition of the  $SiN_x : H$  layer on hydrogen passivation mechanism after deposition and during the firing process.

- Hypothesis (2a): More hydrogen in the layer can lead to greater improvement in effective carrier lifetime after firing due to further passivation of defects.
  - Hypothesis (2b): Stacked layers of  $SiN_x : H$  with low density hydrogen-rich films on top of Si and high density film as cap layer can improve the quality of passivation by avoiding hydrogen out-diffusion at firing temperatures and allowing more hydrogen to diffuse into the interface or bulk of Si.
3. In order to increase the efficiency of silicon solar cells plasma texturing is a state of art method to reduce the light reflectivity due to the optimal light transfer in the nanostructured surface. However, due to the strongly increase of the surface area and the defects induced by the plasma process, the surface recombination rate increases drastically. Thus, the quality of surface passivation is of great importance. As mentioned before, it is known that hydrogen plays a key role on the passivation of defects, dangling bonds and impurities. In this sense, we intend to investigate whether the increase of the surface area through the plasma texturing and the subsequent increase of the volume of the  $SiN_x : H$  layer leads to a higher hydrogen effusion and if this process influences the effective charge carrier lifetime.
- Hypothesis (3a): The increased of surface area due to the plasma texturing increases the amount of hydrogen. This leads to an improvement in passivation quality after firing due to an increased amount of hydrogen in  $SiN_x : H$  layer.
  - Hypothesis (3b): The increase in surface recombination rate due to the high concentration of plasma-induced defects and the surface enlargement cannot be overcome by the increased amount of hydrogen.

### Structure of this work

This dissertation is comprised of 8 chapters.

Chapter 1 presents the motivation for this thesis, including the necessity of renewable energies and particularly solar photovoltaics. Furthermore, the objectives and the structure of the dissertation are presented.

Chapter 2 provides the physical fundamentals regarding the carrier recombination at the surface and the bulk of silicon solar cells and the role of passivation layers. Furthermore, an overview of relevant literature is presented to provide a brief history, key behaviors, hypothesized models for hydrogen passivation in  $SiN_x : H$  layers.

Chapter 3 summarizes the methodologies used for the preparation of the samples including the cleaning processes, plasma texturing and plasma deposition processes.

Chapter 4 provides an overview on characterization methods namely, Fourier transform IR (FTIR) spectroscopy, optical ellipsometry, quasi-steady-state photoconductance (QSSPC) decay and C-V characteristics.

In Chapter 5, a new setup of effusion mass spectroscopy developed for investigating the

hydrogen effusion from  $SiN_x : H$  passivation layers during the firing process is studied. It is compared with other commonly used methods and its advantages and limitations are discussed. During comparison of this method with nuclear reaction analysis (NRA), it is found that the sharp peaks in the effusion spectra is correlated with enhanced surface damage, for which a model is proposed. It is also shown that effusion measurements carried out at a constant heating rate can be compared to rapid thermal annealing, since the effusion/diffusion of hydrogen is strongly temperature dependent.

Chapter 6 presents a systematic analysis of PECVD-deposited  $SiN_x : H$  passivation films, investigating the role of deposition parameters on the compositional, optical and electrical properties of the films. Two significant deposition factors, gas flow ratio  $R$  and substrate temperature  $T_S$ , are further studied. The results lead to identify three groups of  $SiN_x : H$  films, (I) Si rich, (II) medium SiN, and (III) N rich films. Based on these results, layers stack of different  $SiN_x : H$  groups are prepared and the passivation quality and effusion mechanism are examined and compared with the single layers.

In Chapter 7, plasma-textured black silicon wafers are prepared and passivated by  $SiN_x : H$  layers. The results are compared with the planar counterparts presented in chapter 6. The possible reasons for the reduction of passivation quality such as the effective surface enhancement and the plasma induced defects are discussed.

In Chapter 8, a summary of the work is given and some potentials for future work are presented.

## Chapter 2

# Physical Fundamentals

*In this chapter, an overview of physical principles related to the surface recombination rate and passivation mechanisms by  $SiN_x : H$  is presented.*

### 2.1 Carrier recombination in crystalline silicon

Recombination is referred to the physical process that is responsible for the carrier recovery to thermal equilibrium after the semiconductor is exposed to excess carriers. Recombination can occur at the surface or in the bulk of the semiconductor. As the main concern of this work is the  $Si/SiN_x : H$  interface, the focus is on interface recombination mechanisms.

#### Definitions

In a semiconductor, the transition of an electron from the conduction band to the valance band is called recombination. The excess energy from this transition can generate a photon, a phonon or other electrons. In thermal equilibrium, the concentration of electrons  $n_0$  in the conduction band times the concentration of holes in the valance band  $p_0$  is constant and equal to [14],

$$n_i^2 = n_0 p_0 \quad (2.1)$$

with  $n_i$  being the intrinsic carrier density. External light radiation with energies above the band gap of the semiconductor can excite the electrons from valance bod to conduction band and generate additional electron-hole pairs called excess carriers  $\Delta n = n - n_0$  and  $\Delta p = p - p_0$ . When  $\Delta n \gg n_0$ , the recombination rate  $R$  is then given by [14],

$$R = \frac{\partial \Delta n(t)}{\partial t} \quad (2.2)$$

Therefore, the charge carrier lifetime is then defined as

$$\tau = \frac{\Delta n(t)}{R} \quad (2.3)$$

which is known as charge carrier lifetime. The term "minority charge carrier lifetime" is used frequently in doped semiconductors to highlight the impact of the minority charge carrier recombination in low injection levels.

### 2.1.1 Bulk recombination

The effective carrier lifetime  $\tau_{eff}$  is determined by all recombination processes occurring in a semiconductor. These are intrinsic processes (radiative and Auger recombination) which also occur in high quality crystals and extrinsic processes by impurities and defects (Shockly-Reed-Hall (SRH) recombination). A schematic of the recombination processes in a semiconductor out of thermal equilibrium is shown in Figure 2.1.

Radiative recombination or band-band recombination is the inverse process to the generation

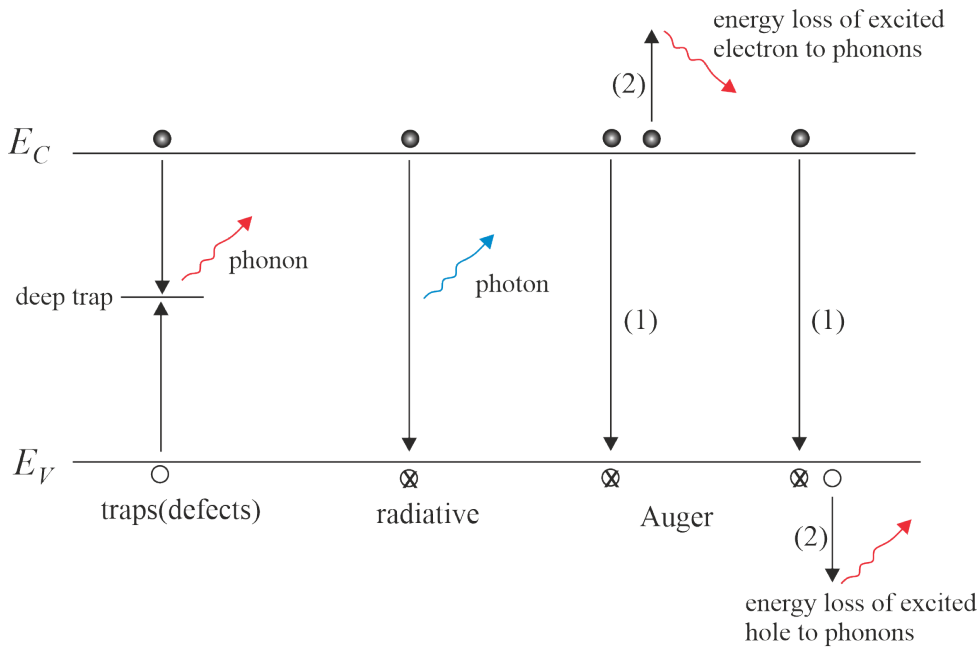


Figure 2.1: Different recombination processes in semiconductor.

of electron-hole pairs and is more strong in direct band gap semiconductors.

$$e + h \longrightarrow \gamma(\text{photon}) \quad (2.4)$$

The generation rate of photons ( $G_\gamma$ ) are equal to the recombination rate of electrons ( $R_e$ ) and holes ( $R_h$ ). The radiative recombination is then give by [14],

$$G_\gamma = R_e = R_h = B(pn - n_i^2) \quad (2.5)$$

where  $B$  is the material specific radiative recombination constant,  $n$  and  $p$  are the concentration

of electrons and holes, respectively. In n-type semiconductor ( $n \approx n_0 \gg p_0$ ), the radiative lifetime can be determined by [14]

$$\tau_{rad} = \frac{1}{n_0 B} \quad (2.6)$$

A similar equation can be written for p-type semiconductors.

Auger recombination is very similar process to radiative recombination with the difference that another charge carrier is generated in either valance or conduction band by the transition energy. The Auger recombination rate is [14]

$$R_{Auger} = (C_n n + C_p p)(pn - n_i^2). \quad (2.7)$$

This rate increases with higher doping concentration in the semiconductor. In n-type material with low injection the auger lifetime is determined by [14],

$$\tau_{Auger} = \frac{1}{C_n n_0^2} \quad (2.8)$$

The SRH recombination rate through a single defect level at energy level of  $E = E_T$  is given by

$$R_{SRH} = \frac{pn - n_i^2}{\tau_{SRH,n}(p + n_i e^{(E_i - E_T)/kT}) + \tau_{SRH,p}(n + n_i e^{(E_T - E_i)/kT})} \quad (2.9)$$

where  $E_i$  is Fermi energy in an intrinsic semiconductor and  $\tau_{SRH}$  is the carrier lifetime. The carrier lifetime is determined by,

$$\tau_{SRH} = \frac{1}{\sigma v_{th} N_T} \quad (2.10)$$

where  $\sigma$  is the capture cross section of traps,  $v_{th}$  the thermal velocity of the charge carriers and  $N_T$  is the concentration of the traps. Therefore, the increase of trap concentration increases the probability of carrier interaction with the traps which reduces the carrier lifetime.

In sum up, all of these recombinations can occur in parallel and thus the effective charge carrier lifetime for a doped semiconductor can be determined by

$$\frac{1}{\tau_{eff}} = \frac{1}{\tau_{rad}} + \frac{1}{\tau_{Auger}} + \frac{1}{\tau_{SRH}}. \quad (2.11)$$

### 2.1.2 Surface recombination

At the surface of a silicon wafer, where the crystal network is abruptly terminated, there are high concentration of recombination active centers. The difference to the SRH recombination in the bulk is the continuous distribution of surface states within the band gap as shown in Figure 2.2. By assuming that the transition between the states is negligible and there is only

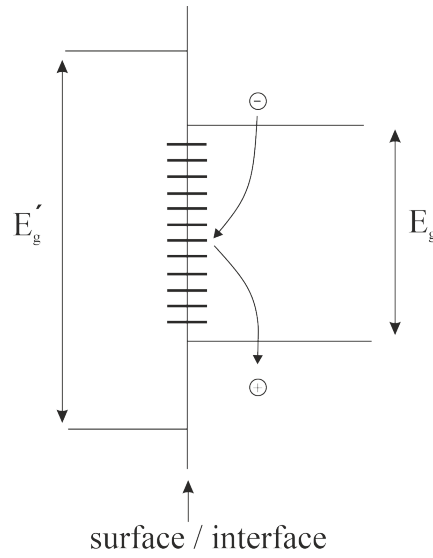


Figure 2.2: Illustration of surface states at the surface of silicon with band gap of  $E_g$  at its interface with dissimilar materials such as  $SiNx_H$  with  $E'_g$ .

the transition through the band edges, the surface recombination rate ( $R_s$ ) can be calculated from the so-called *extended Shockley-Reed-Hall* formalism [15] [16]

$$R_s = (p_s n_s - n_i^2) \int_{E_V}^{E_C} \frac{v_{th} D_{it}(E)}{(p_s + p_1(E))/\sigma_n(E) + (n_s + n_1(E))/\sigma_p(E)} dE, \quad (2.12)$$

where  $n_1(E)$  and  $p_1(E)$  are the number of electron (hole) in the condition band (valance band) in the case of Fermi level falls to trap energy  $E$  and are defined by [15],

$$n_1(E) = n_i \exp\{(E - E_i)/kT\} \quad (2.13)$$

$$p_1(E) = n_i \exp\{(E_i - E)/kT\} \quad (2.14)$$

and  $n_s$  and  $p_s$  are the concentration of electron and holes at the surface,  $D_{it}$  is the surface states density per energy interval ( $cm^{-2}eV^{-1}$ ) and  $\sigma_n$  and  $\sigma_p$  are respectively the capture cross section of electrons and holes. Since  $R_s$  is the surface recombination rate per unit area, the term "surface carrier lifetime" is not applicable and instead a surface recombination velocity (SRV) is defined by

$$S = \frac{R_s}{\Delta n_s} \quad (2.15)$$

where  $\Delta n_s = n_s - n_{s0} \approx p_s - p_{s0}$  presents the excess carrier density at the surface. Therefore, from 2.12 and 2.15, SRV can be calculated from,

$$S = (p_0 + n_0 + \Delta n_s) \int_{E_V}^{E_C} \frac{v_{th} D_{it}}{(p_0 + p_1 + \Delta n_s)/\sigma_n + (n_0 + n_1 + \Delta n_s)/\sigma_p} dE \quad (2.16)$$

## 2.2 Surface passivation

Dangling bonds or defects states at the surface of semiconductors can capture the carriers and accelerate the recombination rate similarly to what is caused by defects in the bulk. The passivation of defects is carried out by two mechanisms, (1) reducing the surface state density called *chemical passivation* and (2) applying an electric field in order to repulse the minority charge carriers at the surface of semiconductor which is known as *field-effect passivation*. Based on the equation 2.16, the SRV depends on the excess carrier densities ( $\Delta n$ ) and the doping concentration. Figure 2.3 shows the influence of each passivation mechanism on SRV. As shown, the SRV can be suppressed by the following: (i) decrease of the defect states at the interfaces ( $D_{it}$ ) (chemical passivation) and (ii) reducing the concentration of minority carriers at the interface (field effect passivation). Hydrogenated amorphous  $SiN_x$  films are widely used as passivation layers meeting both passivation mechanisms, chemical and field-effect passivation.

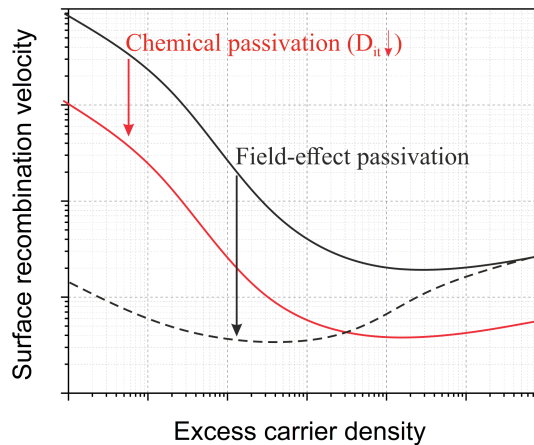


Figure 2.3: Impact of two mechanisms of passivation (1) chemical passivation of surface states  $D_{it}$  (red line) and (2) field-effect passivation (dashed line) [17].

## 2.3 Hydrogenated amorphous silicon nitride

Plasma deposited silicon nitride has been widely used in microelectronics device fabrication as isolation, encapsulating and passivation layer in silicon circuits for many decades. In 1981, for the first time Hezel and Schörner has applied plasma deposited  $SiN_x : H$  on silicon solar cells due to its capability of high passivation quality as well as suitable anti-reflecting properties [18]. Passivation of defects by  $SiN_x : H$  layers is the result of both chemical and field-effect passivation which will be shortly introduced here.

### 2.3.1 Chemical passivation

For achieving good quality passivation it is necessary to produce a chemical inert silicon film and to reduce the density of states at the surface. In  $SiN_x : H$ , the amount of  $Si-H$  bonds

are reported to be a good scale for a successful passivation of silicon dangling bonds [10]. Si-rich silicon nitride layers with high concentration of  $Si-H$  are often reported as a promising passivation layer. However, in some reports, high quality surface passivation is also achieved by stoichiometric  $SiN_x:H$  films, which are optically more suitable for low reflectivity [19]. Plasma deposited  $SiN_x:H$  films contain up to 40 % of hydrogen which is known to be released during the post firing process that forms the metal contacts. This hydrogen can either effuse in the ambient or diffuse into the underlying Si substrate. There are several reports [20] [21] [22] that show the importance of hydrogen in passivation of defects at silicon surface or in the bulk. Since hydrogen atoms are small they can easily diffuse and saturate the dangling bonds and form  $Si-H$  bonds without large distortion of the lattice. The diffusivity of hydrogen in silicon is relatively fast [13] but it is strongly affected by many factors such as temperature, crystallographic defects and the concentration of different impurities. Hydrogen concentration influence the film composition and particularly the  $Si/N$  ratio in the  $SiN_x:H$  layer [23]. The film composition is therefore an effective factor for achieving high quality passivation and can be determined for example by measuring the refractive index  $n$  of  $SiN_x:H$  layer [24].

### 2.3.2 Field-effect passivation

The other possibility to decrease the density of surface recombination centers is to reduce the charge carrier density at the surface by applying an electric field. At the interface of  $Si/SiN_x:H$ , the energy bands of silicon bend towards the surface is due to the surface potential ( $\psi_s$ ) caused by positive fixed charges. The presence of silicon dangling bond defects with three nitrogen back bonds at (or near) the  $Si/SiN_x:H$  interface is responsible for the positive fixed charges ( $Q_f$ ) which are known as  $K^+$  centers [25] [26]. Schmidt et al. assumed that this defect is located slightly below the Si conduction band edge as it is schematically shown in Figure 2.4 [26]. The positive fixed charges at the surface of n-type silicon (phosphor-doped) repel holes in the valance band and absorb electrons in the conduction band. The collection of electrons at the surface leads to band bending downwards with surface potential of  $\psi_s$ . The model includes the native oxide layer on the Si surface which is not properly etched before deposition of  $SiN_x:H$ .

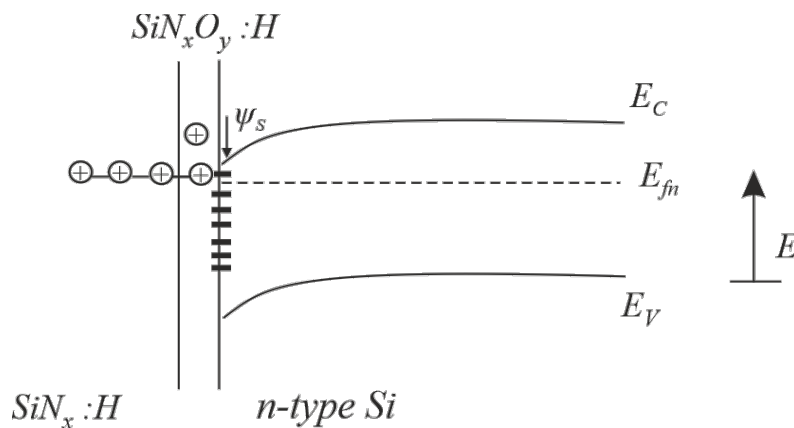


Figure 2.4: A schematic of the band bending at the interface of  $Si/SiN_x:H$  in thermal equilibrium (in dark) due to the positive fixed charges related to  $K^+$  centers [26].



## 2.4 Hydrogen in silicon

The presence of atomic hydrogen in crystalline or amorphous semiconductors can alter the electrical and optical properties. Hydrogen is presumably the passivating species, reacting with dangling and defective bonds and forming complexes with impurities. Hydrogen can be inserted into the semiconductor via processes like hydrogen implantation, hydrogen-containing plasma or chemical reaction at the surface of the material. In silicon, the equilibrium state of hydrogen in the perfect lattice is the tetrahedral interstitial site  $T_d$  calculated from extended Huckel theory by Singh et al [27]. It was also found that the bonded hydrogen has a comparatively lower energy than the free hydrogen, so saturation of dangling bonds or defects is favorable. Hydrogen at low temperatures in silicon can be found in three states [28]: (1) hydrogen bonded to the dangling bonds that form  $Si-H$  bonds, giving rise to the stretching mode that can be observed in IR absorption spectra at  $1800 - 2300 \text{ cm}^{-1}$  [29]. This is the lowest energy state of any hydrogen bonds [28]. (2) Molecular  $H_2$ , which can occur in the absence of defects and is optically and electrically inactive, occupying the  $T_d$  state at thermal equilibrium. (3) The atomic hydrogen, found in the so-called  $M$  state, which is the lowest-energy state for unbound hydrogen. The first two states are dominant at low temperatures and therefore the hydrogen is immobile during thermal equilibrium. While, at high temperature above approximately  $700 \text{ }^\circ\text{C}$  the atomic hydrogen predominates when the bonds break and the diffusivity is substantially higher [28].

Many of the electrically-active impurities in Si can be neutralized by hydrogen. Impurities such as Au, Fe, Cu and Ni can diffuse in silicon bulk during different growth processes at high temperatures. However, their solubility at certain temperatures are low but they are enough to act as recombination centers and degrade the device performance. The passivation of impurities by hydrogen depends on the density of sites where hydrogen can bond. In case of deep level defects, both donors and acceptors can be passivated by atomic hydrogen. About 99 % of shallow acceptors such as B, Al, In and Ga can be deactivated by the atomic hydrogen reactions at temperatures higher than  $100 \text{ }^\circ\text{C}$ . However, very low number of shallow donors are passivated after exposure to atomic hydrogen.

Hydrogen can be found in three charge states,  $H^+$ ,  $H^-$  and  $H^0$  [30]. Regarding different charge states and interactions, they show various mobility in silicon. For example,  $H^0$  is not affected by the electric fields or other charged defects and shows diffusivity about five order of magnitude higher than  $H^+$  [31]. It is emphasized that the hydrogen in form of  $H^+$  species deactivate the acceptors ( $A^- + H^+ \rightarrow (AH)^0$ ) which is confirmed by the donor state of hydrogen in upper half of Si band gap [32]. While passivation of donors occurs due to high level of neutral hydrogen  $H^0$  in n-type silicon ( $D^+ + e^- + H^0 \rightarrow (DH)^0$ ) [33]. However, the passivation of donors by hydrogen is limited due to large formation of molecular hydrogen through the reaction  $H^0 + H^0 \rightarrow H_2$ .

At the surface of silicon, atomic hydrogen forms various bonds such as  $SiH$ ,  $SiH_2$  and  $SiH_4$  [34] [35] resulting from chemisorption of hydrogen at different temperatures or decomposition of surface structure (breaking  $Si-Si$  bonds). At temperature about  $300 \text{ }^\circ\text{C}$  most hydrogen is in form of  $SiH$  with higher thermal stability and at temperatures above that,

hydrogen starts to desorb from  $SiH$  bonds and effuse from the surface [28].

The interest of hydrogen diffusion in silicon arose from 1970s with different model describing the dynamics of hydrogen. One of first quantitative studies was carried out by Van Wieringen and Warmoltz [12] that determined the diffusion coefficient of hydrogen ( $D_H$ ) in silicon cylinder at temperature of 970-1200 °C by using mass spectroscopic analysis,

$$D_H = 9.4 \times 10^{-3} \exp \frac{-0.48 (eV)}{kT} (cm^2 s^{-1}) \quad (2.17)$$

The calculation was based on the pressure-dependent permeation of hydrogen and showed that hydrogen in silicon exists in forms of  $H^0$ ,  $H^+$  and bound hydrogen. Later, Pearton et al. [28] calculated the diffusion of hydrogen in doped silicon. In p-type Si, hydrogen was found in form of  $H^0$  and  $H^+$ , depending on the sample temperature and doping concentration. The permeation of  $H^+$  can be interfered by trapping of acceptors ( $A^-$ ). At high temperatures ( $> 300$  °C),  $H^0$  was the dominant specie without trapping by acceptors and its high concentration leads to the formation of  $H_2$  molecules during diffusion. In n-type Si, the hydrogen is in the form of  $H^0$  and therefore there is a great amount of  $H_2$  formation, resulting in low diffusion of hydrogen compared to p-type silicon. Consequently, the charge state control of hydrogen can lead to successful passivation of defects at high temperatures as suggested by Hallam et al. [20]. In a model described by Sopori et al., hydrogen atoms can be trapped during low temperature film deposition by the defects at the Si surface which is called process-induced trap and later they are detrapped during rapid thermal annealing (RTA) processes [21]. The Model explains the effect of various trapping processes on the hydrogen profile in Si.

## Chapter 3

# Experimental Methods

*The aim of this chapter is to provide an overview on selection of samples, preparation and processing methods.*

### 3.1 Substrate preparation

Double-side polished 6" phosphor-doped n-type Float Zone-Si (Fz-Si) wafers of resistivity  $\sim 1 - 6 \Omega.cm$  and thickness  $\sim 250 \mu m$  are selected as substrates for deposition and optimization of  $SiN_x : H$  films (section 6.1). Commercial iso-textured 156 mm x 156 mm boron-doped p-type Czochralski-Si (Cz-Si) wafers of resistivity  $\sim 1 \Omega.cm$  and thickness  $\sim 180 \mu m$  and mc-Si wafers of resistivity  $\sim 1.6 \Omega.cm$  and thickness  $\sim 180 \mu m$  are used for testing LeTID by hydrogen effusion spectroscopy (section 6.2.2).

The wafers are cleaned using the standard Radio Corporation of America (RCA) 1 and 2 processes [36], followed by a short hydrofluoric acid (HF) dip to remove any oxides from the surfaces. RCA 1 is used to remove the organic impurities from the surface of silicon wafer. The decontamination is based on the oxidation and complexing with an  $H_2O_2/NH_4OH/H_2O$  mixture. RCA 2 is used for removing the metal impurities from the surface of silicon by using an  $H_2O_2/HCl/H_2O$  mixture.

### 3.2 Plasma-enhanced chemical vapor deposition (PECVD)

Plasma enhanced chemical vapor deposition is commonly used method for deposition of solid layer on a substrate from a gas phase precursors. The chemical reactions take place after the plasma of the process gases strikes. The PECVD technique was introduced by Sterling and Swann [37] in 1965 for electronic devices. Hezel and Schrörner [18] transferred it from microelectronics to photovoltaics for fabrication of  $SiN_x : H$  anti-reflective coating in 1981.

In this work a direct PECVD system *Oxford PlasmaLab 100* is applied for deposition of amorphous  $SiN_x : H$  films. A conventional parallel-plate reactor, shown in Figure 3.1, is a RF (radio frequency) driven reactor, in which the substrate is placed on a grounded lower electrode. In direct plasma, all processing gases are excited with an electromagnetic field produced by RF generator at frequency of 13.56 MHz. Electrons are accelerated by the

applied electric field and collide with the molecules of the gas mixture. As a result of an inelastic collision with sufficient energy, the gas molecules become ionized. The RF frequency of 13.56 MHz is above the plasma frequency of ions ( $\omega_{P,ion}$ ) and below the plasma frequency of electrons ( $\omega_{P,e}$ ) which depends on particle masses.

$$\omega_{P,e} = \sqrt{\frac{e^2 n_e}{\epsilon m_e}} \quad (3.1)$$

with the electron density  $n_e$  and the relative permittivity  $\epsilon$ . Concluding, ions with larger mass compared to electrons ( $m_e$ ), cannot follow the alternating field and remain stationary at this frequency. This inhibits the strong ion bombardment towards the substrate and results in a higher quality surface passivation [8]. The process gas mixture enters from top of the chamber

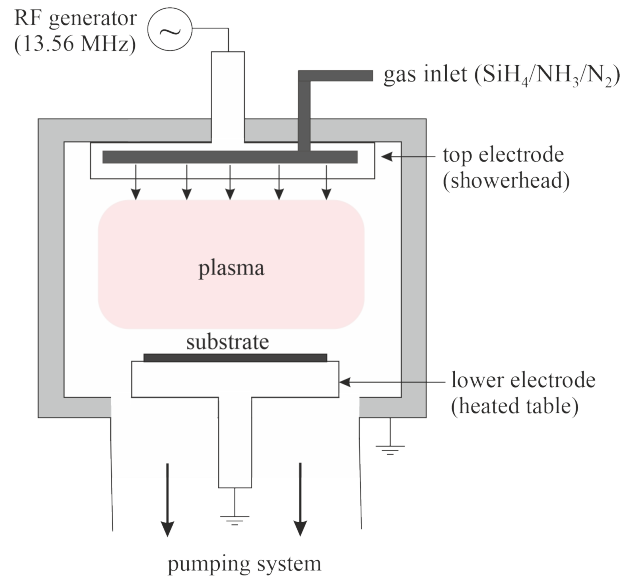


Figure 3.1: Schematic of Oxford Plasmalab 100 PECVD system.

through a shower head and is pumped down from the bottom by a rotary vacuum pump. The substrate carrier and the chamber walls are grounded, so that the potential (the so-called DC bias) is built between the top RF electrode and the substrate carrier which is shown by purple plasma region in Fig 3.1. This potential accelerates the charged dissociated gas species onto the surface of the substrate. A flow mass controller monitors and adjusts the flow rate of the processing gases. The lower electrode can be electrically heated up to 400 °C in this specific setup.

### 3.3 Reactive ion etching (RIE) process

The industrial standard to reduce the reflectivity of solar cells is the wet chemical texturing process [38]. The textures with common micrometer scales eliminate the reflectivity due to multiple reflections on the surface of the solar cell. A promising alternative method to the wet chemical etch process is the so-called black silicon method using the gas mixture of  $SF_6$  and  $O_2$ . Black silicon can be fabricated by using a microwave or inductively-coupled

plasma source in combination with a capacitively-coupled plasma source, referred to a reactive ion etching process (RIE). The texturing was firstly described by Jansen et. al. in 1995 as an undesirable side effect during cryogenic dry etching of silicon with  $SF_6/O_2/CHF_3$  plasma to produce microstructures with up to 200  $\mu m$  heights and high aspect ratios of  $\sim 10:1$  [39].

A schematic of the plasma etching chamber, *Oxford PlasmaLab 100 ICP 65*, that is applied for this work is shown in Figure 3.2. In this setup, the plasma can be ignited in two different

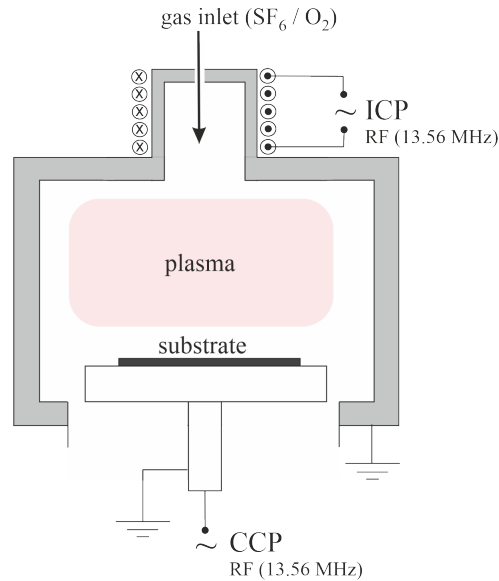


Figure 3.2: An illustration of plasma etch chamber (RIE) with inductively- (ICP) and capacitively-coupled plasma (CCP) sources.

modes, inductively-coupled plasma (ICP) and capacitively-coupled plasma (CCP). In an ICP process, the electromagnetic field is generated by a RF coil. The CCP process can lead to a strong negative charge of the electrode compared to the plasma. Therefore, the positively charged ions are accelerated perpendicular to the samples and may cause a surface damage. The potential between the electrode and the plasma is called the DC bias voltage, which increases with increasing the plasma power. The DC bias voltage can also be influenced by the gas pressure and the gas flow rate. In the ICP method, on the other hand, the plasma density can be adjusted independently of the ion energy, which is an advantage over the CCP method. Since a parallel coupled plasma ICP+CCP process is used in this work, surface damage and consequent increase of surface states are expected due to involved CCP process [40]. More details about the experiments and results are provided in Chapter 7.

### 3.4 Rapid thermal anneal (RTA) process

In the final step of silicon solar cell production, the  $SiN_x : H$ -coated silicon wafers undergo an in-line metallization process in a belt furnace. In this process, a silver paste is brought into contact with the silicon in a rapid thermal annealing (RTA) process to form the front contact, also known as the contact-firing (co-firing) process. The wafers are treated at peak temperature

of 700-900 °C for few seconds. In this work, the metal contacts were not employed, but the samples went through the industrial rapid thermal annealing process in order to study the impact of high temperatures on the properties of  $SiN_x : H$  and the mechanisms of hydrogen passivation. The samples are fired after the deposition of  $SiN_x : H$  layers in a standard fast firing furnace at Hanwha Q CELLS. Figure 3.3 displays the thermal profile of a contact-firing process.

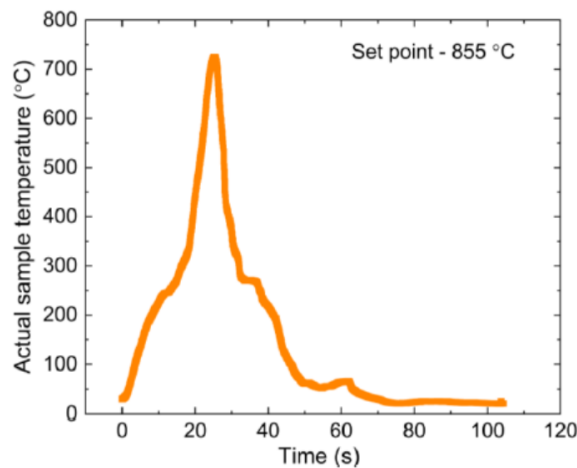


Figure 3.3: An example of a rapid thermal annealing process with a set peak temperature of 885 °C measured on a passivated mc-Si wafer. It can be clearly seen that the measured sample temperature is significantly lower than the peak temperature [41].

### 3.5 DC Magnetron sputtering deposition

DC Magnetron sputtering deposition is a physical vapor deposition (PVD) technique used to grow thin films of metals or semiconductors. In this method, fast inert gas ions (mostly argon Ar) are generated in a magnetron plasma with kinetic energies in the range of about 100 – 1000eV [42]. In DC sputtering, a negative voltage is applied to the cathode, which is also the target. The anode is usually integrated in the magnetron near the target. In addition, the vacuum chamber and the substrate holder also function as an anode. The generation of charge carriers occurs through the collisions of the electrons with the atoms in the plasma. The superposition of the electric-field with the magnetic-field leads to an increase of the electron concentration in the area of the target surface and thus to a higher ionization rates. The positively charged high-energy ions are then accelerated toward the cathode and collide with the surface of the target. The atoms ejects from the target with sufficient kinetic energy can reach the surface of the substrate and form a thin layer of the target material. In this work, a DC magnetron sputtering at *Anhalt university of applied sciences (HSA)* is used for deposition of metal layers for MIS (Metal-insulator-semiconductor) devices for C-V characteristics.

## Chapter 4

# Characterization Methods

### 4.1 Fourier-transform infrared (FTIR) spectroscopy

Fourier-transform infrared spectroscopy is a widely used method to extract the density of the chemical bonds and the components in a sample under consideration. When the sample is exposed to infrared radiation, a selective frequencies (wavenumbers) are absorbed by the molecules of the samples that alters the dipole moment of the molecules. As a consequence, the vibrational energy level of the molecules changes from equilibrium state to excited level. The IR peak frequency indicates the essential energy for this transition and the number of peaks are related to the vibration modes of the molecules. For this work, *Bruker Vertex 70* is used for FTIR spectroscopy in the mid-infrared (MIR) region of  $400\text{-}4000\text{ cm}^{-1}$  with resolution of  $4\text{ cm}^{-1}$  to estimate the bond configuration in the  $\text{SiN}_x : \text{H}$  layers. For the measurements, symmetrically polished wafers were used to minimize the discrepancies between the two sides of the sample. Figure 4.1 shows an example of  $\text{SiN}_x : \text{H}$  related IR absorption spectrum. A bare silicon wafer was measured as a background and subtracted

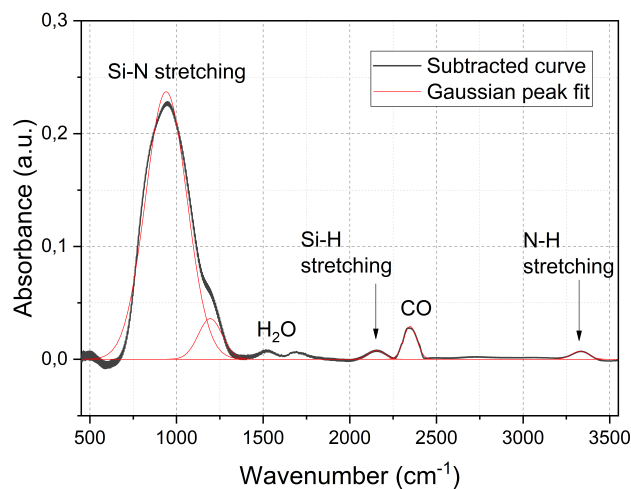


Figure 4.1: IR absorption spectra of  $\text{SiN}_x : \text{H}$  film as function of wave number indicating three main peaks of  $\text{Si-N}$ ,  $\text{Si-H}$  and  $\text{N-H}$  in stretching mode.

from the IR absorption spectra of the coated sample. For evaluation of the bond densities, the peaks were determined by Gaussian fit analysis after a polynomial baseline correction. The peak position of  $Si - N$  stretching mode is reported at wave numbers of 790- 1020  $cm^{-1}$  [29],  $Si - H$  stretching mode at 2000-2300  $cm^{-1}$  and  $N - H$  stretching mode at 2500-3340  $cm^{-1}$  [29] [43]. From the model developed by Lanford [44] and Yin et al. [45], the density of a chemical bond  $[A - B]$  can be determined by

$$[A - B] = K_{[A-B]} \int \alpha(\omega) d\omega \quad (4.1)$$

With the IR absorption cross section of  $A - B$  bond  $K_{[A-B]}$  and the absorption  $\alpha(\omega)$ . The integral  $\int \alpha(\omega) d\omega$  can be calculated from the area under the absorption spectrum as a function of the wavenumber ( $\omega$ ). The area under the IR peak is with a good approximation the product of the absorbance and the bandwidth at half-absorbance [44]. Lanford et al. reported that the specific absorption of Si-H bonds in SiN is about 1.4 times of the N-H bonds. The  $K$  values are taken from the literature [45] as  $2.4 \times 10^{16} cm^{-1}$  for the  $Si - N$  stretching,  $5.9 \times 10^{16} cm^{-1}$  for the  $Si - H$  stretching and  $8.2 \times 10^{16} cm^{-1}$  for the  $N - H$  stretching. Due to linear proportionality, the integrated area ( $\int \alpha(\omega) d\omega$ ) is mostly used as a measure of the bond density in this work.

## 4.2 Spectroscopic ellipsometry (SE)

Spectroscopic ellipsometry (SE) is a non-destructive characterization technique that has been used extensively to determine the optical properties of thin films. The ellipsometric parameters,  $\psi$  and  $\Delta$ , are measured by a *JA-Woollam EC-400* system in the wavelength range of 210-1000 *nm*.

The incident linearly polarized electromagnetic (EM) wave is partially reflected or transmitted when it reaches the sample. The change in the state of polarization is measured of the reflected part,  $R$ , which is generally elliptically polarized. Thus, during the measurement, according to equation 4.2, the change of the amplitude ratio,  $\psi$ , and the phase difference,  $\Delta$ , of the reflected EM-wave can be determined. The indices " $s$ " and " $p$ " denote the component perpendicular and parallel to the plane of incidence.

$$\tan(\psi)e^{i\Delta} = \frac{R_p}{R_s} \quad (4.2)$$

The variation of the film thickness changes the length that light travels through the film, while the index introduces the angle of the incident light and the reflectivity. A model based on the dispersion relationship is used to evaluate the optical properties of a material by matching certain fitting parameters to experimental data. The Tauc-Lorenz model is used in this work to determine the optical properties of amorphous  $SiN_x : H$  films [46]. The model consists of a known substrate and a top layer of dielectric with unknown optical properties. To fit the experimental data with minimal mismatch, an iterative fitting process is performed in the software program W-VASE (JA-woollam).



### 4.3 Photoconductance carrier lifetime tester

Figure 4.2 shows the scheme of a photoconductance charge carrier lifetime tester *WCT-120 Sinton Instrument*. In this setup, sample is mounted under a flash lamp and on the top of a coupled RF coil. When the sample is flashed by the lamp, the change in the sheet conductivity is measured with the RF coil. The light intensity is measured simultaneously by a calibrated light sensor located near the sample.

For measuring the charge carrier lifetime, two methods are common, (1) the quasi-steady state

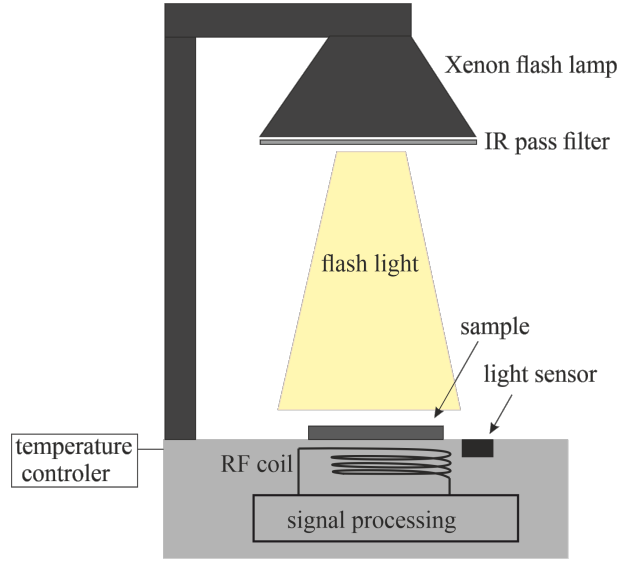


Figure 4.2: A schematic of a photoconductance charge carrier lifetime tester *WCT-120*.

(QSS) measurement method and (2) the quasi-transient method. Depending on the charge carrier lifetime of the sample  $\tau_{eff}$ , if it is smaller, larger or equal to the decay time of the flash lamp, one of the methods is used. These two methods are the limited cases of the general equation [47] that calculates the effective charge carrier lifetime  $\tau_{eff}$  of the sample,

$$\tau_{eff} = \frac{\Delta n(t)}{G(t) - \frac{\partial \Delta n}{\partial t}} \quad (4.3)$$

with the photo-generation rate  $G(t)$  and excess carrier density  $\Delta n$  that is calculated from the change of the sheet conductivity  $\Delta\sigma$  of sample,

$$\Delta\sigma = qW(\mu_n + \mu_p)\Delta n \quad (4.4)$$

with the mobility of the electron  $\mu_n$  and the holes  $\mu_p$  and the sample thickness  $W$ .

In the quasi-steady-state method, sample is subjected to very slow decay of the light, so it is assumed that  $\frac{\partial \Delta n}{\partial t} = 0$ . This method is used for the samples samples with short charge carrier lifetime assuming steady-state conditions.

$$\tau_{eff} = \frac{\Delta n(t)}{G(t)}. \quad (4.5)$$

The photo-generation rate can be measured from the amount of light absorbed in sample with known optical constant.

While, in the case of transient measurement method, a very short pulse of light (typically in range of 10-20  $\mu s$ ) is applied, only to excite the charge carriers in the samples and then it is off. Therefore, in the transient mode, it is assumed that the  $G(t) = 0$ . The transient method is applied for samples with large charge carrier lifetimes

$$\tau_{eff} = -\frac{\Delta n(t)}{\frac{\partial \Delta n}{\partial t}}. \quad (4.6)$$

The quality of the passivation and the bulk lifetime of minority charge carriers can be acquired from the shape of injection-dependent lifetime curve. For the comparison of the passivation quality in different samples, a single value of  $\tau_{eff}$  is taken at the excess charge carrier density,  $\Delta n$ , of  $10^{15} \text{ cm}^{-3}$  which is approximately equal to the excess carrier density in silicon solar cells under normal operating conditions (forward bias 0.5 V and AM1.5 illumination).

#### 4.4 Capacitance-Voltage (C-V) measurements

C-V measurements are powerful characterization tools for studying thin films properties at the surfaces and the interfaces, particularly in metal-insulator-semiconductor (MIS) devices. In MIS structure, the rear side of the semiconductor and the metal gates at the front side are Ohmically contacted, which introduce the two electrodes of a capacitor. The insulator layers such as  $SiN_x$  form the dielectric between the two electrodes of the capacitor. In this work, the C-V measurements are used to particularly determine the positive fixed charges in the  $SiN_x : H$  layers and the surface states at the interface of  $Si/SiN_x : H$ . Measurements are performed at a high frequency of 1 MHz at room temperature in the dark. As the DC-bias is swept, the MIS device switches from the accumulation region to the depletion region and further into the inversion region [48]. More details about the MIS structure and the data acquisition are presented in Chapter 6 (6.1.2.III).

For this work, multi-frequency Keithley 4200-CVU impedance measurement card (with frequency ranges between 10 KHz and 10 MHz) is used with AC test signal (10 mV RMS to 100 mV RMS) that can generate DC voltages biased from -30 V to +30 V. A scheme of the measurement circuit is shown in Figure 4.3. During the test, the complex AC impedance ( $Z$ ) of device under test (DUT) is measured by applying the AC voltage, via the resulting AC current, AC voltage ( $V_{AC}$ ) and the phase angle ( $\theta$ ) between them. In this case, the capacitance of the device under test frequency  $f$  can be calculated by

$$C_{DUT} = \frac{I_{DUT}}{2\pi f V_{AC}}. \quad (4.7)$$

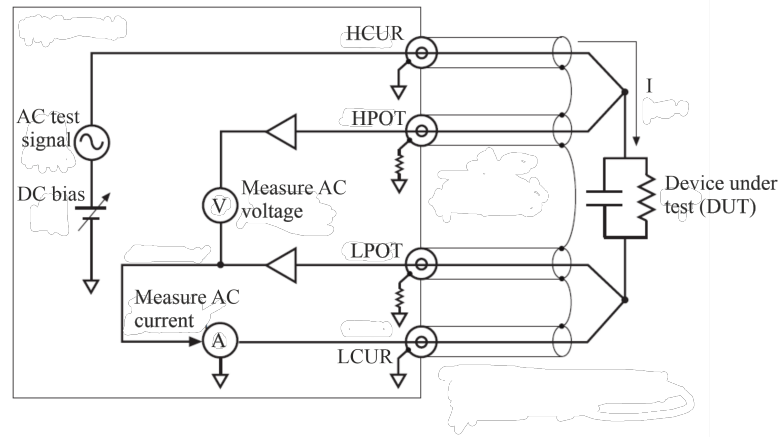


Figure 4.3: Circuit diagram of the C-V measurement system, Keithley 4200-CVU [49].

The system can measure the device under test (DUT) in parallel or series RC (resistor-capacitor) configuration. In a series configuration, the series capacitance  $C_s$  and resistance  $R$  are

$$R = Z \sin \theta \quad \text{and} \quad \frac{1}{\omega C_s} = Z \cos \theta \quad (4.8)$$

with the angular frequency,  $\omega = 2\pi f$ , of the AC signal. While, in a parallel configuration, the parallel capacitance  $C_p$  and conductance  $G_p$  can be determined from

$$C_p = \frac{C_s}{1 + B^2} \quad \text{and} \quad G_p = R_s \left( R_s^2 + \frac{1}{(\omega C_s)^2} \right) \quad (4.9)$$

with the dissipater factor  $B$  that indicates the ratio of real and imaginary parts of the  $Z$ .

## 4.5 Scanning electron microscopy (SEM)

Scanning electron microscopy provide images by scanning the surface of samples with a focused beam of electron. The electron beam passes through scanning coils which are energized by variable voltages and creating a magnetic field that deflects the beam in a controlled pattern. The electron beam is then focused onto the sample as a very fine spot through a magnetic objective lens. There are different products from the interaction of the electrons with the atoms in various depth within the sample as shown in Figure 4.4.

The secondary electrons (SE) are the results of inelastic collisions of primary electrons with the samples atoms in near-surface regions, therefore they are useful to study the topography of the sample surface. The emitted secondary electrons are detected in most devices with an Everhart-Thornley detector [50]. The secondary electrons have a low energy which limits their mean free path length in a solid sample and therefore only those at nanometer scales near the surface can be removed from the sample and be detected. The signal of the secondary electrons is strongly centered on the point where primary electrons hit the sample and consequently enables the acquisition of images with a resolution better than 1 nm. For this work, the SEM HITACHI Su70 is used to provide images from the passivated textured surfaces

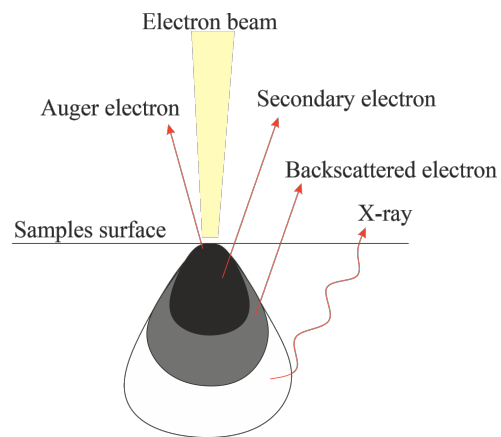


Figure 4.4: Interaction of electrons with atoms and the signals that are generated in various depth of the sample.

in order to study the impact of surface roughness on the passivation mechanisms of the  $SiN_x : H$  layers.

## Chapter 5

# Effusion Mass Spectroscopy for PV Applications

### 5.1 Introduction

Hydrogenated amorphous layers deposited at low temperatures can provide high surface passivation to achieve highly efficient silicon solar cells. Amorphous silicon nitride layers, typically grown by plasma-enhanced chemical vapor deposition (PECVD), have therefore been investigated over the last forty years [10] [25] [51]. It is well known that these layers release hydrogen during the contact firing step (RTA process), which is essential for the metallization at about 700-800 °C. At such high temperature, most of the hydrogen molecules effuse into air, but a part of it diffuses into the silicon bulk and passivate the crystallographic defects and accelerate the recovery in case of carrier-induced defects like boron-oxygen (BO) complexes [52] [53].

#### 5.1.1 Aim of this work

Few technologies can detect hydrogen directly, since hydrogen has only one electron and interacts weakly with common analytical probes. Furthermore, the high temperature firing process can also affect the properties of  $SiN_x : H$  films, so it is important to provide a coating with high thermal stability. The objective of this work is to improve the physical understanding of the hydrogen transport mechanisms in relation to the film properties of PECVD-deposited  $SiN_x : H$ . Therefore, an effusion mass spectrometer is developed, which is not only capable of detecting hydrogen, but also gives valuable information about the film composition of the hydrogenated films and its correlation with the hydrogen effusion/diffusion regimes.

#### 5.1.2 State of the literature

The experiments of hydrogen effusion from silicon was first carried out in 1975 by Triska et al. [54], however gas effusion measurement is generally an older method. In 1962, Redhead et al. [55] published a review study of gas desorption kinetics by applying a variation of the sample temperature. He calculated the activation energy of desorption as a function of the

maximum desorption temperature  $T_p$  for various numbers of reactions. Some decades later, Beyer et al. established and developed the hydrogen effusion mass spectroscopy for studying the role of hydrogen in hydrogenated silicon material through investigation of the saturation of dangling bonds at the surface and interface with the main focus on amorphous  $Si_x : H$  films [56] [57]. The study of glow-discharge  $SiN_x : H$  alloys via effusion measurements performed in 1987 showed that the addition of nitrogen atoms to amorphous hydrogenated silicon material shifts the hydrogen effusion peak to a higher temperature, which was correlated with the higher binding energy of N-H bonds [58]. Later in 1996, Murley et al. [59] applied both FTIR spectroscopy and hydrogen effusion measurements to analyze the role of deposition parameters on the film composition of silicon nitride. In 2006, Beyer and Dekkers reported about the application of effusion measurements for studying the microstructure of  $SiN_x : H$  films and showed that the effusion of hydrogen from a porous network is mainly in the form of hydrogen molecules while in compact material, atomic hydrogen is the dominant diffusing species [60]. In this work, the developing process of a simplified effusion measurement setup is presented in order to focus more on hydrogen-related mechanisms in PV applications. Therefore, it is investigated whether effusion mass spectroscopy can be a suitable benchmark for evaluating the rapid thermal annealing process. Furthermore, the sensitivity of the hydrogen detection by effusion mass spectroscopy is compared with nuclear reaction analysis (NRA) as an established and accurate method.

## 5.2 Development of effusion mass spectroscopy

### 5.2.1 System setup

Figure 5.1 shows a photograph of our newly developed effusion measurement system with all relevant spectrometer components and their position within the system. As shown, the instrument is equipped with a quadru-pole mass spectrometer, a turbo-molecular pump, a penning manometer, a quartz tube as vacuum vessel and a heating furnace.

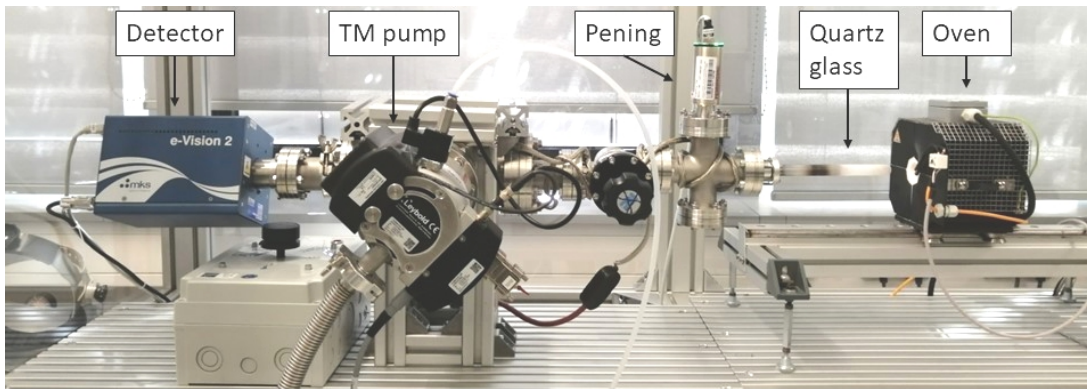


Figure 5.1: A photograph of gas effusion mass spectrometer setup at Fraunhofer CSP, the main compartments are labeled.

The pumping system includes a Backing pump (rotary pump) in order to build up an initial required vacuum of about  $10^{-2} - 10^{-3}$  mbar behind a Turbo-molecular pump for an ultra-high vacuum. The turbo-molecular pump operates on the basis of shuffling the gas molecules from the Ultra-high vacuum (UHV) container to the backing pump by a high-speed rotor ( $10k - 30k$  rpm) [61] which can result in a vacuum pressure of about  $10^{-9}$  mbar.

The pressure within the apparatus is measured by a penning vacuum gauge. The principle of a penning vacuum gauge is the cold cathode ionization. The gauge contains two unheated electrodes operating at an applied DC voltage. To achieve a sufficient number of electron collision with the gas molecules a longer path is provided by applying a magnetic field. The pressure shown on the meter depends on the discharge current which is formed by the positive or negative charge carriers.

A MKS quadru-pole mass analyzer (QMS) is mounted in this system with the operating pressure of  $6.5 \times 10^{-4}$  mbar including a Faraday detector which is able to detect molecular masses of  $1 - 100$  amu. The gas molecules or atoms effused from the samples are converted into ions by an ionizer in the mass analyzer. The quadru-pole filter separates then the various ions by their mass to charge ratio ( $m/e$ ) and present the user selected  $m/e$  to the collector. Then the detector converts the filtered ion beams into small electrical current, which is amplified and displayed for the user.

The tube furnace can be heated up to  $1200$  °C with heating rates ( $\beta$ ) up to  $40$  °C/min. The temperature of the oven is measured by a thermocouple thermometer.

A quartz glass with outer diameter of  $16$  mm and a length of  $25$  cm is applied as a vacuum

chamber. The samples are mounted in the quartz tube with the help of small nickel boats for latter transport into position which will be heated in the furnace.

### 5.2.2 Functional principles

A schematic illustration of the effusion mass spectroscopy is presented in Figure 5.2. Regarding the size of the quartz glass, small samples with a size of  $5\text{ mm} \times 5\text{ mm}$  or

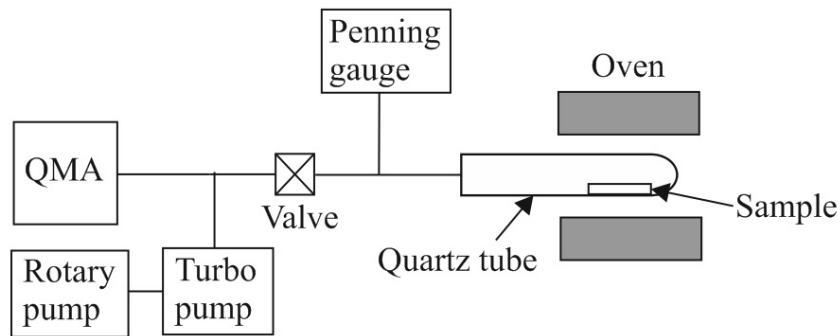


Figure 5.2: Schematic illustration of the effusion mass spectroscopy.

$10\text{ mm} \times 2\text{ mm}$  can be mounted and measured in this system. A quartz tube with a length of  $25\text{ cm}$  and an outer diameter of  $16\text{ mm}$  is used as a vacuum chamber in this system, which is sealed from one side and constantly pumped out from the other side. Samples are mounted on small nickel boats to be spatially adjusted under vacuum from the outside of the quartz tube via a small magnet. The oven is mounted on a railway and can move towards the quartz tube.

To measure a sample, it is placed in the end part of the tube (right side) where it is heated by the oven. The rest of the samples are kept in the cold part of the tube (left side) away from the heated range. Prior to the measurements, this end part of the tube is baked at  $1000\text{ }^\circ\text{C}$  for  $10\text{ min}$  to remove residual hydrogen. Moreover, in order to eliminate background gas interferences and moisture present in the equipment, the system is baked out with a heating filament at  $130\text{ }^\circ\text{C}$  for several hours after pumping down the chamber. Before each sample measurement, a reference measurement is carried out to determine the background  $H_2$  concentration in the measurement setup and this value is subtracted from the sample measurements. The samples are heated from room temperature to  $1000\text{ }^\circ\text{C}$  at a constant heating rate ( $\beta$ ) of  $20\text{ }^\circ\text{C}/\text{min}$  and the partial  $H_2$  pressure in the reactor is measured as a function of the annealing temperature  $T_a$ .

By heating the sample at a constant heating rate, free gas molecules diffuse out of the sample into the vacuum chamber and are transferred to the detector at a constant pumping speed. The total gas pressure including all different molecules diffusing out of the sample and the actual pressure of selected molecular masses are measured and displayed.

### 5.2.3 Data analysis

Figure 5.3 shows a screenshot of the Lab-view program in which the user accesses any measurement modes, the filament control and diagnostics. The actual temperature of the



furnace is measured by a thermal sensor and is displays in the software. As soon as the ionizer

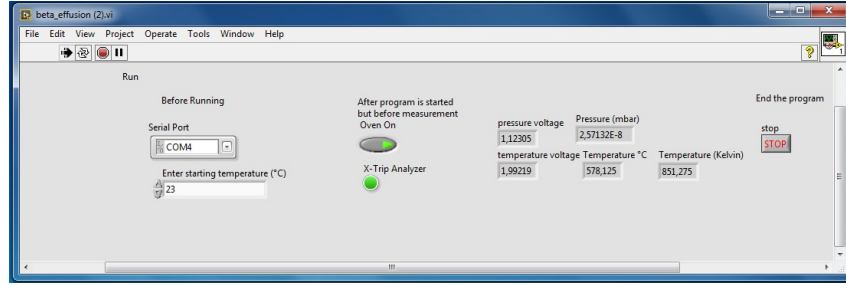


Figure 5.3: A screen shot of software program.

filament is switched on and the detector lamp (X-trip analyzer) turns green in Lab-view, the partial pressure of the selected gases are displayed in Easy-view program shown in Figure 5.4 as a function of time (left-side diagram) and molecular mass (right-side diagram).

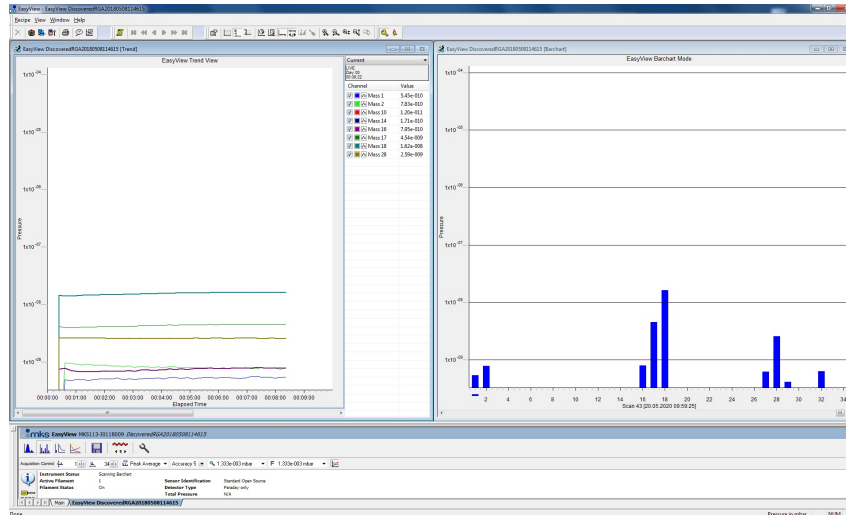


Figure 5.4: A screen shot of software program Easy view.

### Estimation of hydrogen content from effusion spectrum

The number of molecules  $\Delta N$  flowing through a specific cross section within a period of time  $\Delta t$  is called flow rate  $q$  [62],

$$q = \frac{\Delta N}{\Delta t}. \quad (5.1)$$

The hydrogen pressure at the pump port  $P_{H_2}$  is a measure of the effusion rate, as the turbomolecular pumps operate with constant pumping speed over a wide pressure range [57]. Thus, the flow rate is given,

$$\frac{dN_{H_2}}{dt} = C_0 P_{H_2}. \quad (5.2)$$

This applies under the assumption that hydrogen adsorption and desorption at the walls of the container is negligible and the hydrogen flow is not hindered by the vacuum lines. The factor

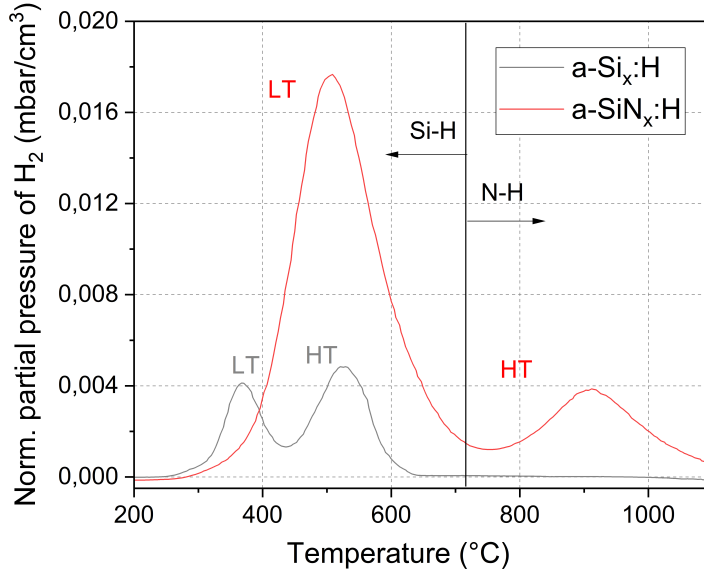


Figure 5.5: An example of hydrogen effusion spectrum of PECVD deposited  $SiN_x : H$  and  $a - Si_x : H$  films. The normalized partial pressure of molecular hydrogen is measured as a function of heating temperature. The peaks' position in the effusion spectrum are composition-dependent and shift to higher temperatures with incorporation of more nitrogen in film.

$C_0$  depends on the suction capacity of vacuum pump which is in this system equal to 78 *lit./s*. The suction capacity indicates the volume of the gas flowing into the nozzles of the vacuum pump.

At a constant heating rate ( $\beta$ ), the temperature is a linear proportion of time  $T = \beta t + T_0$ . Regarding that and equation 5.2, the atomic density of hydrogen is proportional to the time or temperature integral of the normalized partial pressure of effused hydrogen at a constant heating rate.

$$N_{H_2} = \int \left( \frac{dN_{H_2}}{dt} \right) dt = C_0 \int_{t_0}^t P_{H_2} dt = \frac{C_0}{\beta} \int_{T_0}^T P_{H_2} dT. \quad (5.3)$$

The integrated area  $A_{eff}$  under the effusion spectrum as function of temperature is proportional to the hydrogen concentration  $N_{H_2}$  in the film.

$$A_{eff} = \int_{T_0}^T P_{H_2} dT \quad (5.4)$$

An example of hydrogen effusion from the  $SiN_x : H$  layer is shown in Figure 5.5. The partial pressure of hydrogen molecules is plotted as a function of the annealing temperature. The values are normalized to the volumes of the film.

### Interpretation of hydrogen effusion spectra

In Figure 5.5, the partial pressure of effused hydrogen from a  $a - Si_x : H$  layer is also plotted with gray color next to the amorphous  $SiN_x : H$  layer. Both layers are deposited by PECVD at substrate temperature of 150 °C on polished Si wafers. Beyer et al. attributed the two peaks in the  $a - Si_x : H$  layer related to (1) molecular hydrogen desorbing from the surface or diffusing from the bulk at low temperatures (*LT* peak) and (2) diffusion of atomic hydrogen from breaking the Si-H bonds in the film or at the interface at higher temperatures (*HT* peak) [63]. This is valid when the Si-H bonds are assumed to be the only hydrogen bonds in the films. Regarding the graph of  $SiN_x : H$ , its first peak appears between the two hydrogen peaks observed for  $a - Si_x : H$  film. Moreover, there is a peak at higher temperature that is not found for  $a - Si_x : H$ . The addition of nitrogen atoms and the corresponding higher binding energy of the N-H bond ( $\sim 3.59$  eV) compared to that of the Si-H bond ( $\sim 3.06$  eV) shift the effusion peaks to higher temperatures [64] and lead to presence of an extra peak at relative higher temperatures.

In contrast to the hydrogen desorption from the surface, the effusion of hydrogen by breaking the Si-H or N-H bonds is composition dependent and related to the diffusion coefficient  $D_0$  of the film. [57]. Therefore, an early release of hydrogen can be indicative of a film with void structure [58]. For the  $SiN_x : H$  film, the heights of the *LT* and *HT* peaks reveal the film stoichiometry, high incorporation of Si in the film leads to higher *LT* peak, while more N corresponds to a higher *HT* peak.

### 5.3 Comparison of the effusion measurement with the rapid thermal firing process

As already mentioned at the beginning of this chapter, silicon solar cells undergo a firing process to form the front-contacts after the  $SiN_x : H$  passivation layers are deposited. To study the impact of the firing process on the passivation properties of the  $SiN_x : H$  films, samples are annealed in a constant heating rate  $20\text{ }^\circ\text{C}/\text{min}$  and the effusion of hydrogen is measured using a effusion mass spectroscopy. The time scale of the firing process is however much faster than the effusion experiment. Therefore, the following experiments are performed to simulate the rapid thermal firing process. The results are compared with the results of the effusion experiments at constant heating rate.

Five different  $SiN_x : H$  layers are deposited on the both sides of the Si wafers. After the deposition, two pieces of each sample are used. One piece is located in the vacuum chamber under the preheated oven at  $700\text{ }^\circ\text{C}$  for few minutes while the effusion of hydrogen is measured as a function of time. The temperature of  $700\text{ }^\circ\text{C}$  is chosen because the standard firing process takes place at  $\sim 700\text{-}800\text{ }^\circ\text{C}$ . The other piece of the sample is annealed at a constant heating rate of  $20\text{ }^\circ\text{C}/\text{min}$  and the effusion of hydrogen is measured vs. the annealing temperature.

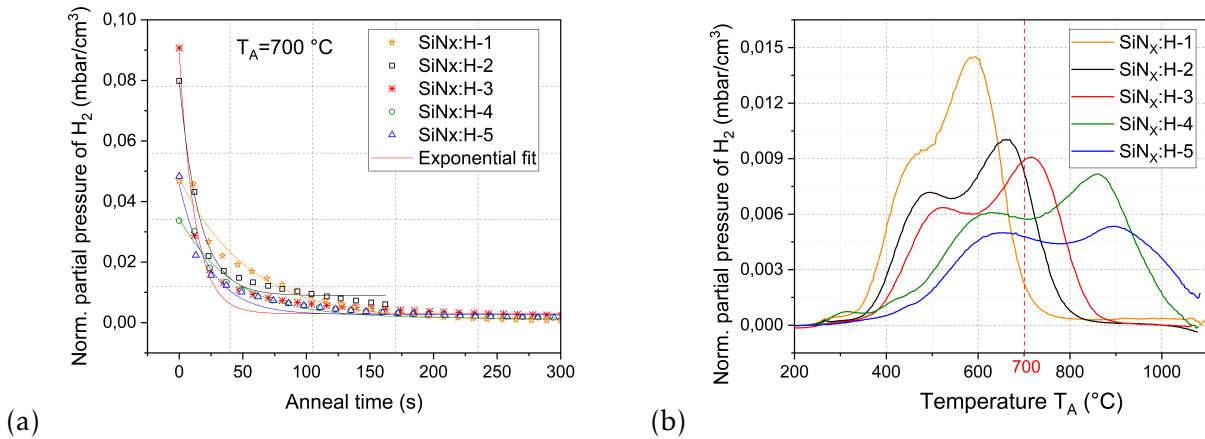


Figure 5.6: a) The partial pressure of effused hydrogen from five different  $SiN_x : H$  layers decreases exponentially when the samples are exposed to a constant temperature of  $700\text{ }^\circ\text{C}$  for a few minutes. b) hydrogen effusion spectra of identical samples at constant heating rate  $\beta$  of  $20\text{ }^\circ\text{C}/\text{min}$ .

The results are shown in Figure 5.6a presetting the normalized partial pressure of hydrogen as a function of time. A maximum is observed in the first few seconds for all samples, followed by an exponential drop as fitted using,

$$P_{H_2} = P_0 e^{-R_0 t} \quad (5.5)$$

where  $P_0$  is the initial value of hydrogen partial pressure and  $R_0$  the decay constant. On the

other hand, the hydrogen effusion spectra of second pieces of the samples are obtained by heating them up to 1100 °C with constant heating rate of  $\beta = 20$  °C/min as shown in Figure 5.6b. By comparing these two diagrams, the decay constant  $R_0$  increases from  $SiN_x : H-1$  to  $SiN_x : H-5$  with the reduce of effused hydrogen below 700 °C in Figure 5.6b.

Moreover, it is observed that the time integral of normalized partial pressure of effused hydrogen  $P_{H_2}$  at constant temperature  $T = T_{firing}$  is proportional to the temperature integral of  $P_{H_2}$  at constant heating rate. It is shown by the gray areas under the exponential fit and the inserted effusion spectrum in Figure 5.7. From the equation 5.3, it can be concluded that,

$$\int \frac{dN_{H_2}}{dt} dt \propto C_0 \left[ \int_0^t P_{H_2} dt \right]_T \propto \frac{C_0}{\beta} \left[ \int_{T_0}^T P_{H_2} dT \right]_{\beta}. \quad (5.6)$$

It means that the calculated area under the effusion spectra  $A_{eff}$  in Figure 5.6a are

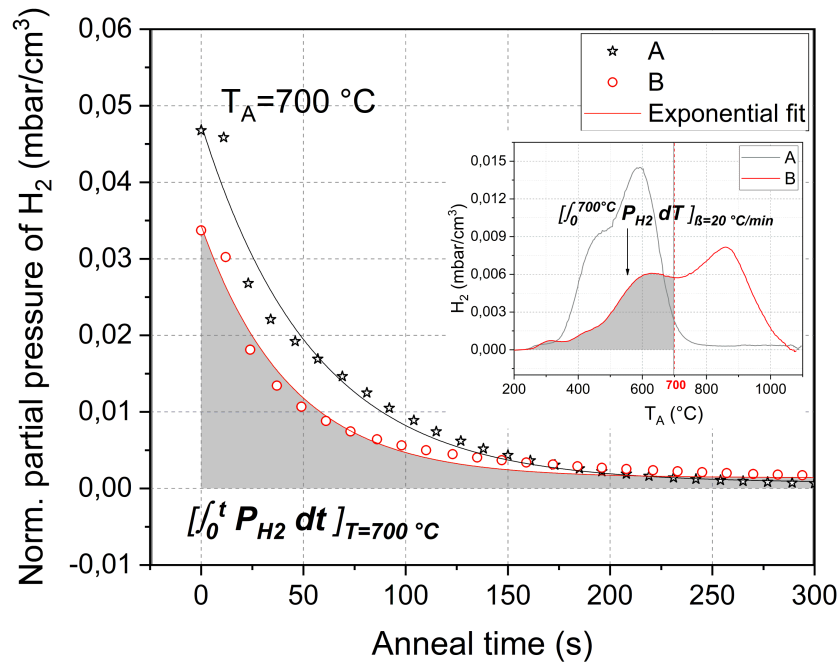


Figure 5.7: The partial pressure of effused hydrogen decreased exponentially when the samples are exposed to a constant temperature of 700 °C for a few minutes. The time integral of normalized partial pressure of effused hydrogen  $P_{H_2}$  at constant temperature is proportional to the temperature integral of normalized  $P_{H_2}$  at constant heating rate, shown by gray areas under exponential fits and the insert effusion spectra.

proportional to the area under the exponential fit in figure 5.6b. The values are listed in Table 5.1. This implies that the effusion of hydrogen from  $SiN_x : H$  is strongly temperature-dependent and the main part of diffusion/effusion occurs at a given temperature within the first few seconds. Therefore, the effusion measurement with a constant heating rate can also provide a comparable measure of the effused hydrogen during a rapid annealing process.

| Sample        | $[\int_0^t P_{H_2} dt]_{T_{firing}}$ | $[\int_{T_0}^{T_{firing}} P_{H_2} dT]_{\beta}$ |
|---------------|--------------------------------------|--|
| $SiN_x : H-1$ | 2.86                                 | 2.75   |
| $SiN_x : H-2$ | 2.64                                 | 2.65   |
| $SiN_x : H-3$ | 2.55                                 | 2.32   |
| $SiN_x : H-4$ | 2.11                                 | 1.86   |
| $SiN_x : H-5$ | 1.97                                 | 1.82   |

Table 5.1: The time integral of normalized partial pressure of effused hydrogen  $P_{H_2}$  at constant temperature and the temperature integral of normalized  $P_{H_2}$  at constant heating rate decrease proportionally. The values are shown in arbitrary units.

## 5.4 Comparison of effusion mass spectroscopy with other established methods

In this section, hydrogen density measured by effusion mass spectroscopy is quantitatively compared with nuclear reaction analysis (NRA) as a common method for detecting hydrogen. A summary of the advantages and limits of effusion mass spectroscopy will also be discussed later.

### 5.4.1 Quantitative comparison with nuclear reaction analysis (NRA)

The amount of hydrogen released from PECVD deposited hydrogenated amorphous silicon ( $a-Si_x : H$ ) layers is determined by effusion measurements and compared with the hydrogen concentration which is previously measured by nuclear reaction analysis (NRA). The experimental flow chart is shown in Figure 5.8.

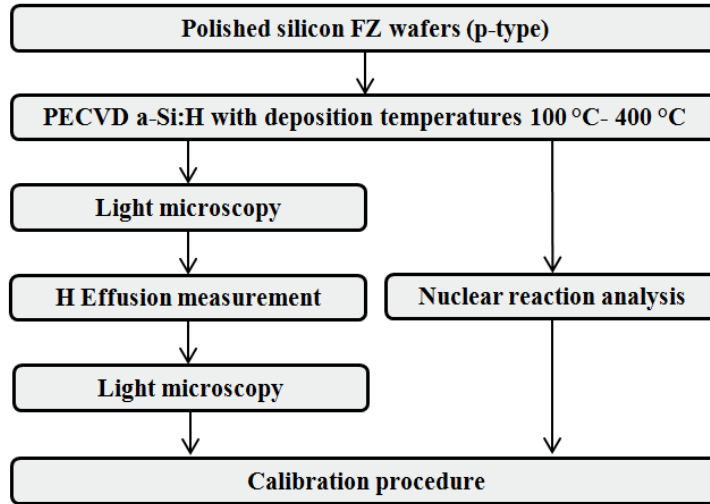


Figure 5.8: Flow chart of the experimental and the characterization procedure.

### Hydrogen content in $a-Si_x : H$ measured by NRA

Nuclear reaction analysis (NRA) is a commonly used method to detect hydrogen with a high sensitivity of  $\sim 100$  ppm ( $\sim 10^{18} \text{cm}^{-3}$ ) at near surface depth [65]. The resonant nuclear reaction of  $H + {}^{15}\text{N} \rightarrow {}^{12}\text{C} + {}^4\text{He} + \gamma$  (4.43 MeV) is used to profile hydrogen in the film [44]. From that, the number of  $\gamma$  rays detected is proportional to the hydrogen concentration in

the film. The measured hydrogen concentration  $C_H$  in the  $a - Si_x : H$  layers as well as the layer thicknesses  $d$  are given in Table 5.2. As the substrate temperature  $T_S$  rises, the hydrogen concentration measured by NRA drops from 20 at-% to 10 at-% while the thickness of the film increases. More details about the NRA measured hydrogen concentration of this set of samples is published by Steffens et al. [66].

| Sample name | $T_S$<br>[°C] | $d$<br>[nm] | $C_H$<br>[at.%]  |
|-------------|---------------|-------------|------------------|
| A1          | 100           | 438         | $19.22 \pm 0.08$ |
| A2          | 150           | 526         | $17.67 \pm 0.08$ |
| A3          | 200           | 608         | $15.61 \pm 0.07$ |
| A4          | 250           | 683         | $13.77 \pm 0.07$ |
| A5          | 300           | 724         | $12.27 \pm 0.07$ |
| A6          | 400           | 778         | $10.09 \pm 0.06$ |

Table 5.2: The film thicknesses  $d$  and NRA measured hydrogen concentration  $C_H$  of PECVD deposited  $a - Si : H$  films on  $c - Si$  wafers at various substrate temperatures  $T_S$  [66].

#### Hydrogen content in $a - Si_x : H$ measured by Effusion mass spectroscopy

The normalized partial pressure of effused hydrogen as a function of the annealing temperature  $T_A$  is presented in Figure 5.9. The shape of the hydrogen effusion graphs of samples A1 and A2 are similar. There are two effusion peaks, one at lower temperature ( $LT$ ) of about 360 °C and one at higher temperature ( $HT$ ) of about 530 °C. In contrast, a significant difference in the effusion curve is found for rest of the samples. In samples A3 to A6, the  $HT$  peaks become the main component of the effusion spectra and a sharp peak ( $SP$ ) appears at the rising edge of the  $HT$  peak.

A list of the peak positions with the mean values and the standard deviation for the integrated area under peaks ( $A_{eff}$ ) is presented in Table 5.3. The integrated areas are calculated using the equation 5.4, The correction factor  $C_0$  is not applied in these calculations and the values of  $A_{eff}$  are given in arbitrary units. The possible reasons for the occurrence of the sharp peaks will be discussed later in this chapter.

| Sample name | Mean $A_{eff}$<br>[a.u.] | SD<br>[Err±] | $LT$<br>[°C] | $SP$<br>[°C] | $HT$<br>[°C] |
|-------------|--------------------------|--------------|--------------|--------------|--------------|
| A1          | 2.21695                  | 0.197        | 357          | –            | 539          |
| A2          | 2.29774                  | 0.485        | 367          | –            | 528          |
| A3          | 2.09823                  | 0.299        | 357          | 497          | –            |
| A4          | 1.81366                  | 0.119        | 373          | 457          | 497          |
| A5          | 1.43484                  | 0.303        | 373          | 443          | 505          |
| A6          | 1.05926                  | 0.199        | 371          | 407          | 499          |

Table 5.3: Mean value and standard deviation (SD) of the integrated area under the hydrogen effusion peaks  $A_{eff}$ , peak position of  $LT$ ,  $HT$  and sharp peaks  $SP$  of  $a_{Si} : H$  layers deposited at various substrate temperatures  $T_S$ .

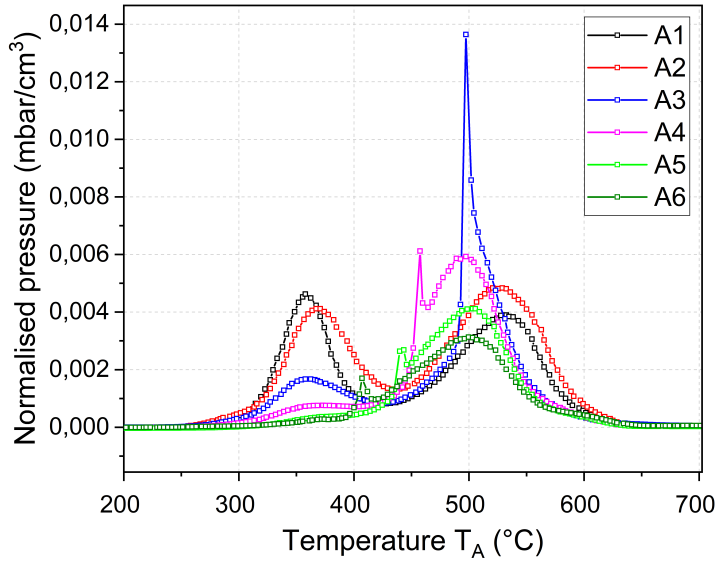


Figure 5.9: Normalized partial pressure of effused hydrogen from  $a - Si_x : H$  film deposited at various substrate temperatures  $T_S$  of 100 °C to 400 °C as a function of annealing temperature  $T_A$  [67]. The samples are divided into two groups (I and II) according to their appearance: Group I includes samples A1 and A2 without a sharp peak and Group II includes samples A3-A6 with a sharp peak, see section 5.5.

### Comparison of the NRA with the effusion mass spectroscopy and the calibration procedure

The mean values of  $A_{eff}$  show a reduction of roughly 50 % in the hydrogen effusion rate from sample deposited by 100 °C (A1) to that deposited at 400 °C (A6). The result are in correlation with the hydrogen concentration measured with the NRA technique (See Table 5.2). In Figure 5.10, the hydrogen concentration measured with the NRA method is plotted vs. the integrated area  $A_{eff}$  obtained from the effusion measurements for  $a - Si_x : H$  samples.

The individual effusion results are represented by dots and the red regression line shows the rough linear relationship. Horizontal error bars display the variation between multiple measurements of the same reference samples. The 95 % confidence interval of the regression is shown by the red highlighted area.

To determine the detection limit of the effusion measurement system, multiple blank measurements (annealing the empty quartz without the samples) are performed. The results are also plotted in Figure 5.10 approximately near zero. According to the regression analysis, the following empirical relationship is applicable for the absolute concentration of hydrogen  $C_H$ . A coefficient of determination (R square) of about 0.96 is calculated from the regression analysis.

$$C_H[at.\%] = (8.12 \pm 0.72) A_{H,eff} + (-0.18 \pm 1.253) \quad (5.7)$$

From the result, it can be concluded that effusion mass spectroscopy is a good scale for measuring hydrogen.



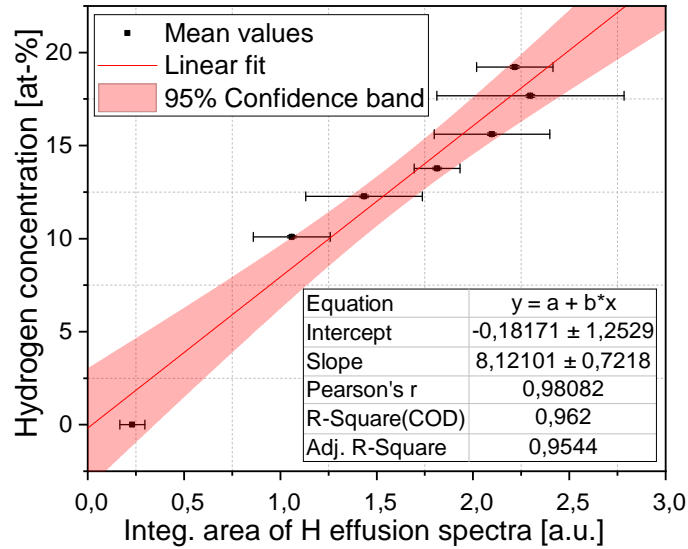


Figure 5.10: Comparison of integrated area under the hydrogen spectra measured by effusion mass spectroscopy with hydrogen concentration measured by NRA as a reference measurement.

#### 5.4.2 The advantages and the limits of effusion mass spectroscopy

##### The advantages and the possibilities

The observation of an excellent agreement with hydrogen concentration measured by nuclear reaction analysis reveals the high hydrogen sensitivity of the effusion mass spectroscopy. For further comparison, a list of some frequently used characterization methods for hydrogen detection such as Fourier-transform infrared spectroscopy (FTIR), dynamic secondary ion mass spectroscopy (SIMS), elastic recoil detection (ERD) analysis as well as nuclear reaction analysis (NRA) are presented in Table 5.4 with their detection limits and average unit prices.

|      | Detection limit                          | Average unit price   |
|------|--|----------------------|
| FTIR | $\sim 10^{20} \text{ cm}^{-3}$ [44] [68] | $\sim 100\text{K €}$ |
| SIMS | $\sim 10^{17} \text{ cm}^{-3}$ [69] [70] | $\sim 1\text{M €}$   |
| NRA  | $\sim 10^{18} \text{ cm}^{-3}$ [71] [65] | $\sim 800\text{K €}$ |
| ERDA | $\sim 10^{19} \text{ cm}^{-3}$ [72]      | $\sim 800\text{K €}$ |
| EMS  | $\sim 10^{18} \text{ cm}^{-3}$           | $\sim 100\text{K €}$ |

Table 5.4: List of some widely used characterization methods for hydrogen detection.

FT-IR spectroscopy is a highly available method to determine the hydrogen content by measuring the hydrogen bond densities. The detection limit of the FT-IR lies at  $\sim 10^{20} \text{ cm}^{-3}$ . A limit of the method is that only bonded hydrogen can be measured and the atomic hydrogen or the interstitial are not detectable. However, the FTIR spectroscopy provides a valuable information about the film structures and the bindings in a specimen.

In the second method, elastic recoil detection (ERD), a beam of  $\sim 2 \text{ MeV He}$  ions impinges on the sample. The scattered hydrogen atoms recoiled from the sample are measured with high sensitivity of  $\sim 1000 \text{ ppm}$  ( $\sim 10^{19} \text{ cm}^{-3}$ ) [72] [73]. Both, the ERD and the NRA methods operate with an ion accelerator which is costly and not widely available.

In the third method, secondary ion mass spectroscopy SIMS, a beam of focused primary ions are used to sputter material away from the surface of the sample. Dynamic SIMS is highly sensitive for surface and bulk analyses and can measure hydrogen in the range of  $\sim 10 - 100 \text{ ppm}$  ( $\sim 10^{17} \text{ cm}^{-3}$ ) [69], however it is also costly.

Effusion mass spectroscopy can provide a comparable highly sensitive hydrogen measurement of  $\sim 10^{18} \text{ cm}^{-3}$ . Considering the mentioned methods, the effusion mass spectroscopy with a simple system setup is a cost-effective alternative for measuring hydrogen. In this work, it is shown that the combination of the FTIR spectroscopy and the effusion mass spectroscopy can be optimal for the optical and the structural characterization of the hydrogenated films as well as for the estimation of hydrogen concentration.

Moreover, the measurement setup provide running experiments in various thermal conditions. For example, the effusion measurements is used for simulating the firing process for studying the impact of high temperatures on the properties of  $\text{SiN}_x : \text{H}$  layers. Most importantly, the method can cover a wide range of applications due to a broad mass detection  $m/z$  (mass to charge ratio ) of 1 to 100.

### The limits

A small diameter quartz tube is used as a vacuum chamber to achieve ultra-high vacuum (pressure of  $\sim 10^8\text{-}10^9 \text{ mbar}$ ) in a shorter period of time. Therefore, a limited size of samples can be measured with this setup. Moreover, as shown in section 5.4.1, a measurement error of about  $\pm 2 \text{ at.}\%$  is obtained for absolute hydrogen concentration determined by effusion measurement, while the NRA measurements show an error of  $0.07 \text{ at.}\%$  [66].

Effusion mass spectroscopy does not offer surface analysis such as depth profiling of hydrogen or surface mapping. However, the effusion spectrum gives indirectly some information about the film structure and the influence of the surface/interface states on the hydrogen effusion/diffusion mechanism.

## 5.5 Occurrence of hydrogen spikes and its correlation with void structure

### 5.5.1 Observation of sharp peak (SP) in effusion spectra of $a-Si_x:H$

In Figure 5.9, the hydrogen effusion graphs show two different trends depending on substrate temperature ( $T_S$ ) during the deposition of  $a-Si:H$  layers, (*group I*) the spectra of the samples A1 and A2 contain two main effusion peaks, one at *LT* of about 360 °C and one at higher temperature (*HT*) of about 530 °C and (*group II*) the hydrogen effusion of the other samples (A3–A6) show a small *LT* peak with a sharp peak (*SP*) on the rising edge of the main peak at *HT*s.

To ensure that these *SP*s are not caused by an artifact introduced by the measurement equipment, the experiments are repeated three times for each sample. The correlation between the *SP* in group II with the substrate temperature  $T_S$  and the anneal temperature  $T_A$  in which the peaks occurred during the effusion measurements are shown in Figure 5.11a and b, respectively. The height of the *SP* decreases with increasing substrate temperature  $T_S$ . In contrast, the *SP* signal increases while the peak position shifts to higher annealing temperatures  $T_A$ .

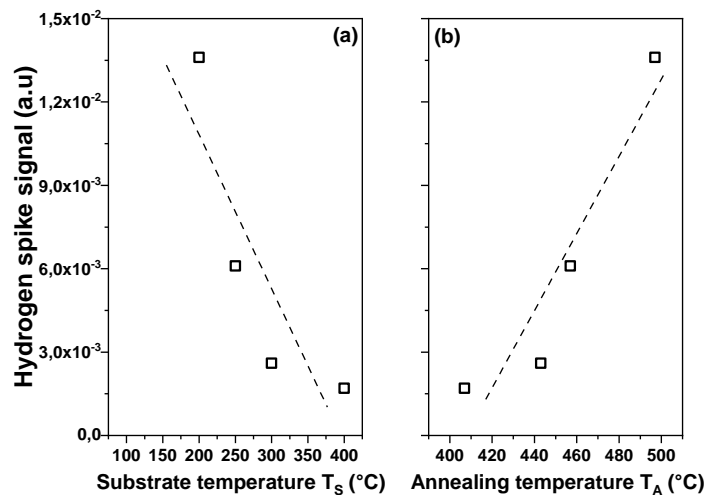


Figure 5.11: The spike of hydrogen effusion as a function of a) substrate temperature  $T_S$  and b) annealing temperature  $T_A$  [67]. The dash lines are a guide for the eyes.

### Surface morphology analysis

Light microscopy images of the samples before and after the effusion measurement are shown in Figure 5.12 a and b, respectively. Sample A1 and A2 without *SP*s in effusion spectra, are presented in a green box which reveal unchanged surfaces after the exposure of high annealing temperatures  $T_A$  during the effusion measurement. However, the other samples that include *SP*s in their effusion spectra show film deterioration after the effusion measurements in a red box. The damaged film area increases from A3 to A6 with increasing

substrate temperature  $T_S$  during the film deposition.

In addition to light microscopy images, a cross-sectional image of the sample A1 is provided

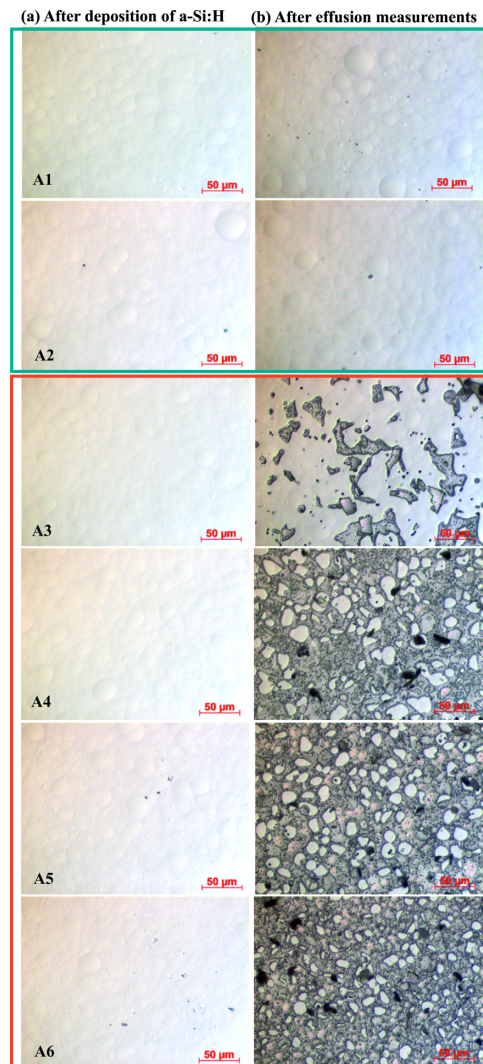


Figure 5.12: Light microscope images of sample's surfaces acquired a) as-deposited (left column) and b) after effusion measurement (right column) of  $a-Si:H$  films A1–A6 deposited at various substrate temperatures from 100 °C to 400 °C, respectively. The green box shows group I with samples A1 and A2 and the red box group II with samples A3...A6.

before effusion measurement using scanning electron microscopy (SEM) shown in Figure 5.13. The thickness of about 477 nm is measured for  $a-Si:H$  film, which is in good agreement with those presented in Table 5.2 measured by Steffens et al. [66]. The dark area indicates the existence of cavities at the interface. The measured diameter of the cavities vary and range up to 450 nm. The hypothesis that the blisters, shown by the microscopic images (after deposition) in Figure 5.12 are due to the large cavities in micrometer scale at the interface of  $Si/a-Si_x:H$  cannot be confirmed from the microscopic results.

## 5.5.2 Discussion and modeling

### Layer density/porosity and morphology

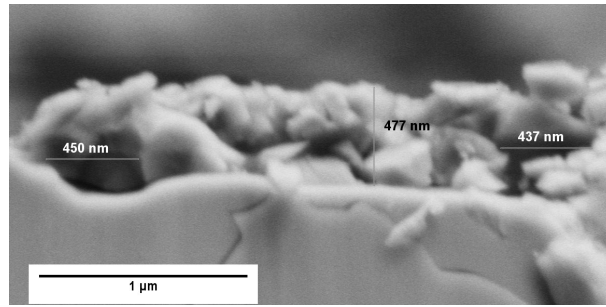


Figure 5.13: A cross-sectional view of the sample A1 deposited at substrate temperature  $T_S$  of 100 °C as deposited obtained from secondary electron microscopy SEM.

As shown in Table 5.3, the film deposition at higher substrate temperatures  $T_S$  decreases the hydrogen concentration  $C_H$  in the film. A structural analysis of the films are published previously by Steffens et al. [74]. FTIR spectroscopy is used to determine the hydrogen bond configurations and the corresponding microstructure factor  $R_{micro}$  [74]. The lower values of  $R_{micro}$  correspond to a more ordered and denser microstructure while the larger values show the less ordered and a loose structure. A reduction of  $R_{micro}$  is observed with increasing substrate temperature during the deposition from 0.5 in A1 at  $T_S = 100$  °C to 0.3 in A6 at  $T_S = 400$  °C. Thus, the amorphous network can be assumed to be denser for higher  $T_S$ .

Beyer et al. attributed the hydrogen effusion peaks to a surface desorption process within the voids followed by the rapid out-diffusion of  $H_2$  molecules at the LTs. While, the diffusion of atomic hydrogen takes place at the HTs [57] [75] [56]. A model proposed by Smets et al. indicates that the film with high hydrogen concentration and low density (high porosity) contains microscopic voids. By increasing the film density (less porous) and lowering the hydrogen concentration, surface bubble are more likely to dominate [76]. Moreover, Shanks et al. reported the interface cavities after deposition of  $a_{Si} : H$ , however, a different deposition condition is used [75].

It can be assumed, that in group I, the film deposition at low temperatures  $T_S < 200$  °C leads to a large discontinuity of the Si-Si network due to the high concentration of hydrogen and the bubbles as shown in Figure 5.13 [74]. Such a porous structure results in large cavities/voids that facilitate the  $H_2$  diffusion at low annealing temperatures. Moreover, it is reported that the effusion peak at low temperature of about 350 °C can be associated with the hydrogen released from polysilane chain-like sites  $(SiH_2)_n$  [56] [77]. The presence of micro-voids is reported by increasing the hydrogen concentration in the film higher than 14 at.% [76] [78]. Moreover, the effusion of hydrogen at low temperatures from a void-rich film can be associated with the film densification which limits the further diffusion of hydrogen.

In group II, by increasing the substrate temperature  $T_S > 200$  °C, the film growth rate increases, while the hydrogen concentration decreases (See Table 5.3). The low incorporation of hydrogen in the film decreases the network disorders and thus the film becomes denser. Therefore, the reduction of voids in the film and smaller interface cavities are expected [74].

### Hydrogen effusion in group I

Samples A2 and A4 are picked as representatives from groups I and II for a detailed study of their different thermal behaviors. The effusion spectra of these two samples are shown in Figure 5.9.

Figure 5.14a shows the peak deconvolution for the spectrum of sample A2. The fit is used to

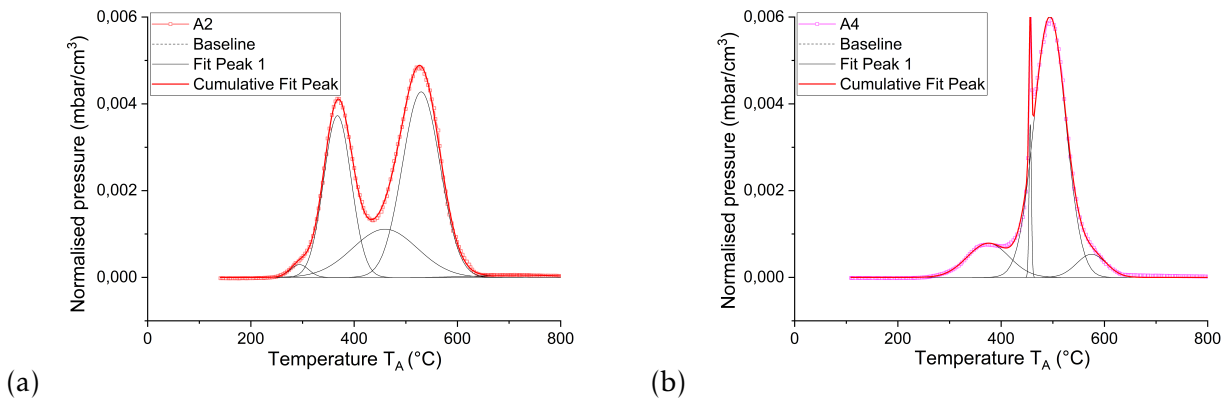


Figure 5.14: Gaussian fit of the hydrogen evolution spectra of a) sample A2 from group 1 and b) sample A4 from group 2 [67].

simplify the interpretation of differences in the effusion spectra. A list of the peak positions and the percentage fraction of integrated area among the peaks is shown in Table 5.5.

|    | P(I)<br>(°C) | Intg.<br>area<br>(%) | P(II)<br>(°C) | Intg.<br>area<br>(%) | P(III)<br>(°C) | Intg.<br>area<br>(%) | P(IV)<br>(°C) | Intg.<br>area<br>(%) | P(V)<br>(°C) | Intg.<br>area<br>(%) |
|----|--------------|----------------------|---------------|----------------------|----------------|----------------------|---------------|----------------------|--------------|----------------------|
| A2 | 294          | 2.6                  | 367           | 29.8                 | 459            | 20.8                 | 529           | 46.8                 | -            | -                    |
| A4 | -            | -                    | 375           | 13                   | 456            | 3.8                  | 500           | 76.9                 | 579          | 6.3                  |

Table 5.5: Peak position and normalized integrated effusion intensity for the Gaussian components of effusion spectra for samples A2 and A4.

The different peak positions indicate the release of hydrogen from different hydrogen bonds with various bond energies [77]. However, the diffusion of hydrogen can be limited by the defects and impurities in the film. Therefore, determining the hydrogen origins only from the effusion peaks is almost impossible.

The other factor that affects the effusion peak positions, is the film densification due to the annealing during the effusion measurement. Densification can shift the effusion peaks to higher annealing temperatures  $T_A$  [79] particularly in the low-density/porous films. A model proposed by Macco et al. indicates the time-dependent immigration of nano-voids through the film due to the annealing at temperature of  $\sim 300$  °C associated with the hydrogen diffusion [80].

In addition, a high concentration of hydrogen in the film increases the possibility of the  $H_2$  formation during the diffusion, leading to higher  $LT$  effusion peak [56]. Hydrogen effusion starts at  $T_A$  of 294 °C in sample A2 and follows by a large  $LT$  peak at 367 °C which contains

50% of the total amount of hydrogen in the film (See Table 5.5).

Shanks et al. reported that the increase of the film thickness can lead to larger bubbles at the film interface [75]. By assumption that and the fact that the rise of the substrate temperature  $T_S$  improves the adhesion of the film to the substrate, smaller interface bubbles can be expected [81] [82]. In conclusion, the void-rich structure of A2 is the reason for the smooth release of hydrogen which causes no significant damage of the film.

### Model for description of hydrogen sharp peaks (SP) in group II

Figure 5.14b presents the fitting curve of the sample A4 from Group II. As a major change in this sample, a *SP* is observed at 456 °C, followed by a large *HT* peak. This indicates that 80% of the total hydrogen in A4 is released at high annealing temperatures, higher than 400 °C. This is observed for all samples in group II.

Considering that A4 is a less porous (denser) film compared to A2 due to the higher substrate temperature  $T_S$ , the reduction of voids can inhibit the release of hydrogen at low temperatures. However, the interface blisters are more dominant in the amorphous films deposited with higher deposition temperatures reported by Smets et al. [76] [83]

During the annealing, the hydrogen atoms diffuse (1) through the film to the interface of  $Si/a-Si_x:H$  or (2) towards the surface and effuse out of the film into the ambient. The atomic hydrogen at the interface of  $Si/a-Si_x:H$  can be trapped into the interface-bubbles and form the hydrogen molecules as shown in Figure 5.15a. The excessive pressure of stored

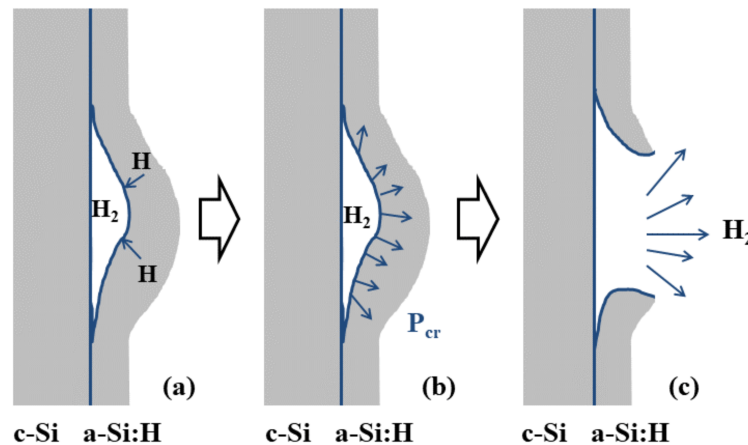


Figure 5.15: The visual model of a sharp release of hydrogen due to the excessive pressure inside interface bubbles in a film deposited at high substrate temperature  $T_S > 200$  °C which leads to the film damage [67].

hydrogen molecules in the bubble can lead to a local explosion which results in film delaminations at the position of bubble/blister. The increase of the pressure up to a critical point  $P_{cr}$  and the deterioration of the film due to the abrupt hydrogen release are modeled in Figure 5.15b and c. The illustration shows the layer structure where sizes and appearance are neglected. The mentioned explosion can be the cause of the sharp peaks in the effusion curve. After sudden release of hydrogen during the explosion, the rest hydrogen atoms release at high temperatures and from the second main peak of spectra.

It is assumed that the area of the deteriorated film is related to the size of the interface blister and the hydrogen concentration in the film. If the volume of the bubble decreases due to the higher substrate temperature, the numbers of hydrogen molecules stored in the bubble are less. This can lead to a lower hydrogen effusion during the explosion (delamination) and thus a smaller sharp peak can be observed [74]. It can explain how the sharp peaks becomes smaller from A3 to A6 as the hydrogen concentration decreases and the film density increases. Moreover, the shift of the *SP* to lower temperatures can be explained by the size of the interface bubbles.

The temperature difference between the position of the *LT* peak and the *SP* can be explained by the different time required to fill the bubbles with hydrogen before the explosion depending on the bubbles size. The difference is decreasing from the sample A3 to A6 by increasing the substrate temperature. It suggests that the volume of bubbles reduced from A3 to A6 which disagrees with the proportional relation between the bubbles diameter and the film thickness claimed by Shanks and Ley [75]. A reason for the different result might be the various layer preparations.

Based on the proposed model and the curve fittings, the hydrogen effusion from the *a-Si:H* films is resulted from following four steps,

- 1) Thermal-driven breakage of hydrogen bonds from the original bonds with various binding energies.
- 2) Hydrogen diffusion through the film with diffusion coefficient  $D_0$ .
- 3) Chemical reaction between the atomic hydrogen and the formation of molecules  $H_2$ .
- 4) Two procedures can be as follows (a) in a low-density (porous) film,  $H_2$  molecules diffuse through the void-rich film to the surface and effuse out without causing a surface damage which results in two effusion peaks at *LT* and *HT*. (b) In a compact film after desorption of near surface hydrogen and appearance of the peak at *LT*, the increase of number of the stored hydrogen molecules  $H_2$  in the interface-bubbles with certain volume  $V_{Vacancy}$  rises the pressure to a critical point which leads an abrupt release of hydrogen (explosion) and formation of a sharp peak.

Time to fill the bubbles is indicated by the difference between the peak position of the *LT* and the *SP*, which also depends on the size of the bubbles.



## Chapter 6

# Investigation and Characterization of Amorphous $SiN_x : H$ Passivation Layers Regarding Its Applications for Si Solar Cells

### 6.1 Understanding the properties of PECVD deposited $SiN_x : H$ passivation layers

*Hydrogen passivation is the result of two process steps in the commercial production of silicon solar cells, (I) deposition of hydrogenated anti-reflective coating at low temperatures and (II) subsequent metallization of the front contact at high temperatures (firing process). Amorphous silicon nitride layers deposited by PECVD at low temperatures show high concentrations of hydrogen, a promising passivation quality and adjustable refractive index which are widely used as anti-reflective coating and passivation films in solar cell processing [8] [10] [25] [51]. In this section, a systematic analysis is carried out to investigate the role of deposition parameters on structural, optical and electrical properties of PECVD deposited  $SiN_x : H$  layers. The aim of this work is to study the influence of film properties on passivation quality and hydrogen transport mechanism during firing.*

#### 6.1.1 Results

##### **I The study of deposition parameters by using Design of Experiment (DoE)**

The definition of optimal parameters lies in the correct selection and introduction of appropriate Design of Experiments (DOE) in the earliest phase of process and product development cycles. To choose a suitable experimental design, the objectives of the experiment and the number of factors under investigation must be considered. In this study, a screening objective is performed to select and screen the significant deposition factors that

influence the most the properties of hydrogenated amorphous  $SiN_x : H$  films deposited by PECVD technique.

### DoE: Experimental steps

A two-level full-factorial design is performed to investigate the effects of the deposition factors with the highest and the lowest adjustable levels of our PECVD system for each factor. In this design, if there is  $k$  factors which run at 2 level, the number of different combinations of the levels will be  $2^k$ . Running the full possible combinations of the factors lead to estimation of all main and interaction effects. For example, in a full-factorial design with three factors ( $A$ ,  $B$  and  $C$ ), there will be three main effects, three two-factor interactions and one three-factor interaction. The effects will be described in a full-model as follows,

$$Y = a_0 + a_1A + a_2B + a_3C + a_{12}AB + a_{13}AC + a_{23}BC + a_{123}ABC. \quad (6.1)$$

The coefficient  $a$  can be estimated in a full-design.

In addition to the full-factorial design, center points are added to set halfway between the low and high settings. Without the centers, the factorial designs would assume that there is a linear relationship between each  $X$  and  $Y$ , however if the relationship has a curvature, a factorial design would be misleading. Double side polished p-doped float zone (FZ) Si wafers with thicknesses of  $250 \mu m$  with  $\langle 100 \rangle$  orientation and a resistivity of  $\sim 1-2 \Omega.cm$  are used for the plasma deposition of  $SiN_x : H$  on both sides of the wafers to achieve uniform lifetime samples. The main deposition parameters, substrate temperature  $T_S$ , gas flow ratio  $R = [NH_3]/[NH_3 + SiH_4]$ , total gas pressure, total gas flow and plasma power are studied. Concluding, forty samples are deposited by  $SiN_x : H$  layers on both sides. Table 6.1 shows the investigated deposition parameters ranges as well as the value of center points. After measuring the output parameters after deposition, samples are fired at a set peak firing of  $\sim 800 \text{ }^\circ C$  for about 1 min.

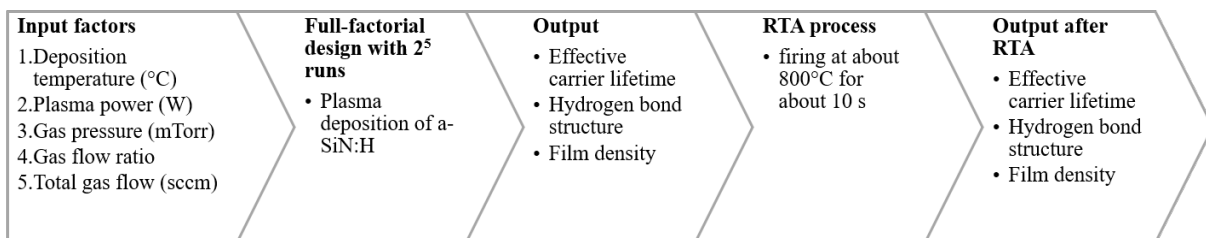


Figure 6.1: Step by step experimental flow chart of design of experiment (DoE).

Figure 6.1 illustrates the step-by-step experimental procedure. The effective minority charge carrier lifetime  $\tau_{eff}$ , hydrogen bond densities of Si-H and N-H and the film density as a function of Si-N bond density are measured for as-deposited layers and after firing and used as response variable in this optimization experiments. An analysis of variance (ANOVA) is performed to provide an interpretation and insightful view into the overall process. The so-called F-test generates the additional data that are consistent with the proposed regression

models. More details on the DoE process and the data analysis can be found in Appendix A. The thicknesses of deposited  $SiN_x : H$  films are measured by using a spectroscopic

| Level/Factor | Substrate temperature $T_S$ [°C] | Total pressure [mTorr] | Plasma power [W] | $R$ | Total gas flow [sccm] |
|--------------|----------------------------------|------------------------|------------------|-----|-----------------------|
| High         | 400                              | 1000                   | 150              | 0.9 | 1500                  |
| Center       | 300                              | 750                    | 100              | 0.5 | 1000                  |
| Low          | 200                              | 500                    | 50               | 0.1 | 500                   |

Table 6.1: List of deposition factors used for PECVD deposited  $a - SiN_x : H$  films with two-level full factorial design including the center points.

ellipsometry and the minority carrier lifetime are obtained at the minority carrier density of  $10^{15} \text{ cm}^{-3}$ . The hydrogen bond densities are calculated from the absorption spectra acquired from FTIR spectroscopy by using the model introduced by Lanford et al. [44] (See section 4.1). Once the deposited samples are characterized, they went through firing at a set peak temperature of 800 °C for about 1 min (actual sample temperature of 750 °C) similar to industrial rapid thermal annealing (RTA) process for comparing the results before and after firing.

### Significant deposition parameters as a result of statistical design (DoE)

Figure 6.2 displays the influence of deposition factors on the hydrogen bond structure in  $SiN_x : H$  as well as the effective carrier lifetime  $\tau_{eff}$  for as-deposited layers and after firing. Si-H and N-H bonds are calculated from the IR absorption spectra of the films at wavenumbers of  $\sim 2100 \text{ cm}^{-1}$  and  $\sim 3350 \text{ cm}^{-1}$ , respectively. The bond densities are normalized to the film thicknesses. The standardized effect of an individual factor (as input) on the corresponding film properties (as outputs) are normalized to 1. The results show that the gas flow ratio  $R = [NH_3]/[NH_3 + SiH_4]$  has the strongest effect on the hydrogen bond structure and the film stoichiometry shown with a blue area. While the substrate temperature  $T_S$  (second large area) shows high impact on the minority carrier lifetime  $\tau_{eff}$  as a measure of passivation quality. Moreover, the amount of N-H in the film is clearly affected by the deposition temperature. The gas pressure with a yellow colored area show almost similar effects as  $T_S$ . The other two factors, plasma power and total gas flow, have low influence on the hydrogen bonding and the passivation quality of  $SiN_x : H$  films.

## II The influence of gas flow ratio ( $R$ ) on $SiN_x : H$ properties

As a result of the DoE analysis, the gas flow ratio ( $R = [NH_3]/[NH_3 + SiH_4]$ ) and the substrate temperature are the most significant parameters to achieve good quality passivation and to control the hydrogen bonding concentration in  $SiN_x : H$  films. Therefore, further experiments are performed to investigate the influence of these factors in more detail.

### The influence of $R$ on optical properties of $SiN_x : H$ layers

Table 6.2 shows the values of  $R$  used for deposition of polished n-doped FZ-Si wafers with a resistivity of 1-5  $\Omega \cdot \text{cm}$  and a thickness of 250  $\mu\text{m}$ . The other deposition parameters

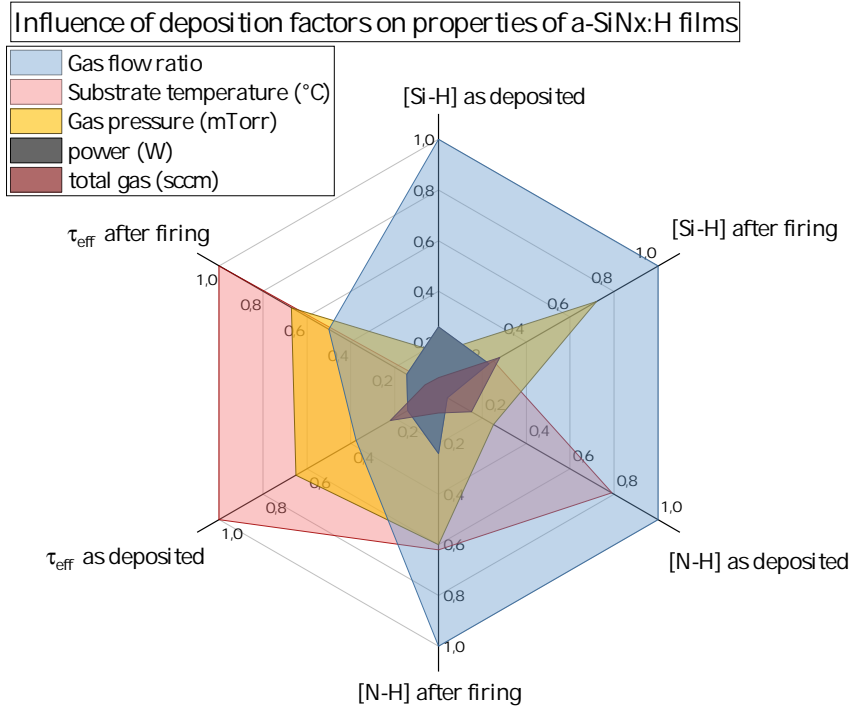


Figure 6.2: Influence of five adjustable PECVD deposition factors on the hydrogen bond densities and the passivation quality of  $a-SiN_x:H$  layers.

| $R$ | $d(nm)$ | $G(nm/min)$ | $n$  | $k$     | $E_g(eV)$         | $Si/N$ |
|-----|---------|-------------|------|---------|-------------------|--------|
| 0.1 | 142     | 47          | 3.02 | 4.63E-2 | $1.80 \pm 0.009$  | 2.25   |
| 0.3 | 115     | 38          | 2.47 | 9.32E-3 | $2.018 \pm 0.005$ | 1.51   |
| 0.5 | 94      | 31          | 2.11 | 6.10E-5 | $2.28 \pm 0.005$  | 1.02   |
| 0.7 | 86      | 29          | 1.92 | 1.56E-6 | $3.6 \pm 0.005$   | 0.77   |
| 0.9 | 69      | 23          | 1.86 | 9.57E-5 | $3.76 \pm 0.002$  | 0.69   |

Table 6.2: A list of measured and calculated optical properties of  $a-SiN_x:H$  films deposited with various gas flow ratios  $R$  on polished FZ-Si wafers.

including a plasma power of 50 W, a gas pressure of 750 mTorr, a total gas flow of 1000 sccm and a temperature of 400 °C are kept constant for all samples.

After deposition, the thicknesses  $d$ , the refractive indexes  $n$  and the extinction coefficient  $k$  of the deposited  $SiN_x : H$  layers are measured at wavelength of 633 nm by spectroscopic Ellipsometry. By fitting the spectral ellipsometric data using the Tauc-Lorentz and Cody-Lorentz models for amorphous solids [84], the optical band gap  $E_g$  of the silicon nitride films is determined. The growth rate  $G$  of  $SiN_x : H$  films is calculated from the measured film thicknesses. Moreover, in order to determine the  $Si/N$  ratios, equation 6.2 is used from the measured refractive index at the wavelength of 633 nm [24]. All measured and calculated values are listed in Table 6.2.

$$n = 1.35 + 0.74 \frac{[Si]}{[N]} \quad (6.2)$$

The variation of the refractive index, the calculated  $\text{Si}/\text{N}$  and the optical band gap  $E_g$  are illustrated in Figure 6.3a and 6.3b as a function of gas flow ratio ( $R$ ). By increasing  $R$  from 0.1

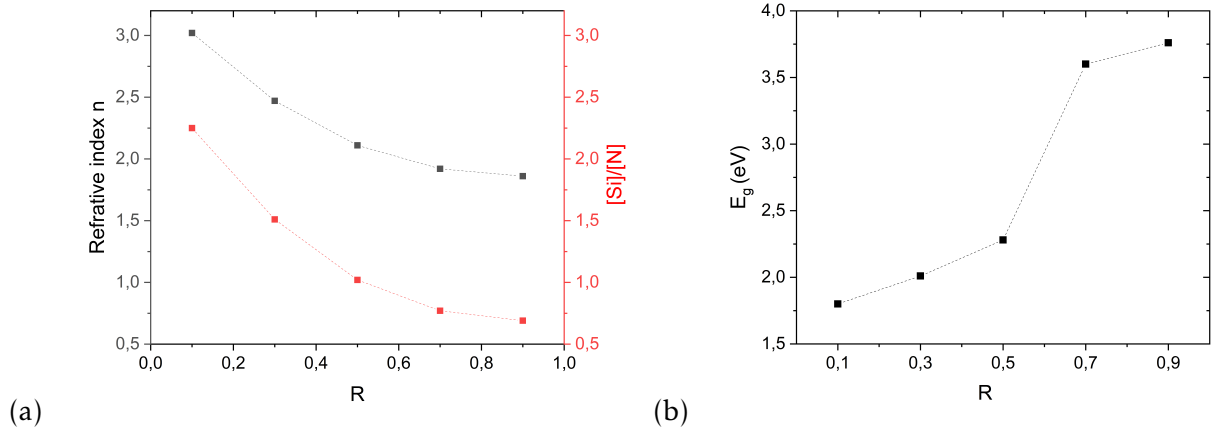


Figure 6.3: a) Refractive index  $n$  and calculated  $\text{Si}/\text{N}$  as a function of gas flow ratio  $R$  used during deposition, b) optical band gap  $E_g$  of  $a\text{-SiN}_x : \text{H}$  films vs.  $R$ . The lines connecting points are a guide to the eyes.

to 0.9, both refractive index and corresponding  $\text{Si}/\text{N}$  values are reduced from 3 to 1.9 and from 2.25 to 0.65, respectively. This is associated with a 50 % reduction in the growth rate from 47  $\text{nm}/\text{min}$  to 23  $\text{nm}/\text{min}$ . Furthermore, the optical band gap  $E_g$  of  $\text{SiN}_x : \text{H}$  film grows rapidly from 1.80 eV to 3.76 eV with increasing gas flow ratio.

#### The influence of $R$ on bond configuration in $\text{SiN}_x : \text{H}$ layers

The normalized IR absorbance spectra for the  $\text{SiN}_x : \text{H}$  films deposited at various  $R$  are shown in Figure 6.4 which is centered around the Si-N stretching mode. The results of as-deposited and fired samples are displayed by solid and dashed lines, respectively.

The absorption spectra is normalized to the film thicknesses. Additional to the Si-N stretching mode at 840  $\text{cm}^{-1}$ , Figure 6.4 presents Si-H wagging mode at 650  $\text{cm}^{-1}$  and N-H wagging mode at 1150  $\text{cm}^{-1}$  similar to those reported earlier by Scradera et al. [85]. The intensity of the bonds are determined using Lanford model [44] and is correlated to the integrated area under the corresponding peaks.

The results after deposition show that a growing N-H shoulder arise with increasing  $R$ . Moreover, the Si-N intensity increases by rise of gas flow ratio, however, it does not appear for  $R=0.9$ . Regarding the Table 6.2, the increase of Si-N bond density is correlated with the reduction of  $n$  and  $\text{Si}/\text{N}$ . After firing, the Si-N and Si-H intensity increase compared to the results after deposition while the N-H shoulder drops.

Figures 6.5a and 6.5b show the IR absorbance of the Si-H- and N-H-stretching modes with identical color code. The intensity of the Si-H peak clearly decreases with increasing  $R$ . A shift of the peak position from 2100  $\text{cm}^{-1}$  to 2175  $\text{cm}^{-1}$  is observed, which correlates with the increase of the gas flow ratio  $R$  and reduction of  $\text{Si}/\text{N}$  value in the film (See Table 6.2). After firing, the Si-H intensity follows the similar trend, although it changes differently in various

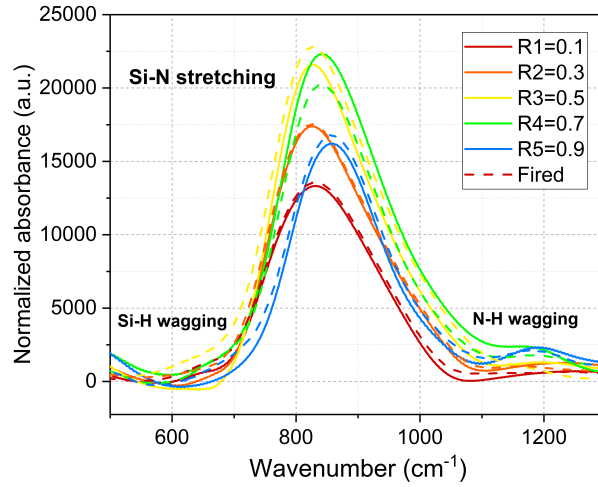


Figure 6.4: FT-IR absorption spectrum of polished FZ silicon wafers deposited by  $SiN_x : H$  at various gas flow ratios  $R$  a) as-deposited b) after firing process.

samples. In contrast to the Si-H bond, the N-H bond density increases by increase of  $R$ . After firing, the N-H intensity increases in all samples.

#### The influence of $R$ on effective minority charge carrier lifetime

To study the impact of the gas flow ratio  $R$  as a significant factor of deposition on the passivation quality of  $SiN_x : H$  films, the effective minority charge carrier lifetimes  $\tau$  are measured and compared.

The lifetime profiles are presented in Figure 6.6 as a function of minority carrier density for  $SiN_x : H$  layers after deposition and after the firing. The results are listed in Table 6.3 at the minority carrier density of  $10^{15} \text{ cm}^{-3}$ . After deposition, an increase of charge carrier lifetime from about  $10 \mu\text{s}$  to  $2 \text{ ms}$  is achieved with decreasing  $R$  from 0.9 to 0.1. A relatively large collapse of the carrier lifetime is observed as  $R$  increased from 0.7 to 0.9. After firing, the results follow the similar trend to those after deposition. Samples  $R0.1$ ,  $R0.3$  and  $R0.5$  show a decrease in charge carrier lifetime after firing  $\tau_{fired}$ , while  $R0.7$  and  $R0.9$  indicate a slight increase.

| $R$ | $\tau_{as\ deposited} (\mu\text{s})$ | $\tau_{fired} (\mu\text{s})$ |
|-----|--------------------------------------|------------------------------|
| 0.1 | 1965                                 | 1717                         |
| 0.3 | 844                                  | 789                          |
| 0.5 | 523                                  | 370                          |
| 0.7 | 414                                  | 482                          |
| 0.9 | 13                                   | 15                           |

Table 6.3: The effective carrier lifetime measured at a minority carrier density of  $10^{15} \text{ cm}^{-3}$  for polished FZ-Si wafers deposited by  $SiN_x : H$  films with various gas flow ratios  $R$ .

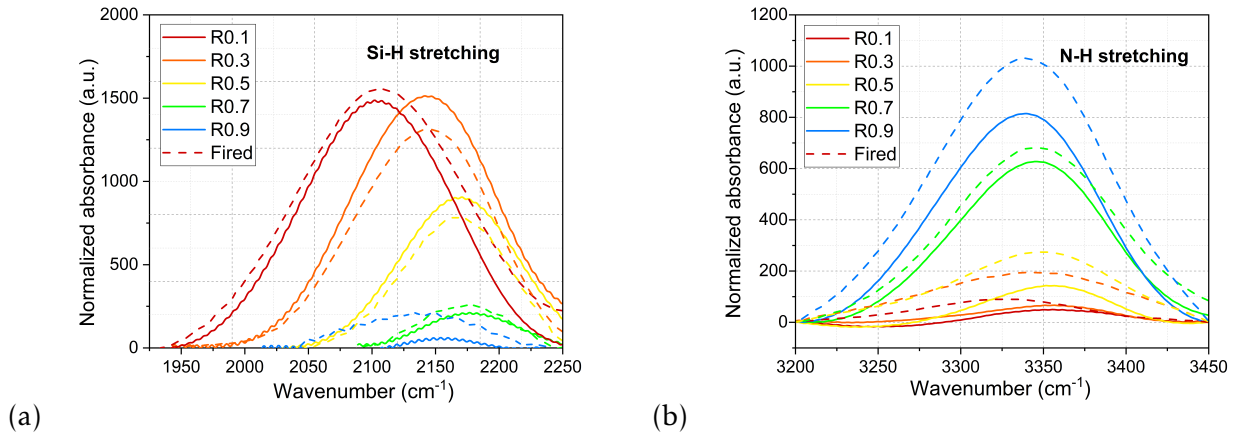


Figure 6.5: [Si-H] bonds in stretching vibration modes obtained from FTIR measurement performed on polished FZ Si wafers deposited by  $a - SiN_x : H$  at various gas flow ratios  $R$  a) as-deposited b) after firing process.

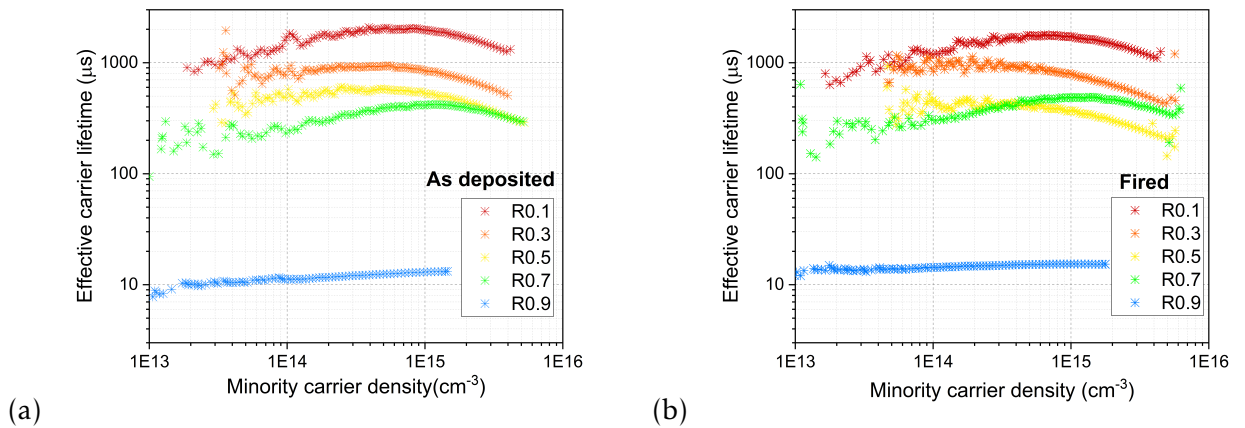


Figure 6.6: Light intensity dependent effective carrier lifetime of different  $SiN_x : H$  layers deposited on planar FZ-Si wafers with various gas flow ratios  $R$  a) as deposited b) after firing process.

### The influence of $R$ on hydrogen effusion from $SiN_x : H$ layers

To determine the hydrogen concentration in the deposited  $SiN_x : H$  and to monitor the hydrogen mobility during firing process, samples deposited with various  $R$  are measured by the effusion mass spectroscopy. A small piece of the samples are annealed up to 1200 °C at constant heating rate  $\beta$  of 20 °C/min.

In order to remove the residual hydrogen from the measurement chamber, it is heated up to 1000 °C for about 10 min prior to the measurements. Figure 6.7 shows the partial pressure of effused  $H_2$  molecules from  $SiN_x : H$  layers as a function of annealing temperature  $T_A$ . The spectra are normalized to the volumes of the films. Mainly, three different hydrogen effusion behaviours can be described,

(i)  $R0.1$  shows one main peak at a relatively low temperature  $LT_A$  of 625 °C and no hydrogen is effused from the sample above 800 °C. In contrast, the rest of the samples show spectra with two main peaks.

- (ii) In R0.3, R0.5 and R0.7, the spectra consist of two peaks, at low temperature  $LT_A$  and at high temperatures  $HT_A$ . Both peaks shift to higher temperatures as the gas flow ratio increases. Hydrogen is released at temperature up to  $\sim 900$  °C in R0.3 and R0.5 and 1100 °C in R0.7.
- (iii) R0.9 shows a main peak at  $HT_A$  of  $\sim 900$  °C and a small peak at  $LT_A$  at 580 °C. The release of hydrogen is observed at temperatures up to 1100 °C.

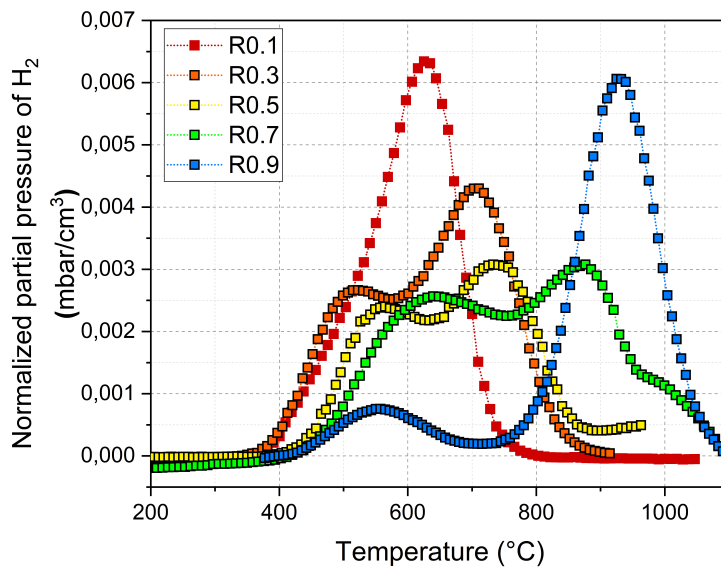


Figure 6.7: Partial pressure of effused  $H_2$  gas molecules from  $SiN_x : H$  films deposited at various gas flow ratios  $R$  normalized to the film volume as a function of annealing temperature.



### III The influence of substrate temperature ( $T_S$ ) on properties of $\text{SiN}_x : \text{H}$ layer

Analogue to the gas flow ratio, the substrate temperature  $T_S$  as a further significant deposition factor is studied in more detail. Polished n-type FZ-Si wafers are deposited on both sides with  $\text{SiN}_x : \text{H}$  layers at different substrate temperatures  $T_S$  from 100 °C to 400 °C. The intermediate gas flow ratio  $R0.5$  is used for deposition of this set of samples.

#### The influence of $T_S$ on optical properties of $\text{SiN}_x : \text{H}$ layers

The optical parameters, the film thickness  $d$ , the refractive index  $n$  and the extinction coefficient  $k$  of these set of samples are measured after deposition. The results are shown in Table 6.4. Moreover, the  $\text{Si}/\text{N}$  values are calculated by equation 6.2.

Figure 6.8a shows the  $n$  and the  $\text{Si}/\text{N}$  values and Figure 6.8b the variation of the calculated

| $T_S$ (°C) | $d$ (nm) | $G$ (nm/min) | $n$  | $k$     | $E_g$ (eV)       | $\text{Si}/\text{N}$ |
|------------|----------|--------------|------|---------|------------------|----------------------|
| 100        | 503      | 50           | 1.85 | 1.53E-5 | $2.81 \pm 0.006$ | 0.676                |
| 150        | 449      | 45           | 1.88 | 8.25E-5 | $2.69 \pm 0.007$ | 0.716                |
| 200        | 398      | 40           | 1.94 | 9.61E-5 | $2.48 \pm 0.006$ | 0.797                |
| 250        | 359      | 36           | 1.99 | 9.02E-5 | $2.56 \pm 0.005$ | 0.865                |
| 300        | 334      | 33           | 2.03 | 1.37E-4 | $2.50 \pm 0.004$ | 0.919                |
| 350        | 319      | 32           | 2.07 | 2.50E-4 | $2.46 \pm 0.005$ | 0.973                |
| 400        | 302      | 30           | 2.1  | 3.48E-4 | $2.29 \pm 0.008$ | 1.014                |

Table 6.4: A list of optical properties of  $\text{SiN}_x : \text{H}$  films deposited with various substrate temperatures  $T_S$ .

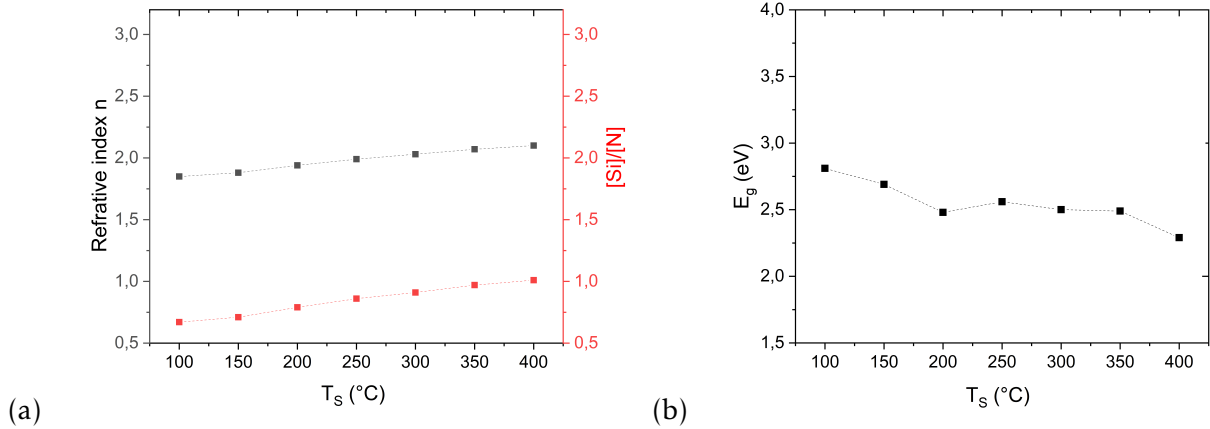


Figure 6.8: a) Refractive index  $n$  and calculated  $\text{Si}/\text{N}$  as a function of substrate temperature  $T_S$  during deposition, b) optical band gap  $E_g$  of  $\text{SiN}_x : \text{H}$  films vs.  $T_S$ . The lines connecting points are a guide to the eyes.

optical band gap  $E_g$  as a function of the substrate temperature. A slight increase in the refractive index from 1.85 to 2.1 and corresponding  $\text{Si}/\text{N}$  values from 0.67 to 1.014 are observed as the  $T_S$  increased from 100 °C to 400 °C. While the thicknesses of the films and the corresponding film growth rate  $G$  reduced from 503 nm to 302 nm and from 50 nm/min to 30 nm/min. Furthermore, a moderate reduction of the band gap from 2.81 eV to 2.29 eV is observed as the  $T_S$  increased.

### The influence of $T_S$ on bond configuration in $SiN_x:H$ layer

Similar to the last set of samples, the bond configuration of  $SiN_x:H$  films deposited at various  $T_S$  are studied via FTIR spectroscopy. The normalized peaks of Si-N ( $845\text{ cm}^{-1}$ ), Si-H ( $\sim 2160\text{ cm}^{-1}$ ) and N-H ( $3350\text{ cm}^{-1}$ ) are shown in Figure 6.9 and 6.10 as a function of wave number. The solid lines represent the spectra after deposition of  $SiN_x:H$  films and the

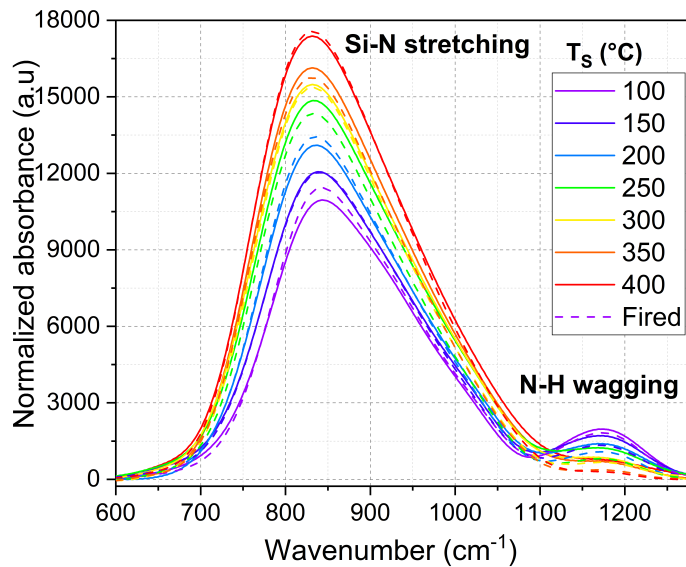


Figure 6.9: IR absorption peak of Si-N stretching mode obtained from FTIR measurement performed on polished FZ-Si wafers deposited by  $SiN_x:H$  at various substrate temperatures  $T_S$  as-deposited and after firing process.

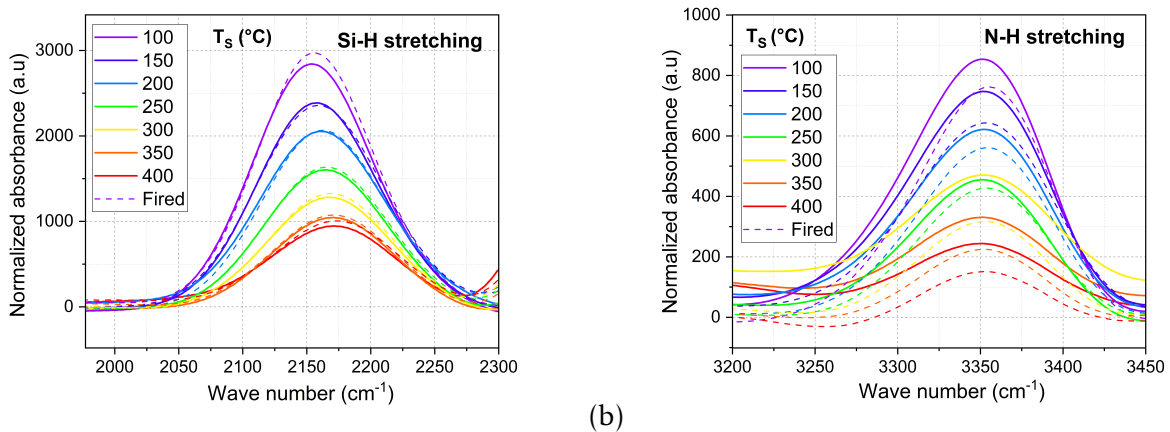


Figure 6.10: IR absorption peak of [Si-H] and [N-H] stretching mode obtained from FTIR measurement performed on polished FZ-Si wafers deposited by  $a-SiN_x:H$  at various substrate temperatures  $T_S$  as-deposited (straight lines) and after firing process (dashed lines).

dashed lines show the results after firing. The peak height of Si-N stretching mode is increased by rising  $T_S$ . The Si-N bond intensity increased after firing, except for the samples deposited at 250 °C and 350 °C. The N-H wagging shoulder at  $1150\text{ cm}^{-1}$  increases with the reduction

of the  $T_S$ , while it decreases after firing for all samples. In Figure 6.10, the increase of the  $T_S$  leads to a reduction of the Si-H and N-H peaks after deposition. This implies that the total concentration of bonded hydrogen decreases in the film as deposition takes place at higher temperatures. Moreover, the Si-H peak position shifts slightly to the higher wave numbers as the temperature increases. After firing, the Si-H bond intensities change irregularly, while reduction of N-H bonds are observed for all samples.

### The influence of $T_S$ on effective minority charge carrier lifetime

The effective minority charge carrier lifetimes are determined for samples deposited by  $\text{SiN}_x : \text{H}$  at different substrate temperatures  $T_S$  after deposition and after the firing. Results are shown in Figure 6.11.

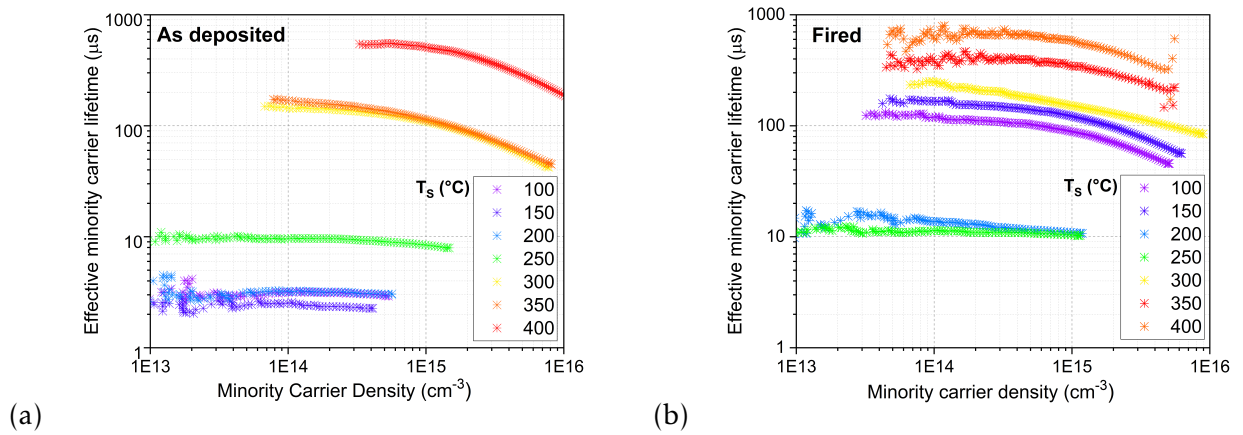


Figure 6.11: Effective minority carrier lifetime of planar FZ-Si wafers deposited by  $a\text{-SiN}_x : \text{H}$  films at various substrate temperatures  $T_S$  a) as-deposited layers b) after firing process.

| $T_S$ (°C) | $\tau_{as\ deposited}$ ( $\mu s$ ) | $\tau_{Fired}$ ( $\mu s$ ) |
|------------|------------------------------------|----------------------------|
| 100        | 3                                  | 88                         |
| 150        | 2                                  | 121                        |
| 200        | 3                                  | 11                         |
| 250        | 8.3                                | 10.3                       |
| 300        | 108.8                              | 151                        |
| 350        | 113.6                              | 344                        |
| 400        | 503                                | 584.6                      |

Table 6.5: Effective minority carrier lifetime obtained for SiN coated planar FZ-Si with various substrate temperature  $T_S$  as deposited ( $\tau_{as\ deposited}$ ) and after firing ( $\tau_{Fired}$ ).

Table 6.5 lists the measured charge carrier lifetimes after deposition of  $\text{SiN}_x : \text{H}$  ( $\tau_{as\ deposited}$ ) and after firing ( $\tau_{Fired}$ ) at excess carrier density of  $10^{15} \text{ cm}^{-3}$ . An overall increase of the charge carrier lifetime is achieved by increasing substrate temperature. The maximum value of  $\tau_{as\ deposited}$  is about  $\sim 500 \mu s$  at  $T_S$  of 400 °C. Substrate temperatures below 250 °C show almost no or very poor passivation quality. After firing, the charge carrier lifetimes increase for all samples. The increase is larger for the samples with  $T_S$  of 100 °C and 150 °C. The

maximum charge carrier lifetime is  $\sim 580 \mu s$  for the sample deposited at  $T_S$  of  $400 \text{ }^\circ\text{C}$ . No significant change in the charge carrier lifetime is found for  $SiN_x : H$  deposited at  $T_S$  of  $250 \text{ }^\circ\text{C}$  after firing.

### The influence of $T_S$ on hydrogen effusion from $SiN_x : H$ layer

The effusion of hydrogen from the  $SiN_x : H$  layers deposited at different substrate temperatures  $T_S$  is determined by effusion mass spectroscopy. As mentioned, the gas flow ratio of  $R_{0.5}$  is used for the deposition of this set of samples. The normalized partial pressure

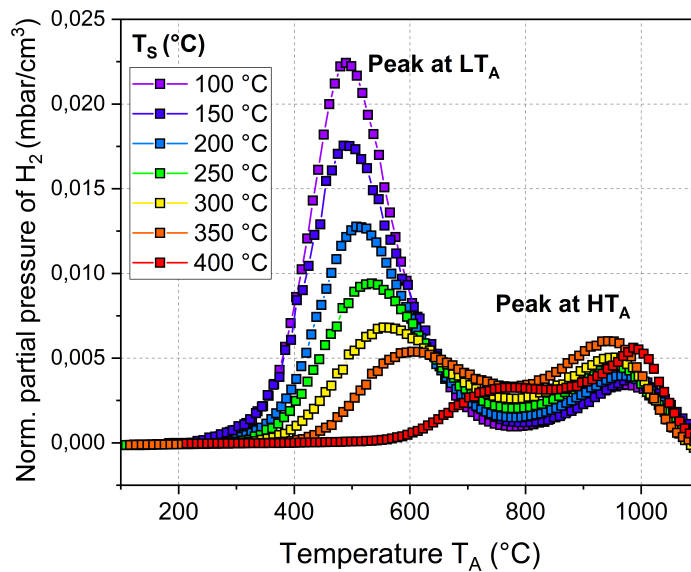


Figure 6.12: Partial pressure of effused  $H_2$  gas molecules from the  $SiN_x : H$  films deposited at various substrate temperatures  $T_S$  normalized to film volume as a function of annealing temperature.

of  $H_2$  is plotted as a function of the annealing temperature  $T_A$  in Figure 6.12. All spectra consist of two peaks. Hydrogen peak at  $LT_A$  decreases by increasing the substrate temperature  $T_S$ . Moreover, the increase of the  $T_S$  shifts the  $LT_A$  peak to higher annealing temperatures from  $T_A \sim 422 \text{ }^\circ\text{C}$  for the sample with  $T_S = 100 \text{ }^\circ\text{C}$  to  $T_A \sim 570 \text{ }^\circ\text{C}$  for the sample with  $T_S = 100 \text{ }^\circ\text{C}$ . The peak at high temperature ( $HT_A$ ) increases with rise of the  $T_S$ . The peak position at  $HT$  shifts from  $T_A \sim 800 \text{ }^\circ\text{C}$  when  $T_S \geq 250 \text{ }^\circ\text{C}$  to  $T_A \sim 850 \text{ }^\circ\text{C}$  when  $T_S < 250 \text{ }^\circ\text{C}$ . Substrate temperatures below  $350 \text{ }^\circ\text{C}$  leads to a dominant  $LT_A$  peak in the spectra. All samples show no hydrogen release above  $1000 \text{ }^\circ\text{C}$ .

### 6.1.2 Discussion

The role of deposition parameters on the properties of  $\text{SiN}_x:H$  films has been investigated for better understanding of the hydrogen transport mechanism at high temperatures during firing. Upon this, possible reasons for different passivation qualities and optical properties can be discussed to provide an optimal layer for high-efficiency solar cells.

#### I The influence of the two significant deposition parameters, $R$ and $T_S$ , on $\text{SiN}_x:H$ properties

Considering the results from DoE analysis, two significant deposition parameters, the gas flow ratio  $R$  and the substrate temperature  $T_S$ , are studied in more detail and results are presented in sections II and III. In this section, the influence of these two parameters on the properties of  $\text{SiN}_x:H$  layers will be discussed in detail. For better comparison, a summary of the results shown in the last section are presented in Figure 6.13a and 6.13b with regards to the variation of the gas flow ratio and the substrate temperature, respectively.

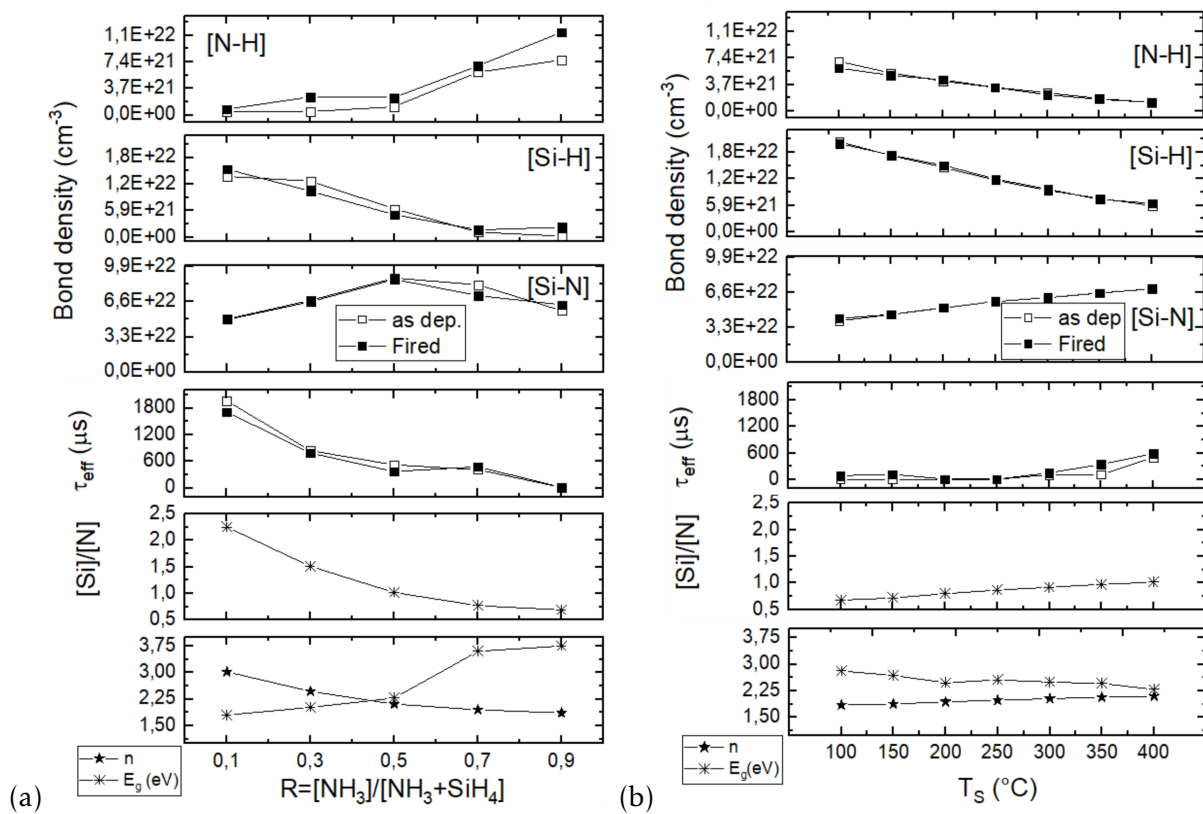


Figure 6.13: The influence of a) the gas flow ratio  $R$  (at  $T_S = 400^\circ\text{C}$ ) and b) the substrate temperature  $T_S$  (with  $R = 0.5$ ) during the deposition on the optical and the electrical properties of the PECVD-deposited  $\text{SiN}_x:H$  passivation layers.

### The impact of the gas flow ratio $R$ on the optical and the compositional properties of $SiN_x : H$

The optical ( $n, k$ ) and compositional (atomic bonds) properties of  $SiN_x : H$  layers as a function of  $R$  are shown in Figure 6.13a in the top and the bottom diagrams. A strong reduction of the refractive index ( $n$ ) and the corresponding  $Si/N$  values with increasing  $R$  implies structural change from Si-rich to N-rich  $SiN_x : H$  film. The results are in good agreement with those previously reported [43] [10]. Sinha et al. indicated that the film density ( $\rho$ ) of the amorphous  $SiN_x : H$  increases from less than  $2.1 \text{ g.cm}^{-3}$  up to  $\sim 2.8 \text{ g.cm}^{-3}$  when the  $Si/N$  decreases from 1.5 to above 0.75 [86].

The increase of silane flow forces the formation of disilane ( $Si_2H_6$ ) as dominant plasma precursor, while more ammonia arise the amount of tri- or tetra-aminosilanes ( $Si(NH_2)_3$ ,  $Si(NH_2)_4$ ) [87]. Low deposition rate is observed when ammonia flow is higher. This can be explained by a decrease of the plasma residence time and an increase in  $Si(NH_2)_4$  compared to  $Si(NH_2)_3$  [88] [87].

Furthermore, the optical band gap ( $E_g$ ) increases with  $R$  as also reported by others [87] [64]. The increase of the band gap occurs gradually up to  $\sim 2 \text{ eV}$  in R0.5 and then rapidly to  $\sim 3.5 \text{ eV}$  in R0.9. Robertson et al. indicated that a rapid increase in the band gap of  $SiN_x : H$  is due to the percolation threshold in the film network at  $x = N/Si > 1.1$  ( $Si/N < 0.9$ ,  $R > 0.5$ ) [64]. He showed that the band edges differs due to various bonding configuration, where the Si-Si bonds are replaced by stronger Si-N bonds at higher  $x$  (lower  $Si/N$ ). The largest band gap of  $\sim 3.7 \text{ eV}$  is achieved in this work for stoichiometric  $SiN_x : H$  film with the lowest  $Si/N$  values of 0.65 ( $x \approx 1.5$ ) deposited by R0.9.

The bond structure of the films are studied through the IR absorption spectra. The gas flow ratio  $R$  strongly affects the hydrogen configuration in the as-deposited  $SiN_x : H$  shown in Figure 6.13a with hollow squares. The differences between the films are more apparent in the hydrogen distribution in form of Si-H and N-H bonds rather in the total hydrogen content. The conversion of disilane-rich plasma to saturated aminosilane through different  $R$  varies the hydrogen bonded to Si or N. The peak position of the Si-H in IR absorption spectra appears at higher wave numbers as the  $Si/N$  ratio decreases (see Figure 6.5a). It is reported that a different back bonding of the Si-H bond can influence the peak position [89] [29]. A model described by Verlaan et al. determines the peak position of the Si-H as a result of back bonding configuration [23]

$$\omega(\text{cm}^{-1}) = 1630 + 49 \sum_{j=1}^3 \chi_{A_j} \quad (6.3)$$

with the sum of effective electronegativity  $\chi_{A_j}$  of  $j^{\text{th}}$  neighbor of Si-H bond. N related bonds with higher electronegativity ( $\chi_N = 3.04 > \chi_{Si} = 1.9$ ) can result in a peak at higher wave numbers.

The largest peak in the FTIR spectra is Si-N stretching at about  $840 \text{ cm}^{-1}$  as shown in Figures 6.4 and 6.9. It is found that Si-N bonds decrease once ammonia flow overcomes silane during deposition ( $R \geq 0.5$ ). It is associated with a strong increase in N-H bonds. This can be

explained by the absence of silane in the plasma, which leads to amino radicals forming more N-H rather than Si-N.

### The impact of $R$ on passivation quality of $SiN_x:H$

Besides the structural changes, the effective carrier lifetime ( $\tau_{eff}$ ) as a measure of passivation quality of  $SiN_x:H$  layers varies with different gas flow ratios. The effective carrier lifetime for well-passivated surfaces with carrier diffusion length greater than the sample width  $W$  can be determined [90] by,

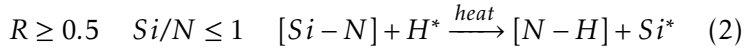
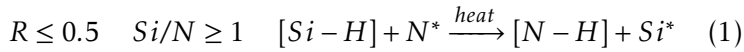
$$\frac{1}{\tau_{eff}} = \frac{1}{\tau_{bulk}} + \frac{2S_{eff}}{W} \quad (6.4)$$

Ideally, the bulk lifetime ( $\tau_{bulk}$ ) of silicon does not change during deposition of  $SiN_x:H$ , thus the differences in the measured  $\tau_{eff}$  are directly related to variations in surface recombination velocity  $S_{eff}$  [10]. Therefore, the upper limit of effective surface recombination rate is estimated by  $S_{eff} = W/2\tau_{eff}$  [91].

The lowest  $S_{eff}$  calculated in this work is 6.5 cm/s achieved by Si-rich  $SiN_x:H$  with refractive index of  $\sim 3$  and  $Si/N$  of  $\sim 2.25$ . An increased  $\tau_{eff}$  seems to be related to a higher  $Si/N$  and more Si-H bonds according to Figure 6.13. This is in good agreement with the observation of Verlaan et. al, who showed that increasing  $Si/N$  in the film increases the Si-Si bond density and found no Si-Si bonds in N-rich films [23]. Thus, it is assumed that high amount of  $SiH_4$  precursor saturates the silicon dangling bonds at the surface and forms Si-H or Si-Si bonds. Effective carrier lifetime measured at different injection levels ( $\Delta n$ ) in Figures 6.6 and 6.11 show that ( $\tau_{eff}$ ) increases from low injection to intermediate level ( $10^{14}cm^{-3} < \Delta n < 10^{15}cm^{-3}$ ) and peaks at  $\sim 10^{15}cm^{-3}$ . Kerr et al. indicated that the high doping density in silicon can strongly reduce the lifetime at low injection level [11]. While, the reduction of  $\tau_{eff}$  at high injection levels  $\Delta n > 10^{15}cm^{-3}$  can be explained by the intrinsic recombination and typically dominant Auger recombination  $R_{Auger}$  at doping density ( $N_d$  in n-type Si) higher than  $10^{15}cm^{-3}$  [90].

### The influence of the firing (RTA)

The influence of the firing on the film properties is shown in Figure 6.13a by the black squares. The N-H bonds increased after firing for all samples, while it is not observed for the Si-H bonds. The  $SiN_x:H$  layers with high  $Si/N \geq 1$  ( $R \leq 0.5$ ) show decrease of the Si-H bond density after firing. While, the samples with low values of  $Si/N \leq 1$  ( $R \geq 0.5$ ) show the reduction of the Si-N bonds. This shows that depending on the film stoichiometry, there are different changes in the bond densities at high temperature. Thus, on the basis of our observations, reaction (1) and (2) can take place depending on the film composition,



By considering the binding energies of  $E_{N-H} \sim 3.89 \text{ eV}$ ,  $E_{Si-H} \sim 3.17 \text{ eV}$  and  $E_{Si-N} \sim 4.42 \text{ eV}$  [64] [92], reaction (1) is exergonic with negative change in free energy  $\Delta G = -0.72 \text{ eV}$ , while reaction (2) is endergonic with  $\Delta G = +0.53 \text{ eV}$ . The increase in the N-H bonds in N-rich films (reaction (2)) is also reported by Smith et. al. due to post-annealing and the corresponding film densification [87].

The influence of the firing on the effective carrier lifetime has been also shown in Figure 6.13a. No significant change in  $\tau_{eff}$  is found due to the firing, indicating the thermal stability of deposited  $SiN_x : H$  films. However, a slight reduction of  $\tau_{eff}$  after firing is found in samples with low  $Si/N \leq 1$ . This can be attributed to the formation of recombination-active Si dangling bonds after the release of hydrogen from Si-H bonds, which can suppress the charge carrier lifetime.

### Impact of the substrate temperature $T_S$ on the optical and the compositional properties of $SiN_x : H$

Figure 6.13b presents a summary of the influence of the substrate temperature during the deposition on the structural, electrical and optical properties of  $SiN_x : H$ . In contrast with the last set of samples deposited at various  $R$ , the composition of  $SiN_x : H$  films is not strongly affected by the temperature. The refractive index  $n$  and the  $Si/N$  values show slight increases as  $T_S$  rises from  $100 \text{ }^\circ\text{C}$  to  $400 \text{ }^\circ\text{C}$ . A clear difference between the influence of  $R$  with  $T_S$  can be seen in the bond densities of [Si-H] and [N-H] after deposition. While these bonds changed inversely by increasing  $R$ , they both decrease with higher  $T_S$ . A parallel reduction of the Si-H and the N-H bond densities reveal a total reduction of the hydrogen concentration in the film. Moreover, there is a slight shift in the peak position of the Si-H due to various  $T_S$  illustrated in Figure 6.10a. This implies that the film composition of  $SiN_x : H$  and so the back bonding of the Si-H are not strongly influenced by the substrate temperature.

The growth rate of  $SiN_x : H$  films decreased with rising  $T_S$  which is previously reported by Smith et al. [87]. This is due to the fact that a film densification occurs at higher deposition temperatures, resulting in higher mass density. The increase in Si-N bonds at higher  $T_S$  confirms the higher film density. They reported that the film densification at higher substrate temperatures can lead to a tensile film stress. The stress is found in films grew at  $T_S > 200 \text{ }^\circ\text{C}$  due to the condensation zone below the surface of  $SiN_x : H$  [87]. The decrease of the optical band gap due to increasing  $T_S$  can be explained by the shift of N-bonding from N-H towards Si-N bonds and the increase of the  $Si/N$  ratio. Moreover, the high hydrogen concentration in low-temperature samples passivates most Si or N dangling bonds and reduce the gap states, thereby the band gap increases [64].



**The impact of the substrate temperature  $T_S$  on the passivation quality of  $SiN_x : H$** 

The effective carrier lifetime  $\tau_{eff}$  is measured after the deposition of  $SiN_x : H$  at various  $T_S$  shown by hollow squares in Figure 6.13b. An improvement in  $\tau_{eff}$  at higher substrate temperature can be caused by the increase in the film density and the  $Si/N$  ratio. The increase of the Si-H bonds does not result in higher lifetimes as it is for the other set of samples. It is speculated that the large network disorder due to the high growth rate at low temperatures suppresses the passivation quality of  $SiN_x : H$  films.

**The influence of the firing (RTA)**

The results after firing revealed a slight decrease in N-H and increase in Si-N in low-temperature ( $T_S$ ) films (Figure 6.13b). Post-annealing continues the densification of the films that started during deposition. Therefore, the low-density films are likely to be more affected by the firing. The densification is accompanied by hydrogen loss, which is studied by effusion mass spectroscopy and will be discussed in next section. The increase of effective lifetime in low  $T_S$  can be due to the improvement in film density and the release of hydrogen, which further passivate the defects. However, even after firing  $\tau_{eff}$  is larger in samples deposited at higher substrate temperature. It can be concluded, that deposition of  $SiN_x : H$  at temperature higher than 300 °C is essential for achieving a good surface passivation.

## II Study of the hydrogen transport mechanisms in various $\text{SiN}_x : \text{H}$ layers

In order to study the release of hydrogen from  $\text{SiN}_x : \text{H}$  layers during the contact firing step, hydrogen effusion profiles of various  $\text{SiN}_x : \text{H}$  layers are measured and presented in Figure 6.7 and 6.12. This step is essential for the front-side metallization of silicon solar cells and is typically done at  $\sim 800^\circ\text{C}$ . At such high temperature, most of the hydrogen effuses into air, but a part of this hydrogen diffuses into the silicon surface or the bulk which is known to passivate the crystallographic defects and accelerate the recovery in case of carrier-induced defects like boron-oxygen (BO) complexes [20] [52] [53]. As it is shown by Wieringen et al. [12] and Sheoran et al. [13], the hydrogenation in crystalline silicon (c-Si) at high temperature is not diffusion limited, it can be assumed that effusion in the ambient and diffusion of hydrogen in the bulk are proportional. Thus, more hydrogen effusion might indicate that potentially more hydrogen diffusion into the underlying Si substrate.

### The impact of gas flow ratio $R$ on hydrogen effusion mechanism

In the last section, it is shown that the gas flow ratio strongly affects the film stoichiometry and changes the  $\text{Si}/\text{N}$  ratio in the film.

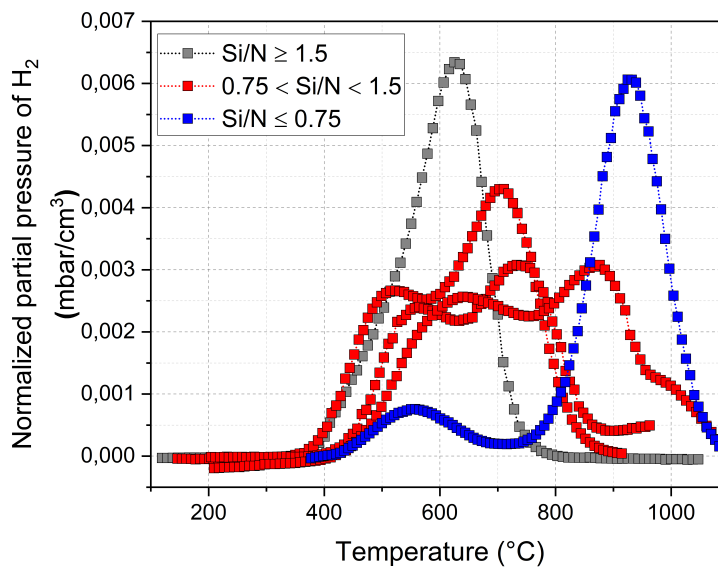


Figure 6.14: Three mechanisms of hydrogen effusion are observed depending on their film stoichiometry related to  $\text{Si}/\text{N}$  ratio.

Effusion measurements are carried out for a set of samples deposited at various  $R$ . From the results, three different mechanisms of hydrogen release related to the film structure are proposed and discussed in the following; (1) an early release of hydrogen at low temperatures in samples with high amount of Si ( $\text{Si}/\text{N} \geq 1.5$ ), (2) layers with two pronounced hydrogen effusion peaks ( $0.75 < \text{Si}/\text{N} < 1.5$ ) and (3) release of hydrogen at high temperatures from films with high N content ( $\text{Si}/\text{N} \leq 0.75$ ) shown in Figure 6.14. An overview of these three possible

mechanisms of hydrogen effusion from  $SiN_x : H$  layers with the probable reactions at different temperatures is shown in Table 6.6 and will be discussed in the following.

|                     | $T < 700^\circ\text{C} (LT_A)$  | $T > 700^\circ\text{C} (HT_A)$                           |
|---------------------|---|--|
| $Si/N \geq 1.5$     | <ul style="list-style-type: none"> <li>• surface desorption of <math>H_2</math></li> <li>• <math>2[Si-H] \xrightarrow{\text{heat}} [Si-Si] + H_2</math></li> <li>• <math>2[Si-H] + 2N^* \xrightarrow{\text{heat}} 2[Si-N] + H_2</math></li> </ul> | no reaction or desorption                                |
| $0.75 < Si/N < 1.5$ | <ul style="list-style-type: none"> <li>• surface desorption of <math>H_2</math></li> <li>• <math>2[Si-H] \xrightarrow{\text{heat}} [Si-Si] + H_2</math></li> <li>• <math>2[Si-H] + 2N^* \xrightarrow{\text{heat}} 2[Si-N] + H_2</math></li> </ul> | $2[N-H] + 2Si^* \xrightarrow{\text{heat}} 2[Si-N] + H_2$ |
| $Si/N \leq 0.75$    | <ul style="list-style-type: none"> <li>• surface desorption of <math>H_2</math></li> </ul>  | $2[N-H] + 2Si^* \xrightarrow{\text{heat}} 2[Si-N] + H_2$ |

Table 6.6: Three different mechanisms of hydrogen release related to the film structure of  $SiN_x : H$  are introduced. The possible reactions for the first ( $LT_A$ ) and second ( $HT_A$ ) peaks of effusion are proposed.

1. The first mechanism is observed for films with a high  $Si/N \geq 1.5$  ratio (R0.1), showing a fast release of hydrogen at low temperatures below  $800^\circ\text{C}$  and a main peak ( $LT_A$  peak) located at  $\sim 600^\circ\text{C}$ . In this specific sample almost no N-H bond is observed, but a high Si-H peak, meaning hydrogen is mostly bonded to Si than N atoms. As the binding energy of Si-H bonds of  $3.17\text{ eV}$  is lower than N-H bonds of  $3.89\text{ eV}$ , hydrogen effusion is facilitated for this composition. Furthermore, the low bond density of Si-N in this film indicates a relative low density, which improves the hydrogen mobility in the film. To compare the industrial firing process with the hydrogen effusion measurement, the hydrogen released below the firing temperature ( $\sim 800^\circ\text{C}$ ) must be taken into account (See section 5.3). Therefore, films with such effusion mechanism such as the sample R0.1 will be a good source of hydrogen during the firing. Although no significant increase in the effective charge carrier lifetime of this film is observed after the firing, as hydrogen is known to be responsible for effective passivation of defects. The initial  $\tau_{eff}$  of  $\sim 2\text{ ms}$  after deposition is the highest  $\tau_{eff}$  value among all samples in this work.
2. The second hydrogen effusion regime is observed in the films with  $0.75 < Si/N < 1.5$  (in samples: R0.3, R0.5, R0.7), resulting in an effusion profile with two peaks at low ( $LT_A \sim 500 - 600^\circ\text{C}$ ) and high temperatures ( $HT_A \sim 700 - 800^\circ\text{C}$ ). Beyer et al. proposed two effusion processes for  $a-Si_x : H$  films, (i) the surface desorption of molecular  $H_2$  at low temperatures and (ii) the diffusion of atomic hydrogen from breaking Si-H bonds at higher temperatures [93]. In the case of the  $SiN_x : H$  layers, the additional N-H bonds affect the mechanism of hydrogen effusion, this explains the presence of an extra peak for  $SiN_x : H$  layers at higher temperatures [58]. As the  $Si/N$  ratio decreases, both peaks

shift to higher temperatures. This can be either related to the increase of the N-H bonds and the decrease of the Si-H bonds or the enhancement of the film density, which delays the effusion of hydrogen due to the diffusion.

3. A further increase of the N content ( $Si/N \leq 0.75$ ) expose a third hydrogen effusion mechanism, where most of the hydrogen effuses at relatively high temperatures. Comparing to the large  $HT_A$  peak observed for this film, only a small amount of hydrogen seems to effuse at the low temperatures. Regarding the absorption spectra of this layer, hydrogen is bonded mainly to N and no Si-H peak is found. The peak of hydrogen effusion appeared at a higher temperature than the usually applied firing temperature, so it is expected that the least amount of hydrogen will be released from this film during the firing.

### The impact of the substrate temperature $T_S$ on the hydrogen effusion mechanisms

The effusion profile of hydrogen released from the  $SiN_x : H$  layers deposited with different substrate temperatures are shown in Figure 6.12. Since the gas flow ratio of  $R0.5$  is used for the deposition of these layers with relatively constant  $N/Si$  values ranged between 0.67-1, this set of samples can be assigned to the second effusion mechanism group with two distinct peaks. However, the position and the height of the two peaks at low ( $LT_A$ ) and high ( $HT_A$ ) annealing temperatures depend on the substrate temperature ( $T_S$ ). The Figures 6.15a and 6.15b display the change of the peak height and the peak position of hydrogen effusion as a function of the substrate temperature ( $T_S$ ) during deposition. The peak height of the  $LT_A$  decreases with increasing substrate temperatures. Beyer et al. reported that high  $LT_A$  peak correlates with a void-rich film structure, which confirms the observation in this work, that low temperature  $SiN_x : H$  deposition results in low-density films [58]. In contrast, the  $HT_A$  peak increased slightly with rise of the substrate temperature. This can be attributed to the further film densification during annealing which limit the free hydrogen molecules to diffuse.

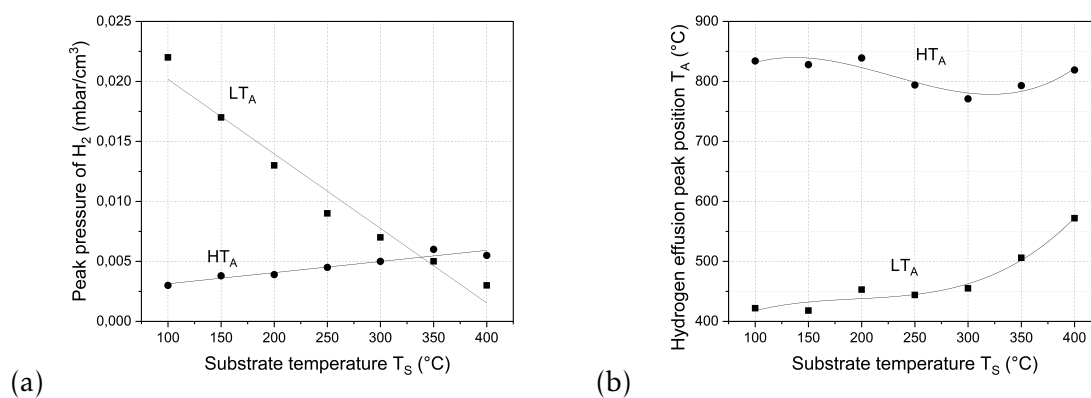


Figure 6.15: a) The height and b) position of two hydrogen effusion peaks ( $LT_A$  and  $HT_A$ ) as a function of substrate temperature used during film deposition of  $SiN_x : H$ . Lines are guide for the eyes.

The shift of the peak position of  $LT_A$  in Figure 6.15b towards higher  $T_A$  values is observed

with increasing  $T_S$ , which can be due to the increased film density. No trend is found for the peak position of the  $HT_A$  regarding different  $T_S$ .

Moreover, total  $\text{H}_2$  concentration diffusing out of the films up to  $T_A \sim 1100$  °C are measured from the effusion spectra. The values are calculated using equation 5.3 and plotted in Figure 6.16. A correlation is found between the concentration of the released hydrogen and the substrate temperature during the deposition, indicating more hydrogen diffuse out of the porous films deposited at the lower  $T_S$ . In comparison with the set of samples deposited with various  $R$  and constant  $T_S$  of 400 °C, the amount of hydrogen released from the films shows almost no change. This implies that the significant effect of the substrate temperature during deposition on the total hydrogen concentration in the films.

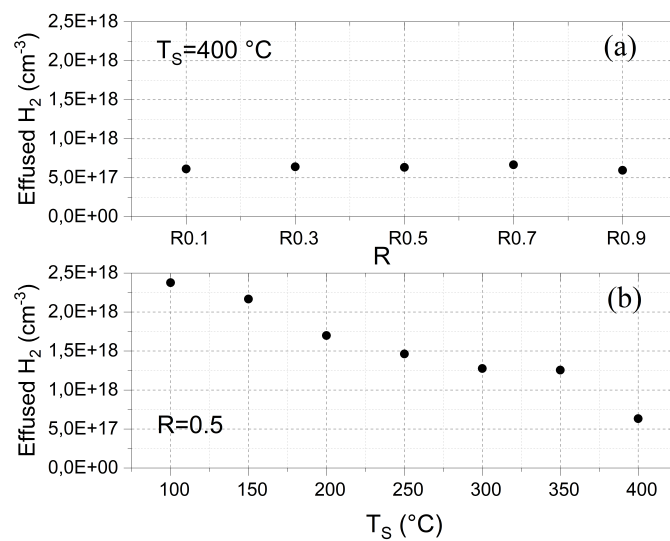


Figure 6.16: Total amount of hydrogen ( $N_{\text{H}_2}$ ) diffused out of the  $\text{SiN}_x : \text{H}$  layers deposited at a) various gas flow ratios ( $R$ ) and b) various substrate temperatures ( $T_S$ ).

### III Three major types of $\text{SiN}_x : \text{H}$ layers based on the film structure and compositional analysis

Based on the results discussed so far, it is suggested to separate the film properties of PECVD-deposited  $\text{SiN}_x : \text{H}$  layers in three major groups depending on the  $\text{Si}/\text{N}$  ratio with different hydrogen effusion mechanisms.

In Figure 6.17a, the calculated  $\text{Si}/\text{N}$  of all deposited films during DoE analysis are shown as a function of the gas flow ratio  $R$ . It shows that even though all deposition parameters change,

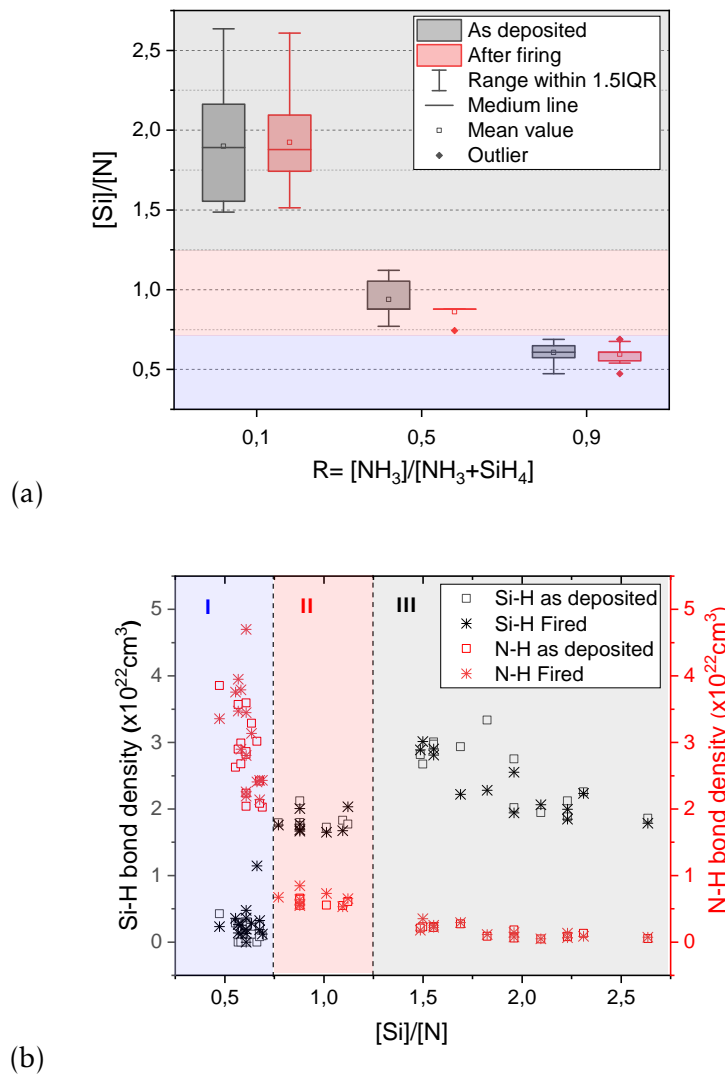


Figure 6.17: The film properties of PECVD-deposited  $\text{SiN}_x : \text{H}$  are categorised into three main groups depending on the  $\text{Si}/\text{N}$  ratio with different H-effusion mechanisms. These three groups are highlighted by different colours. The dependence of the  $\text{Si}/\text{N}$  values on the gas flow ratio  $R$  is shown in a), and the change in hydrogen bond density of the Si-H and N-H bonds as a function of the  $\text{Si}/\text{N}$  values is plotted in b).

the film composition depends strongly on the ratio of the plasma precursor gases. The three suggested ranges of  $\text{Si}/\text{N}$  are highlighted in gray, pink and blue colors. The boxes present the standard deviation from the mean values of  $\text{Si}/\text{N}$ . The gray boxes present the result before

the firing and the red boxes after the firing. A smaller standard deviations from the mean value are obtained for the samples deposited at higher  $R$  which can be explained by the low film density of Si-rich films with larger network disorders.

After the firing, the increase of the film density reduces the standard deviations, however, the mean values remained almost unchanged. A similar color code is used in Figure 6.17b, where the relation of the Si-H and the N-H bond densities with the  $Si/N$  values is plotted. The squares and stars represent the bond densities as-deposited and after the firing, respectively. Red and black colors are representatives for the N-H and the Si-H bonds in the layers. The hydrogen bond densities in the films vary with the change of  $Si/N$  values. Based on these findings, the three types of the  $SiN_x : H$  layers are identified with the following main properties.

In the  $SiN_x : H$  films of group I with low  $Si/N$  value, a high intensity of the Si-H bonds is observed with almost no peak of the N-H bond. While, an opposite trend is observed for the layers of group II which consist of both the Si-H and the N-H bonds with clear dominant Si-H bonds. In  $SiN_x : H$  films of group III, the Si-H bonds increase further and mostly no or poor intensity of the  $N - H$  bonds is observed. After the firing, the trend remains similar to those after deposition. Moreover, the three hydrogen effusion mechanisms discussed already in the last section correspond to these three domains of  $Si/N$  values (see Table 6.6).

In conclusion,  $SiN_x : H$  layers can be divided into the following three groups depending on the  $Si/N$  values,

- I N-rich  $SiN_x : H$  with  $Si/N \leq 0.75$  (near the stoichiometric  $Si_3N_4$ ),
- II medium  $SiN_x : H$  with  $0.75 < Si/N < 1.5$  and
- III Si-rich  $SiN_x : H$  with  $Si/N \geq 1.5$ .

#### The atomic concentrations of N and Si in the three groups of $SiN_x : H$

For further evaluation of these three groups of  $SiN_x : H$  films, the concentration of  $N 1s$  and  $Si 2p$  orbitals are estimated by X-ray photo-electron spectroscopy (XPS) in randomly selected samples from all group. In Figure 6.18, the  $Si/N$  ratio obtained from XPS analysis is plotted in comparison with the  $Si/N$  values calculated from Dauwe model [24] (see equation 6.2) using the linear refractive index of the nitride films.

The linear fit shows 94 % agreement between the two values obtained from XPS analysis and the calculation model. In the chemical formula of  $SiN_x : H$ , the  $x$  value is the ratio of  $N/Si$ , which is, for example, equal to  $4/3 \sim 1.33$  for the stoichiometric  $Si_3N_4$ . In addition to the calculated  $Si/N$  ratio from the Dauwe model and the  $Si/N$  values from the XPS analysis, the  $x$  values are plotted with squares in Figure 6.18 as an indication for the film stoichiometry. The calculation of  $x$  values are based on the data obtained from the XPS analysis. A similar color code is used for the different  $SiN_x : H$  groups to facilitate the comparison with the last diagrams. The  $x$  values vary from 1 to 1.07 for the N-rich layers and decrease to about 0.9 in the medium  $SiN_x : H$  layers. The Si-rich layers show lower  $x$  values ranging from 0.3 to 0.55 in agreement with the different refractive indices.

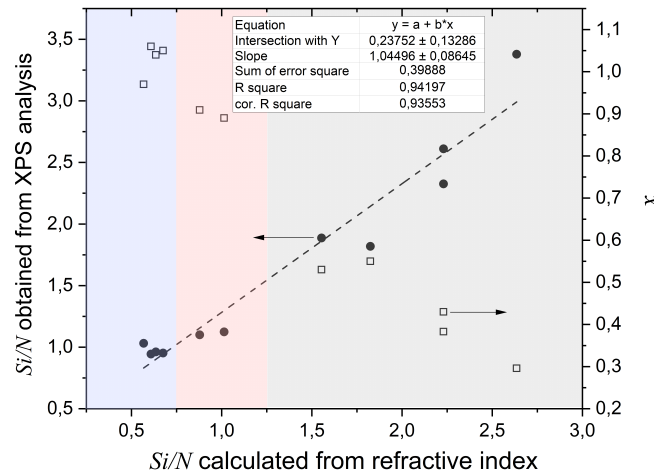


Figure 6.18: Comparison the  $Si/N$  values determined by X-ray photoelectron spectroscopy with Dauwe model [24] using the refractive index of the  $SiN_x : H$  films (equation 6.2).

**The field-effect passivation of three  $SiN_x : H$  groups**

Capacitance-voltage characteristic is used to investigate the effect of film composition on the dielectric properties of the three  $SiN_x : H$  groups. It is known that the  $SiN_x : H$  layers build positive fixed charges close to the  $SiN_x : H/Si$  interface which repel the minority charge carriers in n-type silicon from the surface, thus reducing the surface recombination rate [43] [94]. This is known as field-effect passivation.

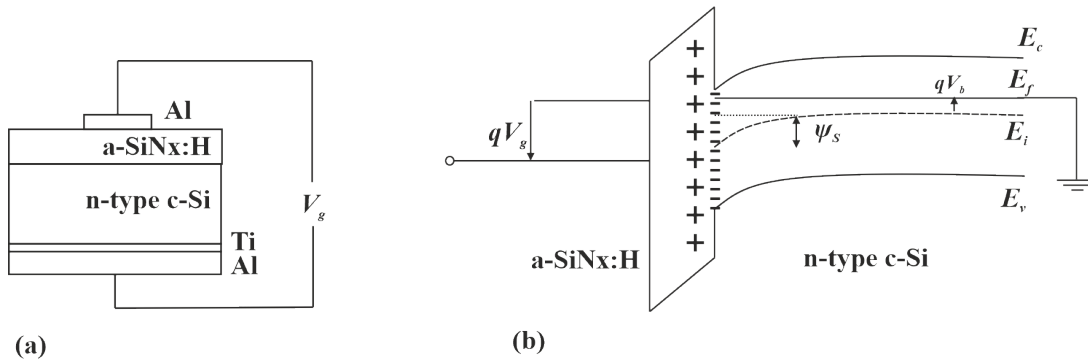


Figure 6.19: a) schematic of MIS device ( $Al/SiN_x : H/c - Si$ ) prepared for C-V characteristics and b) the band diagram of MIS structure when a voltage ( $V_g$ ) is applied.

Metal-insulator-semiconductor (MIS) devices are fabricated for capacitance measurement using  $SiN_x : H$  as insulator.  $SiN_x : H$  layers with different  $Si/N$  ratios from N-rich (group I) to Si-rich (group III) are deposited on one side of n-type FZ-Si wafers. With the use of a shadow mask with hole areas of  $0.04 \text{ mm}^2$ , a layer of Al is sputtered on top of the  $SiN_x : H$  layers forming the gate electrodes. On the backside of the Si wafer, a stack of Ti/Al with thicknesses of  $50/500 \text{ nm}$  provide the Ohmic contact. The devices are annealed at  $300 \text{ }^\circ\text{C}$  for 5 min and then fired with a fs laser from the backside.



A schematic of the MIS device and the energy band diagram with applied voltage  $V_g$  are presented in Figures 6.19a and 6.19b, respectively. The electrical properties of Al and the Si wafers used for the latter calculations are presented in Table 6.7.

| Property                                   | Value                |
|--|----------------------|
| silicon band gap (eV)                      | 1.12                 |
| doping concentration $N_D(cm^{-3})$        | $7.5 \times 10^{14}$ |
| electron affinity of c-Si $\chi_{Si}$ (eV) | 4.05                 |
| work function of Al $\Phi_{Al}$ (eV)       | 4.10                 |

Table 6.7: The properties of Al and c-Si wafers applied for the calculation of positive fixed charges in  $SiN_x:H$  films.

C-V curves measured for three types of  $SiN_x:H$  layers at the frequency of  $\nu = 1$  MHz in dark

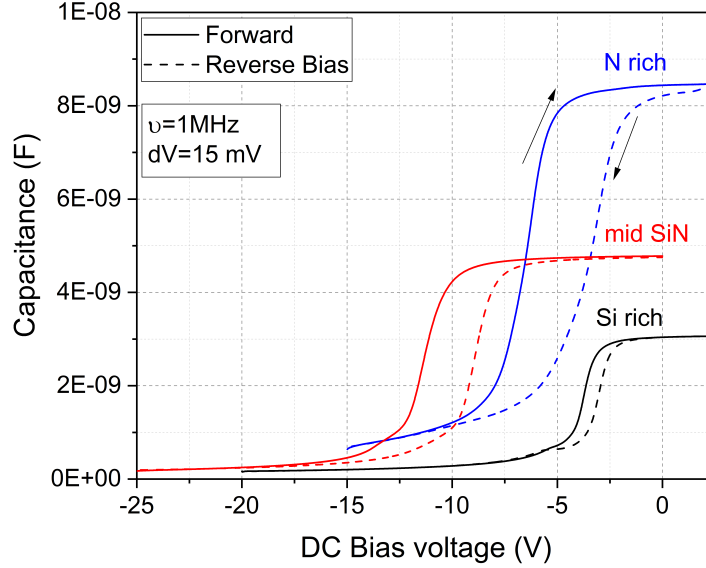


Figure 6.20: C-V characteristics for the three  $SiN_x:H$  groups measured in forward-bias sweep (full lines) and reverse-bias sweep (dashed lines). The measurement frequency is 1 MHz and the voltage sweep interval is 15 mV.

are shown in Figure 6.20. The voltage is swept from -25 to 5 V (forward bias) and back from 5 to -25 V (reverse bias) during the measurements. The shift of the curves in negative voltages imply an increase of positive fixed charges in the film [95]. The relative permittivity of  $SiN_x:H$  layers  $\epsilon_{SiN}$  is given by [96],

$$\epsilon_{SiN} = \frac{C_{max}d_{SiN}}{A_g} \quad (6.5)$$

with the film thickness  $d_{SiN}$  and the gate area  $A_g$ . The flat band capacitance  $C_{FB}$  can be determined from,

$$C_{FB} = \frac{\epsilon_{SiN}}{d_{SiN} + \epsilon_{SiN} \left( \frac{kT}{\epsilon_{SiN} N_D q^2} \right)^{1/2}}. \quad (6.6)$$

Therefore, the corresponding flat band voltage  $V_{FB}$  and the positive fixed charges  $Q_{fix}$  are obtained from the following equation [96],

$$Q_{fix} = C_{SiN}(\Phi_{MS} - V_{FB}) = C_{SiN} \left( \Phi_{Al} - \chi_{Si} - \frac{E_g}{2q} + \frac{kT}{q} \ln \left( \frac{N_D}{n_i} \right) - V_{FB} \right) \quad (6.7)$$

with the work function difference  $\Phi_{MS}$  between metal and silicon, the band gap  $E_g$  of silicon and the doping concentration  $N_D$ . The results are listed in Table 6.7. The hysteresis ( $\Delta V =$

| Sample name        | Si-rich               | mid SiN               | N-rich                |
|--------------------|-----------------------|-----------------------|-----------------------|
| $C_{SiN}(F)$       | $3.05 \times 10^{-9}$ | $4.78 \times 10^{-9}$ | $8.4 \times 10^{-9}$  |
| $C_{FB}(F)$        | $2.3 \times 10^{-9}$  | $2.9 \times 10^{-9}$  | $3.9 \times 10^{-9}$  |
| $V_{FB+}(V)$       | -3.47                 | -11.16                | -6.8                  |
| $V_{FB-}(V)$       | -2.78                 | -9.24                 | -3.8                  |
| $\Delta V(V)$      | 0.69                  | 1.92                  | 3                     |
| $Q_{fix}(cm^{-2})$ | $7.03 \times 10^{11}$ | $1.1 \times 10^{12}$  | $1.95 \times 10^{12}$ |

Table 6.8: A list of quantities measured by a high frequency C-V measurements of three different type of  $a - SiN_x : H$  films.

$V_{FB+} - V_{FB-}$ ) indicates the change of the flat band voltage  $V_{FB}$  which depends on the charge state of the traps at the interface or in the bulk. The hysteresis of the investigated samples grow as the  $Si/N$  ratio decreases from the Si-rich to the N-rich film. It is already known that the Si dangling bonds are the dominant deep trap states which are responsible for the large hysteresis [97] and are located in the middle of the band gap [64]. The Si dangling bonds appear as the so-called  $\cdot Si \equiv Si_{3-n}N_n$  configuration with  $n = 1, 2$  and  $3$ , depending on their back-bonding to Si or N [94].

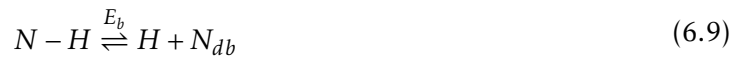
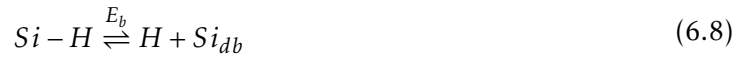
For example, in the Si-rich films, the  $\cdot Si \equiv Si_3$  configuration ( $n=0$ ) appears more likely, while in N-rich films the configuration can be  $\cdot Si \equiv N_3$  ( $n=3$ ) which is called K-centers [94]. In this work, the highest concentration of positive fixed charges  $Q_f$  is obtained for the N-rich film with a capacity of  $\sim 8.5 nF$ . The hysteresis is also larger in N-rich film, thus more trap states are expected in this film.

### Hydrogen effusion model for the three groups of $SiN_x : H$ layers

Based on the properties of the introduced three groups of  $SiN_x : H$  layers and the various mechanisms of the hydrogen effusion that are discussed in the previous section (section II), a schematic model of the diffusion/effusion from  $SiN_x : H$  during the firing process will be proposed in this section.

In general, the effusion of hydrogen out of the  $SiN_x : H$  layer consists of two subsequent processes. **First**, the dissociation of hydrogen from its bond which leads to free hydrogen and the generation of the dangling bonds. **Second**, the diffusion of the free hydrogen in the film towards the surface in the form of a molecule or an atom.

Regarding the first process, reactions 6.8 and 6.9 demonstrate the dissociation of the Si-H and the N-H bonds with the binding energy  $E_b$  in the  $SiN_x : H$  film. The products of the reaction are free hydrogen atoms and dangling bonds such as  $Si_{db}$  or  $N_{db}$ .



Since the binding energy of the hydrogen bonds in  $SiN_x : H$  are above 2 eV, thermal energy with temperature of approximately 800 °C ( $\sim 0.1$  eV) cannot break the bonds. Therefore, the energy which is essential for the bond dissociation must be provided by other possible exothermic reactions, e.g.  $H + H \rightarrow H_2$  ( $\Delta G = -4.5$  eV) or  $Si-H + Si-H \rightarrow Si-Si + H_2$  ( $\Delta G = -0.64$  eV [64]).

In the second process, the diffusion of hydrogen can be limited by being trapped in the defects or the non-passivated dangling bonds. The increase of trap density in the film ( $C_T$ ) suppress the effective diffusivity ( $D$ ) of hydrogen as described [28] [98] in the equation 6.10.

$$D = \frac{\nu_0}{4\pi C_T \sigma_T} \exp\left(\frac{-\Delta E}{kT}\right) \quad (6.10)$$

with the attempt frequency  $\nu_0$ , the cross section of the traps  $\sigma_T$  and the activation energy  $\Delta E$  which is the sum of binding energies and migration energy of hydrogen ( $\Delta E = E_b + E_m$ ) [98].

Based on the two processes and the influence of the film structure and the defect density on the diffusion/effusion of hydrogen, a schematic model of hydrogen transport in the three  $SiN_x : H$  groups is presented in Figure 6.21, which will be evaluated in the following.

Before that, as a reminder, the properties of the three classes of  $SiN_x : H$  films are again briefly summarized.

(1) In the Si-rich layer that is illustrated in gray color in Figure 6.21 with high  $Si/N \geq 1.5$ , hydrogen mainly bonds with Si to Si-H. The film growth is relatively high ( $\sim 50$  nm/min) and the film shows a porous structure. The effusion of hydrogen in this layer occurred at temperatures below 800 °C and the layer showed the superior passivation quality.

(2) Medium  $SiN_x : H$  layers in pink, with higher N ratio ( $0.75 \leq Si/N \leq 1.5$ ), consists of both the Si-H and the N-H bonds and are denser. The effusion of hydrogen shows two peaks at the  $LT_A$  and the  $HT_A$  as a sign of different hydrogen bondings. The passivation quality and the

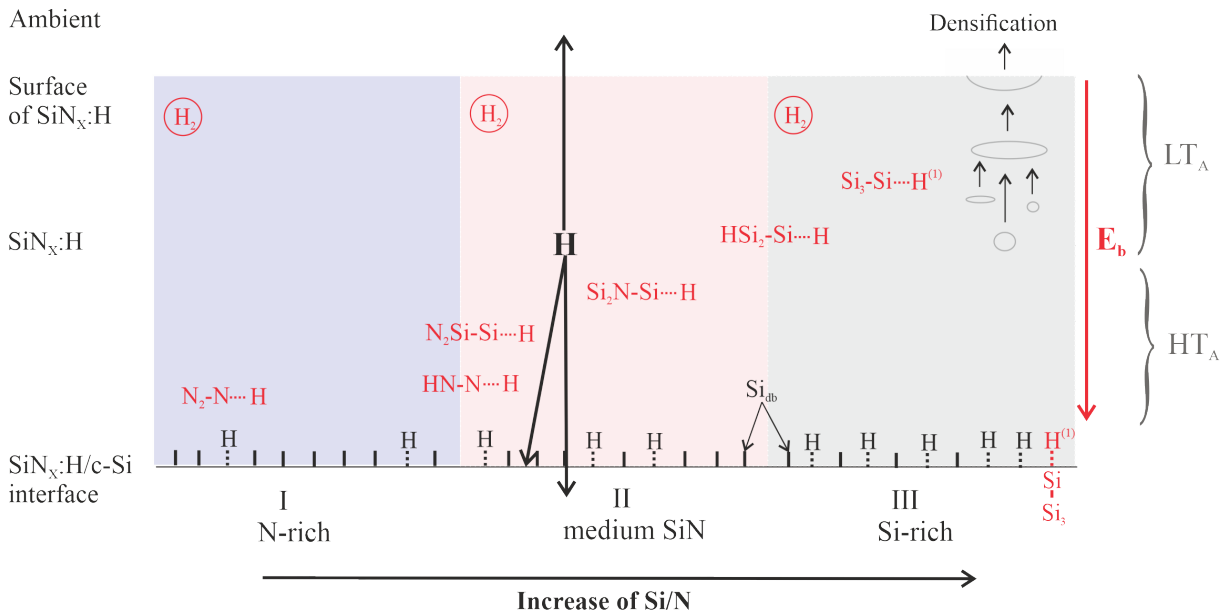


Figure 6.21: Schematic model of the hydrogen transport mechanisms during annealing for N-rich, medium SiN and Si-rich films, with various compositions ( $\text{Si}/\text{N}$  ratios). Reduction of  $\text{Si}/\text{N}$  increases the probability of hydrogen bonds with higher binding energies ( $E_b$ ) which postpone the effusion/diffusion of hydrogen to higher temperatures (larger  $HT_A$  peak in effusion spectra). An example of densification due to annealing is illustrated in low density Si-rich layer.

<sup>(1)</sup>  $\text{Si}_3\text{-Si-H}$  configuration can be found at the interface of  $c\text{-Si}/\text{SiN}_x : \text{H}$ .

film growth rate decreased in comparison to the Si-rich films.

(3) N-rich layers in purple with low  $\text{Si}/\text{N}$  ratios below 0.75 have dominant N-H bindings. The layer growth rate is further reduced, resulting in a higher layer density. Therefore, the peak of hydrogen effusion is at the higher temperatures above 800 °C. N-rich films show poor passivation quality possibly due to defective interfaces at the  $\text{Si}/\text{SiN}_x : \text{H}$  interface.

Back to Figure 6.21, the bottom line shows the interface of the  $c\text{-Si}$  wafer and the  $\text{SiN}_x : \text{H}$  layer. The Si dangling bonds ( $\text{Si}_{db}$ ) are illustrated by short vertical lines at the interface, while those passivated by hydrogen are indicated by dashed lines bonded with hydrogen. Different Si-H and N-H bonds are shown in red, sorted from low binding energy at the top to high binding energy at the bottom of the figure (see schematic scale of  $E_b$  on the right side). The differences in the binding energies are a result of the various back-bondings as described by Giorgis et al. [29]. A back bond refers to the adjacent atoms bonded to a target bond, for example here to the Si-H bond. A larger N contribution in the backbonding increases the binding energy of the Si-H bonds due to the higher electronegativity of N, leading to a shift of the Si-H peak position to higher wavenumbers (See Figure 6.5a).

The positions of the hydrogen effusion peaks depend strongly on the bond configuration and the film structure. A peak at low temperature ( $LT_A$ ) originates from effused molecular  $\text{H}_2$  and a structure with a high Si-H density as the Si-H bonding energy is relatively low, while the high temperatures ( $HT_A$ ) peak is associated with the atomic hydrogen with longer diffusion length (due to the high probability of trapping by the defects) and hydrogen bonds with higher binding energies such as the N-H.

The diffusion of hydrogen can be (i) toward the surface, causing the effusion of hydrogen into the ambient, or/and (ii) toward the interface of  $c - Si/SiN_x : H$  and (iii) into the bulk of Si, as shown symbolically by the three black arrows. In each of these three paths, the trapping and de-trapping of hydrogen can be encountered within the film and at the interfaces.

Based on the proposed model, the mechanisms of hydrogen diffusion in different composition of  $SiN_x : H$  films in high temperature processes such as the firing are described in the following:

1. In **N-rich** SiN films, the hydrogen diffusion and effusion is limited by the high concentration of dangling bonds and defects due to the low passivation quality (high trap density) and the presence of N-H as dominant bonds with relative high binding energy ( $E_{N-H} \sim 3.89 \text{ eV}$ ). Therefore, higher energy is essential for hydrogen effusion and the peak appears at rather higher temperatures ( $HT_A \geq 700 \text{ }^\circ\text{C}$ ). N-rich  $SiN_x : H$  films can work as a diffusion barrier for hydrogen during the firing.
2. In **mid SiN** layers, the concentration of hydrogen bonded to Si increases with comparison to N-rich film and the Si-H bond density dominates. The presence of both the Si-H and the N-H bonds leads to an effusion peak at low and high temperature, however, the  $LT_A$  peak is higher as long as the Si-H bonds dominate. The lower binding energy of Si-H and the higher porosity in the film facilitate the diffusion of hydrogen and shift the effusion peak to lower temperatures. The reduction of N backbonding to Si-H or N-H also affects the binding energies and decrease the effusion temperature.
3. In **Si-rich** SiN films, almost all hydrogen atoms are bonded to Si. The N back bonding of the Si-H bonds further decreases which results in lower binding energy below  $3 \text{ eV}$ . The low energy required for bond breaking and the void-rich structure provide rapid diffusion of hydrogen at low temperatures ( $LT_A \leq 700 \text{ }^\circ\text{C}$ ) below the firing. Therefore, this film can serve as a source of hydrogen for further passivation of defects at the interface of  $c - Si/SiN_x : H$  and in the bulk of Si. Furthermore, the formation of Si-Si bonds with the low binding energy of  $2.34 \text{ eV}$  [64] lead to a film densification during annealing ( $Si - H + Si - H \longrightarrow Si - Si + 2H$ ) [80]. This densification can limit the hydrogen effusion at higher temperatures.

## Conclusion

In this chapter, three groups of  $SiN_x : H$  films depending on the  $Si/N$  ratios are classified regarding the systematic analysis of the structural, optical and electrical properties of the films. The stoichiometry of  $SiN_x : H$  films are determined by estimation of  $Si/N$  values which depends strongly on the ratio of gas precursors during deposition.

The results indicate that Si-rich films with high concentration of Si-H bonds are the optimal candidate for surface passivation of Si dangling bonds. Moreover, they show a relatively high growth rate which is economically preferable. However, the low density of the Si-rich films leads to larger out-diffusion of hydrogen during firing. In contrast, films with high N incorporation show a small tendency to release hydrogen below the firing temperature. This

effect is related to the higher binding energy of  $N - H$  and the increase of the trap density. Therefore, it can be postulated that  $SiN_x : H$  layers stack including a N-rich film as cap layer can eliminate hydrogen effusion during the firing and subsequently increase the amount of hydrogen to passivate defects at the Si surface or the bulk.

Moreover, the experiments reveal that the total concentration of hydrogen in the films can be adjusted by the deposition temperature. A lower deposition temperature improves the hydrogen insertion in the films. Although, there is no correlation between an increased total hydrogen content in the film and an improved passivation quality. This is attributed to the reduction of the film density with increasing hydrogen level. This is shown by increase of hydrogen released at the low annealing temperatures in the samples deposited with low deposition temperature.

## 6.2 Examples of using hydrogen effusion measurements for PV applications

In this section, two applications of hydrogen effusion measurements in photovoltaics are discussed. In the first part, a stack of three groups of  $\text{SiN}_x : \text{H}$  layers is investigated to verify whether the stack of N-gradient layers can prevent the effusion of hydrogen into the ambient during the firing process and subsequently increase the diffusion of hydrogen into the underlying Si wafer for passivating the defects [1].

In the second part, the application of the effusion experiments to study the light- and elevated temperature-induced degradation (LeTID) is presented. Different passivation layers are investigated and the results are compared with the standard LeTID test [2]

### 6.2.1 Composition-limited hydrogen effusion of $\text{SiN}_x : \text{H}$ layers stack [1]

In silicon solar cells, hydrogen is known as passivation material to improve the lifetime of minority charge carriers. During the rapid thermal annealing (RTA) process, hydrogen from the  $\text{SiN}_x : \text{H}$  layer deposited on Si wafers can diffuse through the interfaces or into the Si bulk. Regarding the effusion mechanisms of  $\text{SiN}_x : \text{H}$  layers with different compositions discussed in section II, it is assumed that layers stack of three nitride groups with the N-rich film as capping layer can eliminate the effusion of hydrogen into the ambient and simultaneously increase the hydrogen diffusion through the underlying silicon at the firing temperature of  $\sim 800^\circ\text{C}$ .

To investigate this hypothesis, n-type FZ-Si wafers with a resistivity of  $1\text{-}5\ \Omega\cdot\text{cm}$  and  $\langle 100 \rangle$  orientation are used to deposit layers stack of  $\text{SiN}_x : \text{H}$ . A Si-rich layer is first deposited on the top of the Si-wafer, followed by the mid-SiN layer which is ultimately covered by the N-rich layer. A schematic of the stacks can be seen in Figure 6.22. Regarding the different growth rate of the layers, deposition times are varied to obtain identical layer thicknesses. The gas flow ratio of R0.1, R0.5 and R0.9 are used to provide different film compositions.

|         |
|---------|
| N-rich  |
| Si~N    |
| Si-rich |
| c-Si    |
| Si-rich |
| Si~N    |
| N-rich  |

Figure 6.22: a) Schematic of the layer stacks of three classes of silicon nitrides, the Si-rich, the medium (Si~N) and the N-rich SiN layer deposited on both sides of the c-Si wafer.

## I Results

Table 6.9 shows the deposition parameters, the thicknesses of the layers and the deposition rates  $G$ .

| Sample name | $R$         | $d$ (nm) | Deposition time (min) | $G$ (nm/min) |
|-------------|-------------|----------|-----------------------|--------------|
| Si-rich     | 0.1         | 92       | 2                     | 46           |
| mid-SiN     | 0.5         | 89       | 3                     | 29,5         |
| N-rich      | 0.9         | 90       | 4                     | 22,5         |
| Stack       | 0.1/0.5/0.9 | 45/30/22 | 1/1/1                 |              |

Table 6.9: The film thicknesses  $d$ , deposition rate  $G$  and deposition variables, gas flow ratio ( $R$ ) and deposition time, used during deposition of  $SiN_x : H$  layers.

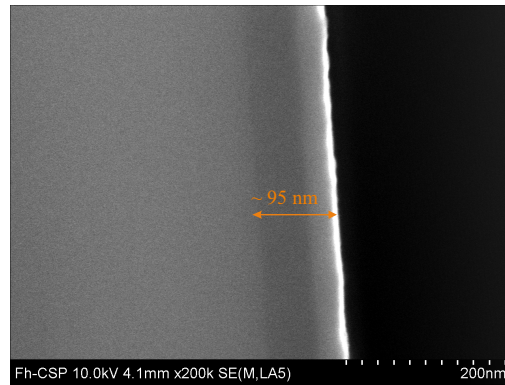


Figure 6.23: Cross sectional SEM image of the layers stack of  $SiN_x : H$  deposited on the silicon wafer.

The thickness of the stacks is measured from the cross sectional SEM image shown in Figure 6.23 (see Table 6.9). The thicknesses of the different layers in the stack are estimated from the growth rates (see Table 6.9), resulting in the Si-rich layer with the thickness of  $\sim 45$  nm, the medium layer with  $\sim 30$  nm and the N-rich layer with  $\sim 22$  nm.

### Hydrogen effusion measurements

The molecular hydrogen effused from the three single layers and the layers stack of  $SiN_x : H$  are shown in Figure 6.24. The values are normalized to the volumes of the films.

The hydrogen effusion mechanisms of three different compositions of the  $SiN_x : H$  layers are previously discussed in detail (in Chapter 6, part II). The Hydrogen effusion diagram of the layers stack consists of two peaks similar to the single layers with an  $LT_A$  peak at  $\sim 587$  and  $HT_A$  peak at  $\sim 858$  °C. However, the overall effusion rate is drastically decreased in the stack. Moreover, the height of the  $LT_A$  peak is higher than the  $HT_A$  peak for stack which can be explained by the deposition of a thicker Si-rich layer. Regarding firing temperature, the percentages of effused hydrogen up to 800 °C is calculated for all samples which are listed in Table 6.10. The results show that the hydrogen effusion from the N-rich  $SiN_x : H$  layer is



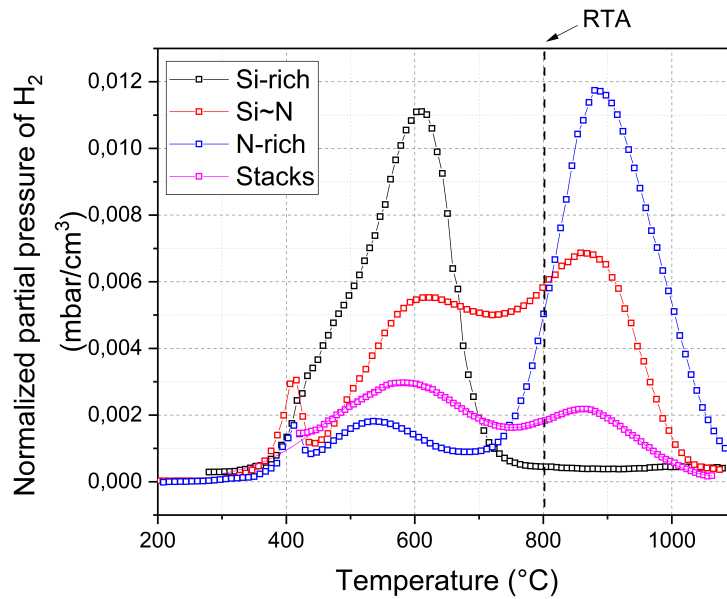


Figure 6.24: Partial pressure of molecular hydrogen effused from different  $SiN_x : H$  layers as well as the layers stack normalized to the film volumes as a function of annealing temperature, the firing temperature of  $\sim 800$  °C is shown by a dashed line.

$\sim 46$  % less than the Si-rich layer. The concentration of hydrogen effused from the layers stack decreases compared to the Si-rich and mid-SiN layer, however, it is  $\sim 15$  % higher than the N-rich layer.

| Sample name | $\frac{\int_{RT}^{800\text{ C}} p_{H_2} dT}{\int_{RT}^{1000\text{ C}} p_{H_2} dT}$ |
|-------------|--|
| Si-rich     | $\sim 94\%$  |
| mid-SiN     | $\sim 82\%$  |
| N-rich      | $\sim 48\%$  |
| Stack       | $\sim 62\%$  |

Table 6.10: fraction of the molecular hydrogen effused at the annealing temperature between the room temperature (RT) and the firing temperature (800 °C) from the different  $SiN_x : H$  layers including the layers stack.

### Hydrogen bond density analysis via FTIR spectroscopy

Figure 6.25 shows the absorption spectra of different layers of  $SiN - x : H$  and the layers stack after the deposition and after the hydrogen effusion measurement. The hydrogen concentration estimated from the FTIR spectroscopy includes only the bonded hydrogen to Si or N atoms, while the effusion mass spectroscopy measures the total Hydrogen content including the atomic or the interstitial hydrogen. Therefore, a combination of both methods gives valuable information about the film composition and the diffusion mechanisms of hydrogen.

The Si-N, the Si-H and the N-H peaks are located at the wavenumbers of  $860\text{ cm}^{-1}$ ,  $2000\text{-}2200\text{ cm}^{-1}$  and  $3350\text{ cm}^{-1}$ , respectively. Similar color codes are used in Figure 6.24 for the

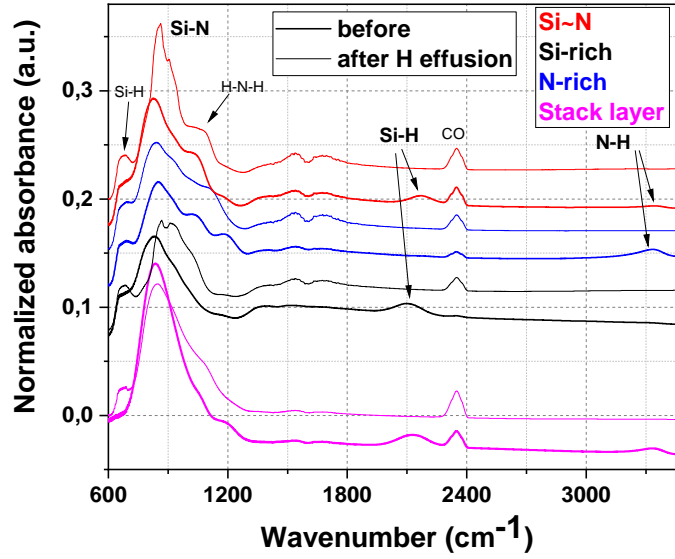


Figure 6.25: Absorption spectra obtained from the FTIR spectroscopy for the silicon wafers deposited with different layers of  $\text{SiN}_x : \text{H}$  and the layers stack after deposition and after the firing.

absorption spectra before and after the firing. Thin lines show the spectra after effusion measurements. The spectra of the mid-SiN layer and the layers stack indicate both the Si-H and the N-H bonds, while the N-rich layer contains only the peak of N-H bond and the Si-rich layer only the peak of Si-H bond. After the effusion experiments, the peaks are disappeared from the spectra for all samples.

### Minority charge carrier lifetime

The effective charge carrier lifetime ( $\tau_{eff}$ ) of the layers stack is measured and compared with different  $\text{SiN}_x : \text{H}$  layers. Figure 6.26a and 6.26b show the effective charge carrier lifetimes  $\tau_{eff}$  before and after the firing, respectively. The stack shows an effective charge carrier lifetime of  $\sim 34 \mu\text{s}$ , which is higher than that of the N-rich layers. However, the Si-rich and the mid-SiN layers both show better passivation quality than the layers stack. Slight changes in  $\tau_{eff}$  are observed after the firing, but no obvious relation to the hydrogen concentration in the films is found.

| $R$     | $\tau_{as\ deposited} (\mu\text{s})$ | $\tau_{Fired} (\mu\text{s})$ |
|---------|--------------------------------------|------------------------------|
| Si-rich | 1965                                 | 1717                         |
| mid-SiN | 523                                  | 370                          |
| N-rich  | 13                                   | 15.3                         |
| stack   | 34                                   | 40                           |

Table 6.11: Effective charge carrier lifetime measured at minority carrier density of  $10^{15} \text{cm}^{-3}$  for Si wafers deposited by different layers  $\text{SiN}_x : \text{H}$  and the layers stack with various gas flow ratios  $R$  a) after deposition and b) after the firing.

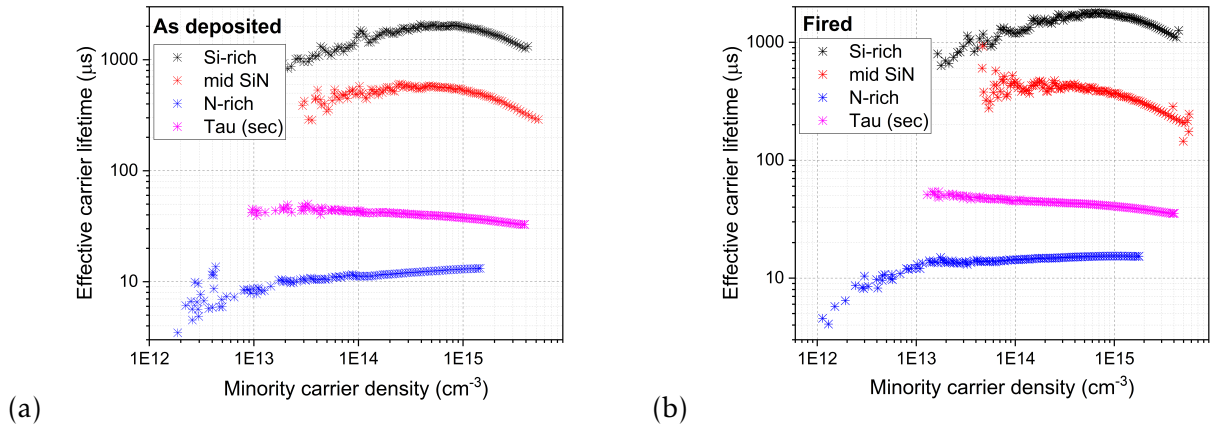


Figure 6.26: Effective charge carrier lifetime of  $SiN_x:H$  layers stack deposited on Si wafers with various gas flow ratios  $R$  a) after deposition deposited and b) after the firing.

## II Discussion

As previously mentioned, the Si-rich layer release more hydrogen during the firing in comparison with the N-rich layer, where the peak of hydrogen effusion appears at higher temperatures than the firing ( $\sim 800$  °C). A layers stack of three groups of  $SiN_x:H$  shows a lower hydrogen effusion ( $\sim 30$  %) than the Si-rich or the mid-SiN layers. This supports the hypothesis that the N-rich layer acts as a diffusion barrier to hydrogen during the firing. The amount of hydrogen calculated from the FTIR spectroscopy is compared with the values which are obtained from the effusion measurements (see Table 6.12). The effused hydrogen from the single layers is higher than the measured hydrogen bonds from the FTIR. The bond densities in the layers stack and the mid-SiN are almost identical after deposition, while the effusion of hydrogen from layers stack is 50 % lower than the mid-SiN layer. This suggests that the amount of hydrogen that is disappeared from the absorption spectrum of the stack after the effusion experiment is not totally effused into the ambient, but also diffuse through the interface or the bulk of the underlying Si wafer which is not traceable by the FTIR.

| Sample name | $\frac{H_{effusion} - H_{FTIR}}{H_{effusion}}$ |
|-------------|--|
| Si-rich     | 0.26   |
| mid-SiN     | 0.34   |
| N-rich      | 0.43   |
| Stack       | -0.77  |

Table 6.12: The relative difference of the hydrogen concentration in the the  $SiN_x:H$  layers and stack calculated from the FTIR spectra and from the hydrogen effusion measurement.

To increase the hydrogen diffusion from  $SiN_x:H$  into the Si wafers below the firing temperature of 800 °C, a thick layer of the Si-rich layer is deposited on the surface of the silicon wafer as a hydrogen source. A higher passivation quality is expected, when more hydrogen can diffuse into the  $Si/SiN_x:H$  interface or the Si bulk due to a higher saturation of

recombination-active defects. Based on this result, the effective charge carrier lifetime of the sample deposited by layers stack of  $SiN_x : H$  increases slightly after the firing, however its value is still smaller than the measured lifetimes of the samples deposited with the Si-rich or the mid-SiN layers. Therefore, the expectation could not be verified experimentally. Nevertheless, the experiments confirmed that the N-gradient layers stack of  $SiN_x : H$  can work as a diffusion barrier for hydrogen during the firing when the N-rich layer is the cap layer.

### 6.2.2 Understanding LeTID in Si wafers using hydrogen effusion measurements<sup>[2]</sup>

A part of hydrogen in hydrogenated films such as  $SiN_x:H$  is released into the silicon bulk during the firing which have been shown to passivate crystallographic defects and accelerate the recovery in case carrier-induced defects like boron-oxygen (BO) [52] [53] [20]. However, recently there is a rising amount of literature that indicates the involvement of this bulk hydrogen is causing a (relatively) recent degradation phenomenon called Light and elevated temperature-induced degradation (LeTID) [99] [100] [101]. This degradation phenomenon has been the focus of multiple research groups worldwide as it causes a significant degradation in all silicon wafer types [102] [103] and particularly in passivated emitter rear contact (PERC) cells [104]. Although the root cause of LeTID is not completely understood, it has been recently reported to increase all pointing towards hydrogen being (at least in part) a defect precursor for LeTID.

The aim of this work is to improve the physical understanding of the LeTID mechanism in regard to the role of hydrogen. Hydrogen effusion measurements are applied for the first-time to study the LeTID effects in silicon wafers deposited with various hydrogenated thin films. This work is performed as a joint project with University of new South Wales (UNSW) and the results are published [2].

## I Experimental

### Sample preparation

Commercial iso-textured 156 mm × 156 mm boron-doped p-type Czochralski-Si (Cz-Si) wafers of resistivity  $\sim 1 \Omega \text{ cm}$  and thickness 180  $\mu\text{m}$ , Multicrystalline silicon (mc-Si) wafers of resistivity  $\sim 1.6 \Omega \text{ cm}$  and thickness 180  $\mu\text{m}$  and double-side polished FZ-Si wafers of resistivity  $\sim 4 \Omega \text{ cm}$  and thickness 285  $\mu\text{m}$  are used. The wafers are cleaned using the standard Radio Corporation of America (RCA) 1 and 2 processes, followed by a short hydrofluoric acid (HF) dip to remove any oxides from the surfaces. All the wafers then underwent a gettering  $POCl_3$  diffusion which resulted in heavy  $n+$  regions. These layers are chemically etched back by a solution of HF and nitric acid. The samples are then passivated to make two sets of minority carrier lifetime test structures.

**For the first set**,  $SiN_x:H$  layers of different thicknesses are as deposited on both the sides by using remote PECVD tool (Roth & Rau MAiA) at 400 °C to create symmetrical lifetime structures. To vary the thickness of  $SiN_x:H$ , the belt speed in the tool is doubled (104 cm/min) to obtain the thinnest layer ( $\sim 50 \text{ nm}$ ). Subsequent depositions are achieved using the same recipe by repeating the process two, three, and four times, respectively, to achieve variable  $SiN_x:H$  thicknesses. The samples are then fired at a set peak temperature of 855 °C (actual sample temperature of  $770 \pm 3 \text{ °C}$ ) at a constant belt speed of 450 cm/min in an industrial belt furnace. On the other hand, the polished FZ-Si samples are fired at a set peak temperature of 935 °C (actual  $770 \pm 2 \text{ °C}$ ). The actual thermal profiles are measured on identical wafers using a Q18 Datapaq thermal profiler. Precise details can be found in an earlier publication [105].

For the second set, the samples are passivated with (1) PECVD based  $SiN_x:H$  with a thickness  $\sim 80$  nm and refractive index  $\sim 2.02$ , (2)  $SiN_x:H$  capped with atomic layer deposition (ALD) based  $AlO_x:H$  with a thickness  $\sim 7$  nm deposited at  $250^\circ C$  and (3)  $AlO_x:H$  capped with  $SiN_x:H$ . The details of the process can be found in [106]. The samples are then fired at a set peak temperature of  $830^\circ C$ . FZ-Si samples are used for FTIR measurements, mc-Si samples for testing LeTID and Cz-Si for both testing the BO regeneration and hydrogen effusion spectroscopy. A schematic of the experimental process flow is shown in Figure 6.27.

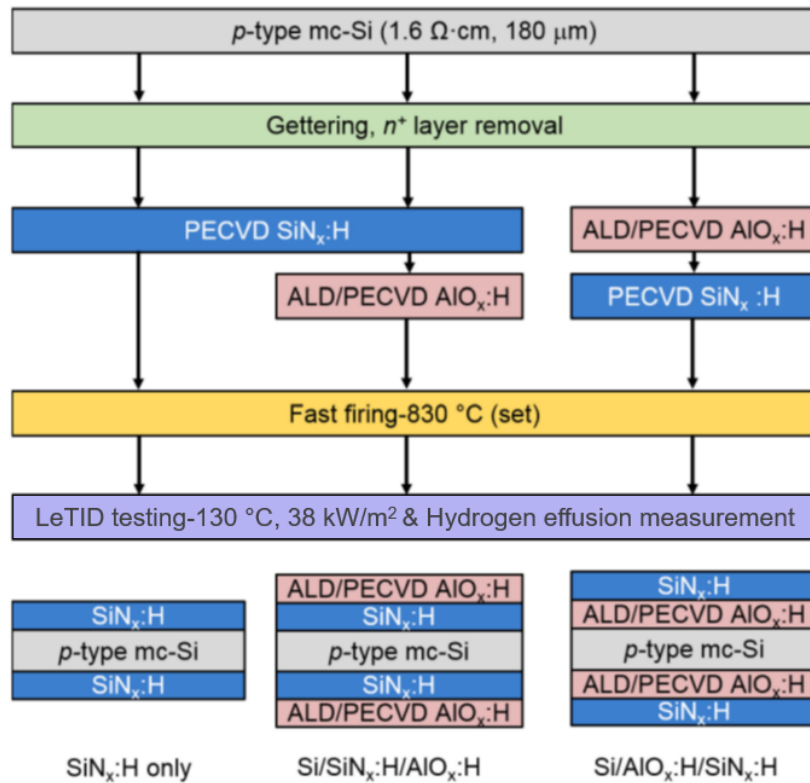


Figure 6.27: The experimental flow chart for sample preparation. [106].

### LeTID testing

The mc-Si samples underwent accelerated LeTID testing using a  $938\text{-nm}$  high-intensity laser illumination of  $26.6 \text{ kW/m}^2$  and  $38 \text{ kW/m}^2$  [107] at  $130^\circ C$  for set one and two, respectively. It is worth noting that the difference in illumination intensities occurred due to an upgrade in the laser system. The progression in effective minority carrier lifetime,  $\tau_{eff}$  is measured using a photoconductance decay lifetime tester from Sinton instruments (WCT-120TS) at room temperature. For comparison between degradation extents, NDD is calculated [108].

$$NDD = \frac{1}{\tau(t)} - \frac{1}{\tau_{eff}} \quad (6.11)$$

## II Results

### The influence of $SiN_x:H$ stack

The first set of samples passivated with variable  $SiN_x:H$  thicknesses as characterized before and after firing by FTIR are shown in Figure 6.28.

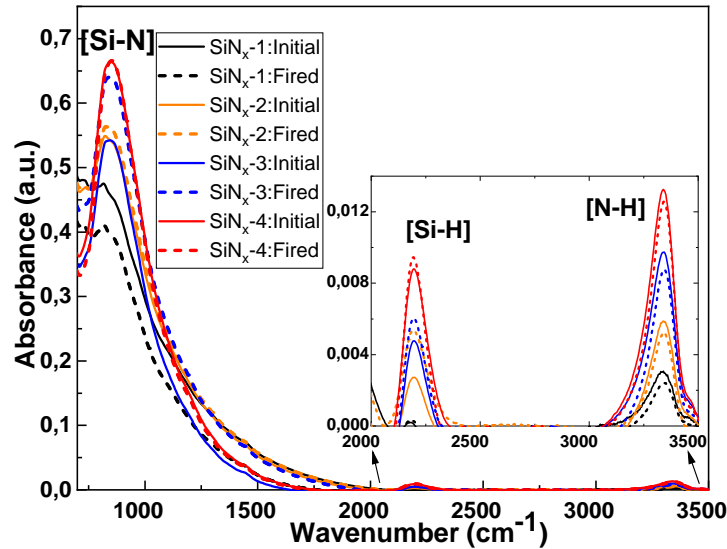


Figure 6.28: FTIR data performed on polished FZ Si samples passivated with different thickness of  $SiN_x:H$ , before and after firing at a set peak firing temperature of 935 °C. The inset shows the data on a different scale. [105].

The three significant peaks include [Si-N], [Si-H] and [N-H] stretching modes corresponding  $\sim 845\text{ cm}^{-1}$ ,  $\sim 2200\text{ cm}^{-1}$  and  $\sim 3300\text{ cm}^{-1}$ . With the particular focus on hydrogen-related bonds, the inset shows a trend of increasing absorbance for both [Si-H] and [N-H] bonds with increase in  $SiN_x:H$  thickness, which indicates the increase in hydrogen content with the film thickness. Moreover, after firing, a reduction in [N-H] bond density is found for all the samples. In contrast, an increase in IR absorption corresponding [Si-H] bond has also been observed.

The mc-Si samples passivated with different thicknesses of  $SiN_x:H$  are tested for LeTID at 130 °C under  $26.6\text{ kW/m}^2$  illumination intensity. The progression of NDD is shown in Figure 6.29a.

For all the samples, an initial increase in NDD is observed, the extent of which strongly correlated with the thickness of  $SiN_x:H$  film. All the samples reached the maximum degraded state around similar time  $\sim 100\text{ s}$ , however the extent of maximum degradation is about seven times for  $SiN_x-4$  as compared to  $SiN_x-1$ . Moreover, the partial pressure of effused hydrogen gas molecules from the this set of samples are displayed in Figure 6.29b as a function of annealing temperature.

The results clearly show that with the increase in film thickness, there is an increase in the amount of hydrogen in the film and the corresponding hydrogen effusion during the annealing process. The hydrogen spectra of  $SiN_x:H$  show the typical two component peak structure for all the samples, one at low temperature (LT) of  $\sim 700\text{ °C}$  and a peak at high

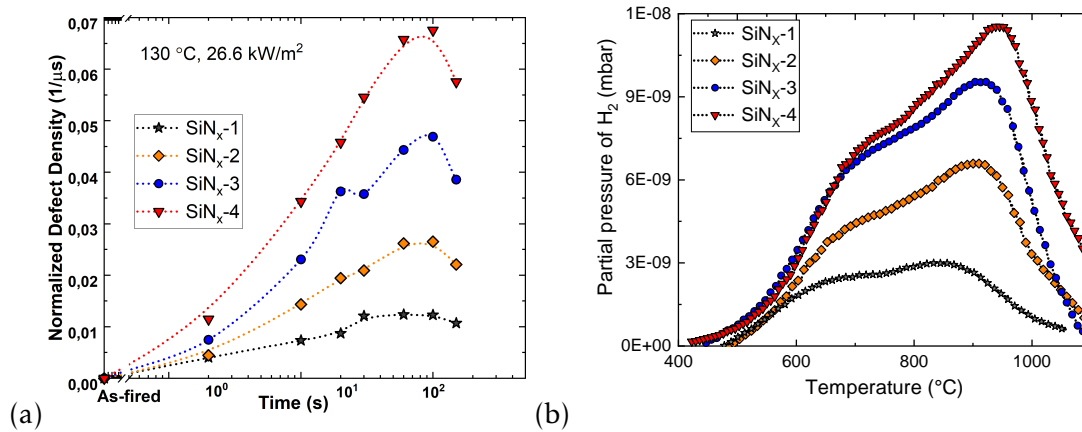


Figure 6.29: a) Normalized defect density (NDD) test of mc-Si samples deposited by multiple  $SiN_x : H$  thicknesses as a function of cumulative laser time under accelerated degradation condition of  $26.6 \text{ kW/m}^2$  at  $130 \text{ }^\circ\text{C}$  [105] b) Hydrogen effusion spectra of samples passivated with  $SiN_x : H$  of various thicknesses.

temperature (HT) of  $\sim 900^\circ\text{C}$ . Whereas, the second peak shifts from  $850 \text{ }^\circ\text{C}$  in  $SiNx-1$  with thickness of  $\sim 50 \text{ nm}$  to  $950 \text{ }^\circ\text{C}$  in  $SiNx-4$  with thickness of  $\sim 200 \text{ nm}$ . Hydrogen evolution at higher temperatures can be explained by the increase of diffusion coefficient that is proportional to the film thickness [63].

### The influence of $AlO_x$

Figure 6.30a shows the evolution of defect densities versus time when the samples with  $SiNx : H$  and  $AlO_x$  based stacks are tested under high-intensity laser illumination of  $38 \text{ kW/m}^2$ . With all the samples showing an increase in NDD followed by a recovery, the  $Si/AlO_x/SiNx : H$  sample showed minimum degradation while  $Si/SiNx : H/AlO_x$  showed the highest degradation extent.

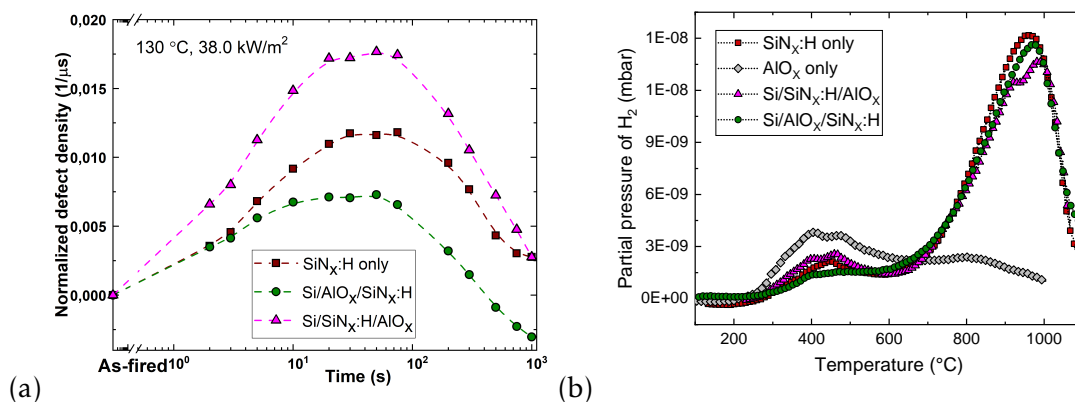


Figure 6.30: a) NDD evolution of mc-Si sample that are passivated with various  $SiNx : H$  and  $AlO_x$  stacks under illumination intensity of  $38 \text{ kW/m}^2$  at  $130 \text{ }^\circ\text{C}$  [105] b) Partial pressure of molecular hydrogen  $H_2$  effused from set 2 of samples.

In addition to the LeTID test, the hydrogen effusion spectra of the second set of samples are



measured and shown in Figure 6.30b. The partial pressure of the hydrogen effusion from two single layers of  $SiN_x : H$  and  $AlO_x$  as well as the stacked layers of  $Si/AlO_x/SiN_x : H$  and  $Si/SiN_x : H/AlO_x$  are plotted as a function of the annealing temperature. A relatively low hydrogen release is observed from the single layer of  $AlO_x$ . The maximum effusion occurs at a temperature of  $\sim 400$  °C, where the peak has a double peak structure. In the  $SiN_x : H$  single layer, the spectra contain a small peak at low temperature of  $\sim 450$  °C, followed by a large peak at high temperature of  $\sim 950$  °C.

It is calculated and reported that the amount of hydrogen-related bonds in PECVD grown  $SiN_x : H$  is  $\sim 8$  times higher than the ALD  $AlO_x$  layer [106], but in terms of hydrogen effusion measurement it is a factor of  $\sim 3$ . This significant difference can be explained by the amount of non-bonded hydrogen or  $H_2$  molecules present in the film network which would be included in the effusion spectra. The stacked layers show hydrogen effusion with some similarity to the single layers. Focusing on the  $Si/SiN_x : H/AlO_x$  stacked layer, both the peaks at low and high temperature show the double peak structure similar to the single layer of  $AlO_x$ . Whereas, in  $Si/AlO_x/SiN_x : H$  the trend is close to  $SiN_x : H$  single layer with a slight lower peak height at both low and high temperature. Considering the firing temperature of  $\sim 830$  °C, the results indicate that by using the stacked layer, the release of hydrogen at high temperatures can be suppressed compared to the single layer of  $SiN_x : H$ .

### III Discussion

#### The influence of hydrogen concentration on LeTID

Effusion measurements revealed that more hydrogen is effused from thicker  $SiN_x : H$  layers during annealing (Figure 6.29b). A kinetics of hydrogen released during the firing step is monitored using the effusion mass spectroscopy. Figure 6.31 illustrates the maximum values of NDD in the first set of samples obtained in Figure 6.29 vs. integrated area under the effusion spectra up to annealing temperature of 850 °C.

As it is shown by Wieringen et al. [12] and Sheoran et al. [13] that the hydrogenation in crystalline silicon (c-Si) at high temperature is not diffusion limited, it is reasonable to assume that effusion in the ambient and in-diffusion of hydrogen in bulk are proportional. Thus, more hydrogen effusion indicates that potentially more hydrogen diffused into the substrate, which led to higher NDD. It suggests that more hydrogen present at the interfaces and in the bulk could assist in the formation of the LeTID defect within the bulk material during light-soaking. Hence, the presented trend between NDD and the effused H-content is consistent with a hydrogen-related defect responsible for the observed degradation. However, the difference between maximum NDD measured in  $SiN_x-1$  and  $SiN_x-4$  is obtained about seven times, where the amount of effused hydrogen from  $SiN_x-4$  is only three times higher than  $SiN_x-1$ .

The shape of the effusion spectra in Figure 6.28 did not change significantly due to the increase in film thickness. This means that the binding structure of  $SiN_x : H$  is independent of the deposition time and therefore, its thickness. However, the *LT* peak is more pronounced in

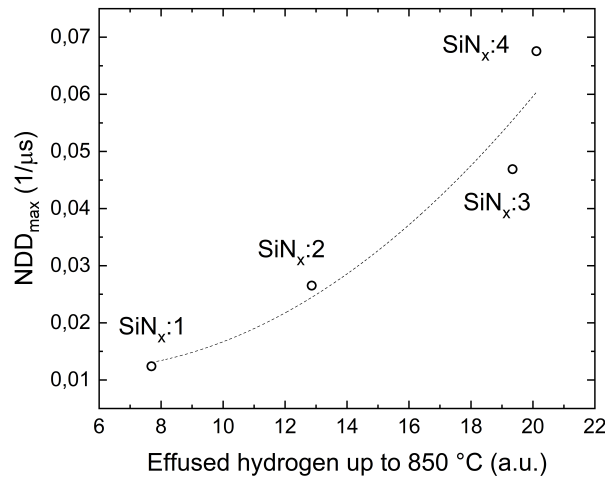


Figure 6.31: Maximum normalized defect densities ( $NDD_{max}$ ) of the samples passivated with multiple thicknesses of  $SiN_x : H$  layers vs. integrated area under the effusion spectra up to temperature of  $\sim 850$  °C. The line is a guide to the eyes.

thinner films and decreases with increasing film thickness. This can be attributed to the presence of  $H_2$  molecules at the surface, which affects the peak relatively more significantly in the thinner samples. This can likely explain why the cumulative hydrogen content is not linear to the thickness in Figure 6.31.

It is known that during effusion measurement [109], hydrogen release from  $SiN_x : H$  films at low temperature ( $LT$ ) is attributed to the  $H_2$  molecules desorbing from the surface, followed by hydrogen atoms from rupture of the [Si-H] bonds below 800 °C. The desorption of  $H_2$  from the surface affects the  $LT$  peak of thinner films more strongly, therefore, this peak is relatively higher for thinner films and decreased with increasing film thickness. This could partly explain the nonlinear dependence between the film thickness and cumulative hydrogen effusion. Whereas the peak at  $HT$  is ascribed to hydrogen from the bonds with higher binding energy such as [N-H]. In Figure 6.29, the  $HT$  peak of hydrogen shifts to the higher annealing temperatures by increasing the layer thickness. This is earlier reported by Beyer et al. [63] and explained by the fact that the effusion measurement is affected by the diffusion of hydrogen through the  $SiN_x : H$  film. The diffusion-limited effusion of hydrogen could thus have resulted in a shift of the  $HT$  peak towards higher temperatures for thicker  $SiN_x : H$  films at a contacts heating rate.

On the other hand, the extent of the LeTID increased significantly with  $SiN_x : H$  thickness. However, the increase in NDD and effused hydrogen are not linearly correlated. This is possibly the result of (i) inaccuracy of sampling and measurements, (ii) another unknown defect candidate playing a role in LeTID. The latter is highly likely as a possibility of metallic impurities affecting the LeTID extent has been reported earlier [101] [110] [111] [112]. The combination of two methods, FTIR and effusion mass spectroscopy also revealed some information about the film composition and mechanism of hydrogen transport in  $SiN_x : H$ . FTIR showed that the [N-H] bonds are the primary hydrogen bonds in the films, which

explains the reasoning behind the HT peak being the maxima in the effusion spectra. Moreover, IR spectroscopy shows that the [N-H] related peak reduced after firing which explains the release of hydrogen from  $SiN_x : H$  films during high-temperature firing. However, [Si-H] related IR peak increased which has also been reported earlier by Verlaan et al. [23] and has been explained by the increase in the density of the films after annealing. Considering effusion spectra of these films with *LT* peak below 800 °C, it can be assumed that almost all the [Si-H] bonds would be broken during firing. The increase in [Si-H] bonds can be then described by freed hydrogen diffusion in the film, meeting silicon dangling bonds and forming new [Si-H] bonds. However, the position of the HT peak is at ~850 °C, thus the typical firing temperature is not sufficient to break all [N-H] bonds and freed hydrogen is more likely to bond with silicon atoms than nitrogen. In this regard, we have previously reported that the increase of N content in  $SiN_x : H$  film can work as a barrier to hydrogen getting diffused [1].

#### $AlO_x : H$ as a barrier for hydrogen effusion

In the second set of samples, the influence of  $AlO_x : H$  layers on the evolution of NDD and the hydrogen effusion mechanism has been studied. Similar to Figure 6.31, Figure 6.32 indicates a relationship between the hydrogen effusion from the samples up to a temperature of 850 °C vs. the maximum NDD ( $NDD_{max}$ ).

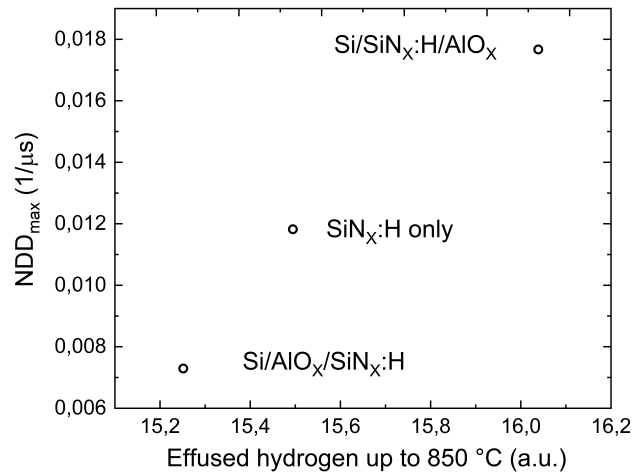


Figure 6.32:  $NDD_{max}$  of sample passivated with variable  $SiN_x : H$  and  $AlO_x : H$  stacks as a function of integrated area under the effusion spectra up to temperature of ~850 °C.

It must be noted that the hydrogen effused from the stacked layers and single films of  $SiN_x : H$  show a slight difference compared to  $SiN_x : H$  stacks in Figure 6.31. While the  $NDD_{max}$  is about ~ 60% higher in  $Si/SiN_x : H/AlO_x : H$  compared to  $Si/AlO_x : H/SiN_x : H$ , the H effusion difference is only ~ 5% between the two samples. The unexpected high release of hydrogen from  $Si/SiN_x : H/AlO_x : H$  can be explained by high tendency of  $AlO_x : H$  to absorb water from the ambient which is more likely when it is the top film [113]. The higher amount of absorbed water leads to an increased H signal relatively to the  $SiN_x : H$  samples.

A similar hydrogen release from a single  $\text{SiN}_x : \text{H}$  films to stack layers shows that the nitride layer dominates the hydrogen release. Regarding hydrogen effusion spectra in Figure 6.30 from a single  $\text{AlO}_x : \text{H}$  film, most of the hydrogen is released at  $\sim 400$  °C.

It can be due to this fast release of hydrogen; the material densifies at higher temperatures and becomes a barrier for hydrogen [114]. Another possibility could be the high surface desorption of  $\text{H}_2$  due to water absorption on the surface of  $\text{AlO}_x : \text{H}$ . However, testing which of the above two possibilities is beyond the scope of this work. The double peak structure in hydrogen effusion spectra of a single  $\text{AlO}_x : \text{H}$  film at low temperature might be attributed to loss of hydrogen in two forms,  $-\text{OH}$  bonds and molecular hydrogen  $\text{H}_2$  present in the  $\text{AlO}_x : \text{H}$  film or at its surface [114].

The stacked layer of  $\text{Si}/\text{SiN}_x : \text{H}/\text{AlO}_x : \text{H}$  is the closest to  $\text{AlO}_x : \text{H}$  single layer since the  $\text{AlO}_x : \text{H}$  is the top-most layer in both the cases. This would mean that the hydrogen release from  $\text{Si}/\text{SiN}_x : \text{H}/\text{AlO}_x : \text{H}$  at low temperature is attributed to  $\text{AlO}_x : \text{H}$  layer and at higher temperature to  $\text{SiN}_x : \text{H}$ . This is also indicated by the double peak structure caused by  $\text{AlO}_x : \text{H}$  and the LT peak of  $\text{SiN}_x : \text{H}$ .

Comparing the two stacked layers, there are differences in both the LT and HT effusion. At LT, the  $\text{Si}/\text{SiN}_x : \text{H}/\text{AlO}_x : \text{H}$  sample shows a similar LT peak, albeit at a lower partial pressure, compared to the  $\text{Si}/\text{AlO}_x : \text{H}$  sample. This can again be attributed to  $\text{H}_2\text{O}$  and  $\text{H}_2$  at the  $\text{AlO}_x : \text{H}$  surface. These peaks are not appeared for the  $\text{Si}/\text{AlO}_x : \text{H}/\text{SiN}_x : \text{H}$  sample which is likely related to the fact that any  $\text{H}_2$  or  $\text{H}_2\text{O}$  absorbed at the  $\text{AlO}_x : \text{H}$  surface prior to the  $\text{SiN}_x : \text{H}$  deposition is released during pre-deposition heating. The HT effusion peak position is significantly different for the various samples. The  $\text{Si}/\text{AlO}_x : \text{H}/\text{SiN}_x : \text{H}$  and  $\text{Si}/\text{SiN}_x : \text{H}$  samples show very similar HT peaks and peak positions, while for the  $\text{Si}/\text{SiN}_x : \text{H}/\text{AlO}_x : \text{H}$  sample, the peak looks quite different and is shifted to higher temperatures. Similar as in the case of the thicker  $\text{SiN}_x : \text{H}$  films, it is hypothesized that this peak shift is caused by a lower diffusion coefficient of the  $\text{AlO}_x : \text{H}$  film.

In Figure 6.32, the  $\text{NDD}_{max}$  is plotted as a function of the effused hydrogen up to 850 °C. It can be seen that there is only a very small difference between the total amount of hydrogen effused from all three samples, while a significant difference in  $\text{NDD}_{max}$  is measured. This can most likely be attributed to the significantly lower hydrogen diffusion coefficient in ALD  $\text{AlO}_x : \text{H}$  which inhibits hydrogen effusion to the ambient when it is the top film or hydrogen diffusion to the Si bulk when it is in between Si and  $\text{SiN}_x : \text{H}$  during a rapid firing step while the impact is relatively minimal during a slow thermal effusion experiment.

## Conclusion

In this work, we investigated the role of hydrogen in LeTID by measuring the hydrogen effusion from the samples during high-temperature firing and comparing it with the defect density introduced via accelerated LeTID testing. We tested the samples passivated with different  $\text{SiN}_x : \text{H}$  thicknesses and a direct correlation between the increase in  $\text{SiN}_x : \text{H}$  thickness, effused hydrogen content, and the LeTID extent was found. It affirms the speculations of the significant role of hydrogen in the generation of defects that lead to bulk degradation pertaining to LeTID. However, the increase in NDD and hydrogen effusion were

not linearly correlated. In addition, minor changes in the total hydrogen effusion were observed when  $AlO_x : H$  layers were used. A single  $AlO_x : H$  layer has a relatively higher hydrogen effusion at low temperatures (and much lower than  $SiN_x : H$  passivated samples) below 500 °C, likely resulting from surface  $H_2$  and  $H_2O$ . The total amount of hydrogen effused from thin film stacks of  $AlO_x : H$  and  $SiN_x : H$  was found to be very similar, while significant differences in LeTID were detected. The hydrogen effusion measurements indicated a slower hydrogen diffusion when  $AlO_x : H$  was used as the top layer, which is consistent with the hypothesis that ALD  $AlO_x : H$  layers act as a hydrogen barrier during a rapid thermal anneal. However, the understanding of the  $AlO_x : H$  as a barrier to hydrogen effusion requires further work.



## Chapter 7

# Impact of Plasma Texturing on Passivation Mechanism of $SiN_x : H$ Layers

### 7.1 Motivation

Plasma-textured black silicon surfaces can highly improve the efficiency of solar cells due to the consequent increase of the short-circuit current  $I_{SC}$  as the result of (i) less light reflection and more absorption of photons with energy near the band gap edge and (ii) stronger light trapping, which permits the reduction of the absorber thickness to lower the undesirable non-radiative bulk recombination [115] [116] [117]. However, the increase of the surface area multiplies the surface recombination rate which suppress the cell efficiency, therefore, a high-quality surface passivation is required.

In the previous chapter, the  $SiN_x : H$  passivation layers are analyzed and classified regarding their film stoichiometry and corresponding hydrogen transport mechanisms during firing process. The aim is to improve the hydrogen passivation by guiding more hydrogen to the interface and the Si bulk during firing and to find the optimal passivation layer for Si solar cells. The two significant deposition parameters, the gas flow ratio and the substrate temperature, that strongly influence the properties of  $SiN_x : H$  are already studied on planar silicon wafers. In this chapter, the influence of the Si surface roughness and plasma etch parameters on the passivation quality of  $SiN_x : H$  layers is studied and the possible reasons will be discussed, followed by several suggestions for future optimization.

## 7.2 Passivation of plasma-textured silicon wafers by $SiN_x : H$ layers

### 7.2.1 Fabrication of black Si using ICP+CCP processes

Parallel inductively- and capacitively-coupled plasma (ICP+CCP) is applied with plasma power of 60 W and 50 W, respectively, at a frequency of 13.56 MHz using an *Oxford Plasmalab System 100 ICP 65*. A gas mixture of  $O_2 + SF_6$  is used for surface texturing of n-doped FZ-Si wafers at temperature of 5 °C for 10 min. A gas ratio  $O_2/SF_6$  of 1.125 and a constant process pressure of 50  $\mu$ bar are applied. Result is shown in Figure 7.1. The SEM cross-section image indicates the formation of silicon needles at the surface with a width of  $\sim 100$  nm and a height of  $\sim 500$ -600 nm.

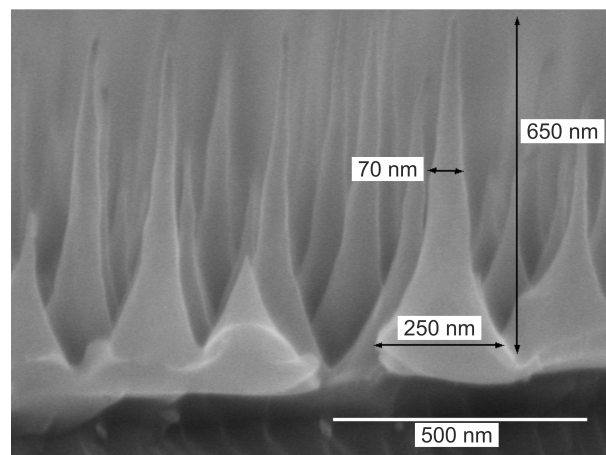


Figure 7.1: Cross-section image of plasma-textured black silicon after 10 min ICP+CCP etching process.

### 7.2.2 The influence of various gas flow ratio $R$ on passivation quality

After the plasma etch process and the RCA surface cleaning, the wafers are dipped in hydrofluoric acid for 1 min. After that, the  $SiN_x : H$  layers with various gas ratios  $R$  ( $R_{0.1}$  to  $R_{0.9}$ ) are deposited on both sides of the wafers. The applied deposition parameters are identical to those used for planar wafers. The SEM images obtained after the deposition of  $SiN_x : H$  layer on the surface of black silicon are shown in Fig7.2 in cross-section view. The height of pillars are in good agreement with the Si needles observed in Figure 7.1. The broken pillars at the cut edge reveal that the Si needles are evenly covered with the  $SiN_x : H$  layer.

After deposition of  $SiN_x : H$ , the effective minority carrier lifetime are measured using the QSSPC method. Moreover, the effusion mass spectroscopy are applied to investigate the hydrogen transport mechanisms. Afterwards, the samples are fired at  $\sim 800$  °C for few seconds and the effective lifetime is measured again after firing. The films deposited on planar wafers presented in the previous chapter are used as the references. The  $SiN_x : H$  film properties deposited on textured wafers are assumed to be identical to the references (see section II in chapter 6).



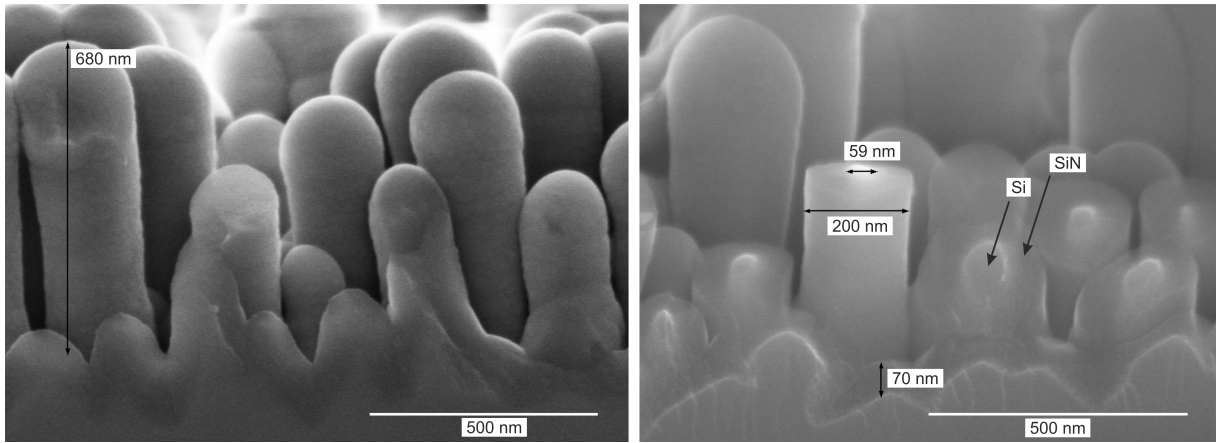


Figure 7.2: SEM cross-section view images of plasma-textured black silicon deposited by  $SiN_x:H$  layer using gas flow ratio  $R0.5$ .

### The influence of $R$ on the passivation quality of $SiN_x:H$ deposited on black Si

The effective carrier lifetimes measured before and after the firing for textured wafers passivated by  $SiN_x:H$  layers are shown in Figure 7.3a and b, respectively. Table 7.1 lists the

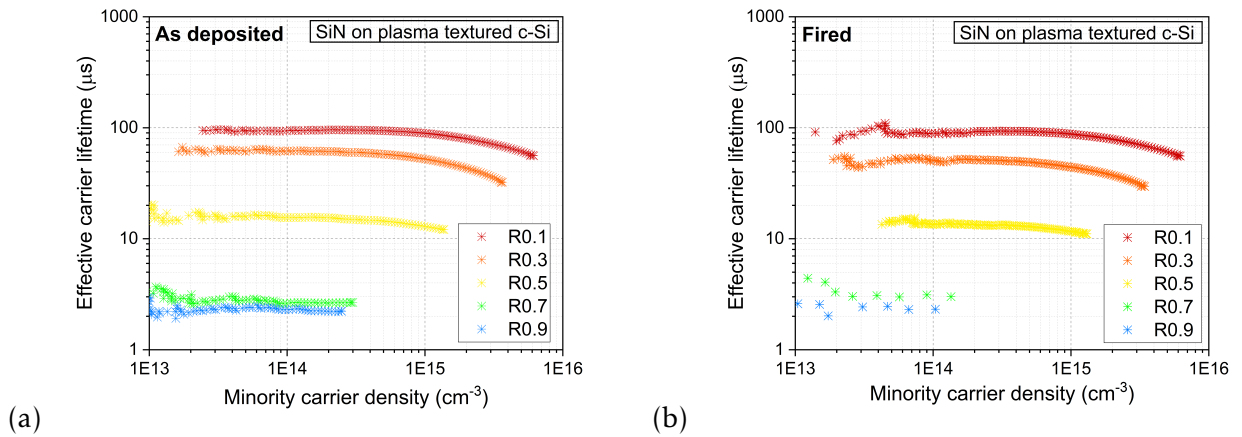


Figure 7.3: Effective charge carrier lifetime of textured samples deposited with  $SiN_x:H$  with various gas flow ratios  $R$  a) before and b) after the firing process.

effective lifetimes  $\tau$  measured at the minority carrier charge density of  $10^{15} \text{ cm}^{-3}$ . For N-rich  $SiN_x:H$  layers ( $R \leq 0.7$ ), the lifetime tester QSSPC tool was not able to detect excess charge carrier densities of  $10^{15} \text{ cm}^{-3}$  as the effective excess charge carrier lifetime of the samples is too small. A higher  $R$  (and a lower  $Si/N$  ratio) leads to enhanced effective lifetimes up to  $89 \mu\text{s}$ . No significant change can be observed after firing. This trend is similar to those of the planar samples.

### The influence of $R$ on hydrogen effusion from $SiN_x:H$ layers deposited on black Si

Hydrogen effusion experiments are performed on  $SiN_x:H$  passivated black Si wafers to find out how the surface roughness changes the hydrogen effusion mechanisms. For an easier comparison, the results of both sample sets (planar and textured) are presented in Figure 7.4a and 7.4b.

| $R$ | $\tau_{as\ deposited} (\mu s)$ | $\tau_{Fired} (\mu s)$ |
|-----|--------------------------------|------------------------|
| 0.1 | 89                             | 88                     |
| 0.3 | 52                             | 44                     |
| 0.5 | 13                             | 12                     |
| 0.7 | n.a.                           | n.a.                   |
| 0.9 | n.a.                           | n.a.                   |

Table 7.1: Effective minority charge carrier lifetime  $\tau$  obtained for SiN coated black Si samples with various gas flow ratio  $R$  as deposited and after firing.

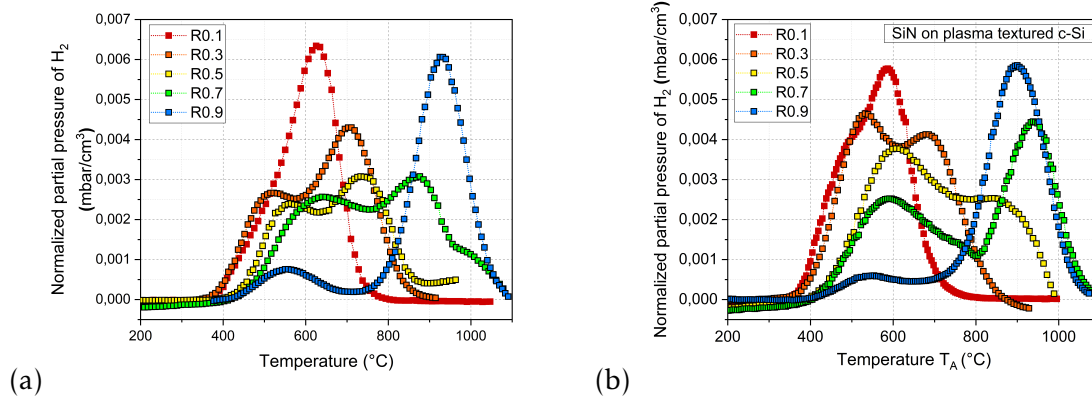


Figure 7.4: Hydrogen effusion a) on planar and b) black Si samples deposited with the  $SiN_x:H$  layers with various gas flow ratio  $R$ .

The following differences between planar and textured samples can be identified.

For  $R0.1$   $SiN$  deposited on black Si, a shoulder appears before the  $LT_A$  peak at a temperature of  $\sim 500$  °C which is not observed for the planar samples. In contrary to the planar samples, the  $LT_A$  peaks of  $R0.3$  and  $R0.5$  are higher than the  $HT_A$  peak for black Si samples.

Moreover, the  $HT_A$  peak of  $R0.5$  is shifted from  $750$  °C to a higher temperature of about  $850$  °C for textured Si samples, as well as the  $HT_A$  peak of the  $R0.7$  which is at about  $950$  °C for the textured Si sample and furthermore increased compared to the planar counterpart. The hydrogen effusion of  $R0.9$  deposited on black Si is mostly similar to planar ones, however, for the textured sample, after the  $LT_A$  peak, the hydrogen effusion rate is kept constant, and no strong decrease is observed before the  $HT_A$  peak as it is for planar samples. In total, more hydrogen effused out of the identical films when they are deposited on black Si. (Table with Intg. area under the peaks)

### 7.2.3 The influence of various deposition temperature $T_S$ on $SiN_x:H$ passivation quality

In the second phase of this experiment, textured wafers are passivated by  $SiN_x:H$  films applying different substrate temperatures and compared with the planar counterparts (see section III in chapter 6). The  $SiN_x:H$  films are deposited with a constant gas flow ratio of R0.5 and various substrate temperature of 150-400 °C.

#### The influence of various $T_S$ on passivation quality of $SiN_x:H$ deposited on black Si

The effective charge carrier lifetime is measured and plotted vs. the minority charge carrier density for the deposited textured wafers before and after firing in Figures 7.5a and 7.5b.

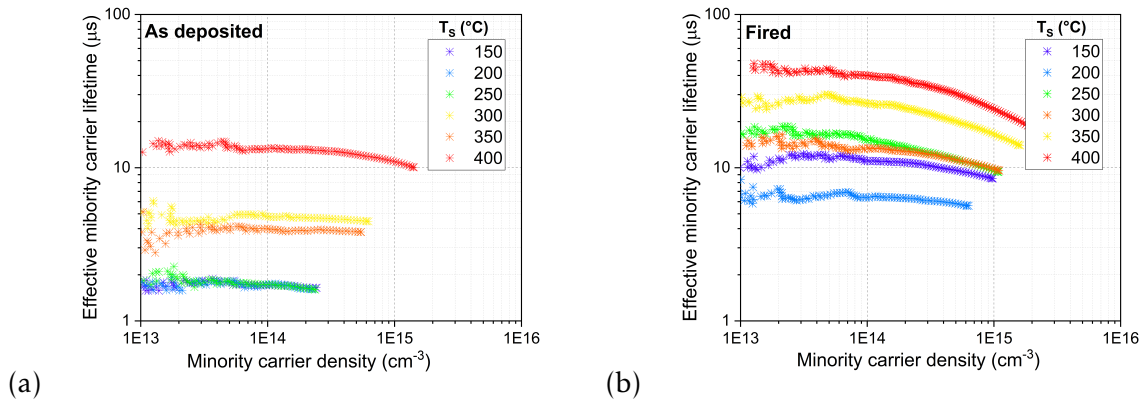


Figure 7.5: Effective charge carrier lifetime of textured samples deposited with  $SiN_x:H$  with various deposition temperatures  $T_S$  a) before and b) after the firing process.

Results are in good agreement with those observed for reference samples, where high deposition temperatures led to a higher passivation quality of  $SiN_x:H$  layers. However, the lifetime values are significantly lower as achieved for the planar samples (See Table 6.5). Finally, the firing improved the effective lifetime in all samples, which is also observed for the planar counterparts.

| $T_S$ (°C) | $\tau_{as\ deposited}$ ( $\mu s$ ) | $\tau_{Fired}$ ( $\mu s$ ) |
|------------|------------------------------------|----------------------------|
| 150        | 2.0                                | 8.5                        |
| 200        | 1.5                                | 6.0                        |
| 250        | 1.6                                | 9.4                        |
| 300        | 4.4                                | 9.7                        |
| 350        | 4.0                                | 16.5                       |
| 400        | 10.8                               | 23.8                       |

Table 7.2: Effective charge carrier lifetime measured at the minority charge carrier density of  $10^{-15} cm^{-3}$  for plasma textured Si samples deposited with  $SiN_x:H$  layers with various substrate temperature  $T_S$  before and after firing.

### The influence of various $T_S$ on hydrogen effusion from $\text{SiN}_x : \text{H}$ layers deposited on black Si

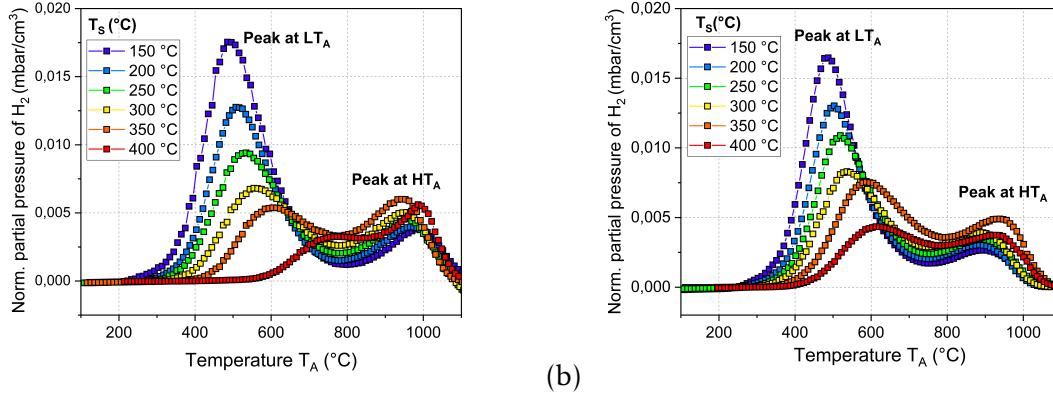


Figure 7.6: Hydrogen effusion from the  $\text{SiN}_x : \text{H}$  layers deposited with various substrate temperature ( $T_S$ ) a) on planar FZ-Si and b) on the plasma textured black Si wafers.

The results of the hydrogen effusion experiments of the  $\text{SiN}_x : \text{H}$  layers deposited with various substrate temperature  $T_S$  on black Si wafers are shown in Figure 7.6b and compared to those results of the planar counterparts in Figures 7.6a. Qualitatively, the H effusion of the two sets of sample show a similar trend, only the following differences can be identified.

The  $L T_A$  peaks widths are smaller for the black Si samples. Furthermore, the maximum of the  $L T_A$  peaks increased for the  $\text{SiN}_x : \text{H}$  layer deposited at  $T_S \geq 300$  °C compared to the planar samples. The  $L T_A$  peak is higher than the  $H T_A$  peak for all black Si samples in contrast to the planar counterparts at 300 °C and 400 °C. Moreover, for the deposition temperature of  $T_S = 400$  °C the  $L T_A$  and the  $H T_A$  peaks are shifted to lower temperature compared to the planar samples.

#### 7.2.4 Passivation of black Si surfaces by stack structure of $\text{SiN}_x : \text{H}$ layers

Similar to the planar Si samples, layers stack of three different types of silicon nitride are deposited on both sides of the plasma textured wafers. The experimental process is described in chapter 6. The effective charge carrier lifetime  $\tau_{eff}$  after deposition and after the firing are shown in Figures 7.7a and 7.7b and the values at  $\Delta n = 10^{15} \text{ cm}^{-3}$  are listed in Table 7.3. Result are similar to the reference planar samples, however, the  $\tau_{eff}$  is significantly lower. The stack structure of  $\text{SiN}_x : \text{H}$  shows relatively low passivation quality with effective carrier lifetime of 12  $\mu\text{s}$  after deposition. Si-rich  $\text{SiN}_x : \text{H}$  layer shows the highest effective lifetime after deposition and after the firing, while N-rich shows no effective carrier lifetime at minority carrier density of  $10^{15} \text{ cm}^{-3}$ . The  $\tau_{eff}$  values remain almost unchanged after firing for all measured samples.

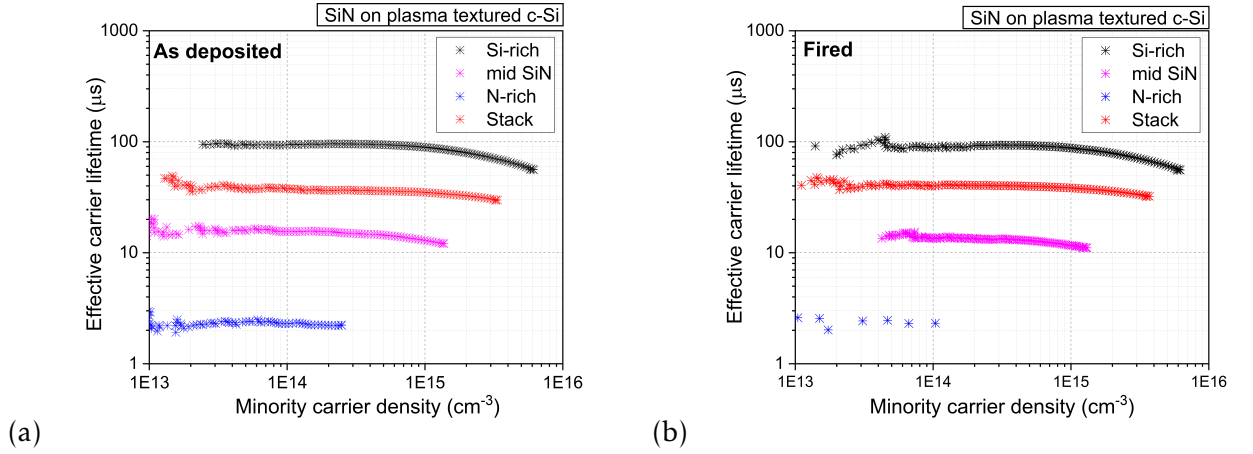


Figure 7.7: Light intensity dependent effective carrier lifetime of  $SiN_x : H$  stack deposited on plasma textured FZ-Si wafers with various gas flow ratios  $R$  a) as deposited b) after firing process.

| $R$     | $\tau_{as\ deposited} (\mu s)$ | $\tau_{Fired} (\mu s)$ |
|---------|--------------------------------|------------------------|
| Si-rich | 89                             | 87                     |
| mid-SiN | 38                             | 38                     |
| N-rich  | n.a.                           | n.a.                   |
| stack   | 12                             | 11                     |

Table 7.3: Effective charge carrier lifetime measured at the minority charge carrier density of  $10^{15} cm^{-3}$  for black Si wafers deposited by single layers and a stack of  $SiN_x : H$  films with various gas flow ratios  $R$  a) before and b) after the firing.

## 7.3 Discussion

### 7.3.1 Degradation of passivation quality of $SiN_x : H$ induced by surface texturing

In this chapter, in order to fabricate the black Si structure an etch process is carried out with a gas mixture of  $SF_6/O_2$  in an ICP+CCP plasma. The samples are then deposited by various  $SiN_x : H$  layers on both sides. The effective charge carrier lifetime is measured after deposition of  $SiN_x : H$  passivation layers. Results show similar trends for planar and plasma textured samples which are deposited by identical nitride layers. The maximum  $\tau_{eff}$  is achieved for Si-rich  $SiN_x : H$  films for both set of samples. Moreover, substrate temperature during deposition shows significant impact on the passivation quality of  $SiN_x : H$  layers. The reduction of the temperature decreases the effective charge carrier lifetime.

Nevertheless, despite of the use of identical passivation layers on the planar and plasma-textured surfaces, the effective charge carrier lifetimes of the textured samples are significantly lower than planar samples. Considering the microscopic images in Figure 7.2, the  $SiN_x : H$  layers covered uniformly the entire surface of the textured area. Therefore, it can be excluded that a non-uniform  $SiN_x : H$  is responsible for the low effective charge carrier lifetime. Regarding previous works [115] [40], two main reasons are responsible for the collapse of effective charge carrier lifetime caused by the texturing; (1) Plasma-induced

defects and (2) the enlargement of the surface area after texturing. In the following, these two reasons are discussed in more detail.

### I Plasma-induced defects and impurities

The inductively-coupled plasma (ICP) process is known to inhibit ion bombardment of the surface of the substrate during plasma etching [118]. In this work, however, the ICP and the CCP plasma are applied in parallel due to the technical instability of the ICP source. Therefore, by adding the CCP process and introducing accelerated ions with high energies (DC bias of  $\sim 130 V$ ), the generation of recombination-active defects and damages at the Si surface are plausible. The plasma-induced defects can be generated in the form of dangling bonds, Si vacancies and displacements, interstitials, metal impurities from the process chamber and more [119]. Furthermore, by using the  $SF_6/O_2$  gases, a thin layer of  $SiO_xF_y$  is deposited during etch process on the surface of silicon. Both O and F atoms compete for free Si bonds and thus a thin  $SiO_xF_y$  layer forms on the surface, which provides a certain etching barrier against F radicals. This layer can be removed from the valleys during etching since the ion bombardment is perpendicular in this area. However, it is more stable at the needle walls and can remain after plasma texturing [40]. The presence of impurities and defects at the surface of Si after etching is displayed schematically in Figure 7.8a. The remain of such impurities at the surface can suppresses the surface passivation by  $SiN_x:H$  layer.

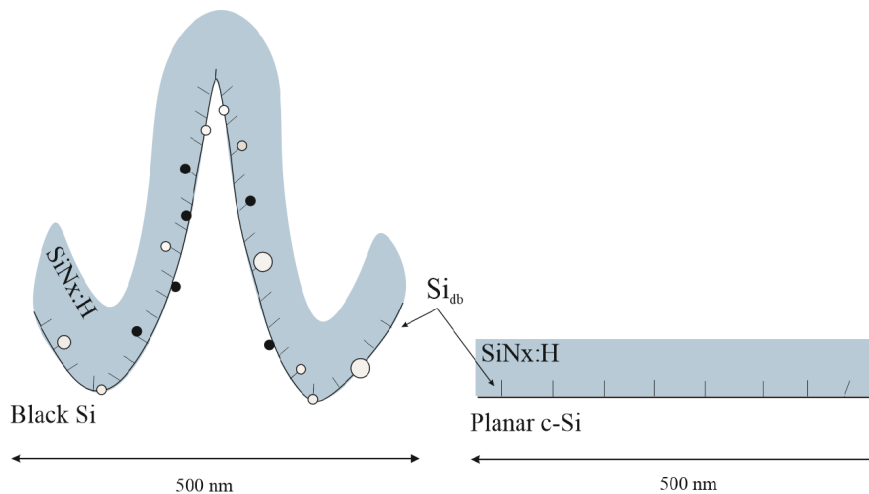


Figure 7.8: Surface impurities and defects are formed during plasma texturing process at the surface or beneath the surface and suppress the passivation quality of  $SiN_x:H$  layers in comparison with the planar samples [40]. The  $SiN_x:H$  coated planar- and textured-Si sample are shown to visualize the surface enhancement as well as the increased surface defects due to the plasma texturing.

To analyze the impact of plasma texturing on the effective charge carrier lifetime after passivation, the following parameters are introduced and calculated in this part using the model introduced by Otto et al. [115]; (i) the fraction of plasma-induced defects of textured wafers compared to their planar counterparts ( $\delta$ ) and (ii) the enhanced effective area generated by the plasma etching process ( $\gamma$ ).

The surface recombination rate ( $R_S$ ) is proportional to the concentration of the recombination-active defects ( $N_D$ ) according to Yablonoitch model, [120],

$$R_S = v_{th}\sigma N_D \quad (7.1)$$

with the thermal velocity  $v_{th}$  and the defects capture radius  $\sigma$ . Additional defect states induced by the plasma etch process increases the surface recombination and thus reduces the effective charge carrier lifetime. By assuming the bulk lifetime is infinite, the maximum surface recombination velocity is given by [115],

$$R_S \equiv R_{S \max} \leq \frac{W}{2\tau_{eff}} \quad (7.2)$$

with the wafer thickness  $W$ . The factor two is due to symmetrically double side surface passivation. Regarding the equations 7.1 and 7.2, the reduction of effective lifetime in black Si ( $\tau_{black \ Si}$ ) compared to reference planar surface ( $\tau_{planar}$ ) is related to the fraction of defects induced by the plasma ( $\delta$ ).

$$\frac{\tau_{planar}}{\tau_{black \ Si}} \propto \frac{N_{D \ black \ Si}}{N_{D \ planar}} = \delta \quad (7.3)$$

$N_{D \ planar}$  and  $N_{D \ black \ Si}$  are respectively the defect density corresponding to the planar and black silicon surfaces.

## II Effective surface enhancement

On the other hand, the enhancement of the effective surface area due to the plasma texturing is the second main factor for the increase of the surface recombination rate. (The increase of surface area is illustrated also in Figure 7.8). If it is assumed that the defects (such as dangling bonds) at the Si surface are uniformly distributed, an increased area causes an absolute increase of the surface defects and a rise of the surface recombination rate. Therefore, the difference between the effective charge carrier lifetime of black Si and planar samples is inversely proportional to the surface area enhancement ( $\gamma$ ) [121].

$$\frac{\tau_{planar}}{\tau_{black \ Si}} \propto \frac{A_{black \ Si}}{A_{planar}} = \gamma \quad (7.4)$$

$A_{planar}$  and  $A_{black \ Si}$  are respectively the effective surface area in planar and black silicon samples. Considering equations 7.3 and 7.4, the effective charge carrier lifetime measured for passivated planar surface over the black silicon is proportional to the multiply  $\delta$  and  $\gamma$ .

$$\frac{\tau_{planar}}{\tau_{black \ Si}} \propto \gamma\delta \quad (7.5)$$

Since the plasma etch conditions and the cleaning process prior to  $SiN_x : H$  deposition are

identical for all samples, it is expected that the  $\gamma$  and  $\delta$  values being constant. That means for example by depositing two types of nitride layers,  $SiN_1$  and  $SiN_2$ , on textured- and planar-Si,

$$\left(\frac{\tau_{planar}}{\tau_{black\ Si}}\right)_{SiN_1} \approx \left(\frac{\tau_{planar}}{\tau_{black\ Si}}\right)_{SiN_2} \quad (7.6)$$

To investigate this, the percentage reduction of effective charge carrier lifetimes ( $\Delta\tau$ ) in black silicon samples are calculated using the equation 7.7. Results are shown in Figure 7.9.

$$\Delta\tau = \frac{\tau_{planar} - \tau_{black\ Si}}{\tau_{planar}} \times 100 \quad (7.7)$$

It is revealed that the reduction in lifetime due to plasma texturing is significantly different between the samples. This means that the effect of plasma are not identical for all samples.

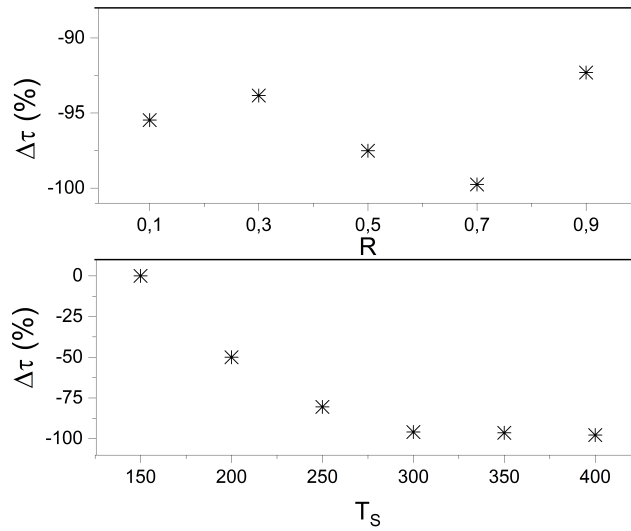


Figure 7.9:  $\Delta\tau$  is the percent reduction of effective charge carrier lifetime in the black silicon compared to the planar samples as a function of various gas flow ratios  $R$  and substrate temperatures  $T_s$  used during the  $SiN_x:H$  deposition. Although identical  $SiN_x:H$  passivation films are deposited on both planar- and plasma textured- Si wafers, the minority carrier lifetime is significantly difference.

However, observation of similar surface geometry by electron microscopy suggests that  $\gamma$  is most likely constant. Therefore, it is assumed that the difference in  $\Delta\tau$  is resulted from various concentrations of plasma-induced defects which interferes the passivation process ( $\delta$  is not constant). This can be caused by the technical instability of ICP source at the time of our experiments. A large range of  $\Delta\tau$  measured for the samples deposited at different  $T_s$  compared to different  $R$  is due to the poor passivation quality of the samples deposited at low temperatures ( $< 250$ ), even for the planar samples. This leads to an unrealistic trend.

Despite the fact that the plasma process resulted in different defect contributions in the samples, the passivation of the black Si samples by different  $SiN_x:H$  layers shows similarities to the planar reference samples. Regarding the lifetime values listed in Tables 7.1 and 7.2, the passivation quality of black Si samples show also dependency on film composition of  $SiN_x:H$ . Improved effective charge carrier lifetime is accompanied with reduction of  $R$  as



well as increase of  $T_S$ . It shows that although the variation of plasma-induced defects disturbed the ideal analytical conditions, but the properties of  $SiN_x : H$  layers still preserve the passivation quality.

### 7.3.2 Mechanism of hydrogen release from $SiN_x : H$ layers deposited on black silicon

To investigate if the plasma textured surface impacts the hydrogen effusion mechanism of  $SiN_x : H$  layers, the effusion experiments are carried out and described in section 7.2.

#### Deposition of $SiN_x : H$ layers with various $R$

The partial pressure of the effused hydrogen from  $SiN_x : H$  deposited planar and plasma textured wafers with various gas flow ratio  $R$  are presented in Figures 7.4a and 7.4b. The deposition of the  $SiN_x : H$  layers with various  $R$  on textured surfaces show the same three mechanisms of hydrogen effusion as for the planar samples. The mentioned quantitative differences will be discussed in the following.

The most noticeable difference between the two sets of samples is the increased  $LT$  peak height for plasma textured samples. The  $LT$  peak is partially attributed to surface desorption of chemisorbed water and/or molecular hydrogen  $H_2$  in the film. Larger surface areas induced by plasma texturing can increase both effects, the water chemisorption and the  $H_2$  concentration at or near the surface, and thus, rise the hydrogen effusion peak at low temperatures.

Secondly, the total hydrogen effusion from the  $SiN_x : H$  layers deposited with various  $R$  on the black Si surface are higher than those of the planar wafers. The effusion of both set of samples are normalized to the volume of the  $SiN_x : H$  layers. The volume is calculated only from the layer thickness multiplied by the area of the specimen. This means that the increase in effective area due to the black Si is not taken into account. Therefore, the higher hydrogen effusion can be related to the larger  $SiN_x : H$  film deposited on the enhanced surface of black Si.

The  $HT$  peak in effusion of the textured surfaces shifts about 100 °C to higher temperature. As a reminder, the  $HT$  peak is related to atomic hydrogen released from hydrogen bonds (mainly from the N-H bond in  $SiN_x : H$ ). Assuming an identical  $SiN_x : H$  composition in the same deposition recipe, the shift of the  $HT$  peak cannot be related to different film structures, but might be caused by plasma-induced defects. The rise of impurities and the defects at the  $Si/SiN_x : H$  interface increase the possibility of trapping hydrogen compared to the planar reference samples which can limit the release of atomic hydrogen to the ambient [122].

#### Deposition of $SiN_x : H$ layers with various $T_S$

The effusion of hydrogen from the  $SiN_x : H$  layers deposited with various  $T_S$  on planar and textured Si wafers are shown in Figures 7.6a and 7.6b, respectively. For the planar samples, a reduction of hydrogen effusion at  $LT$ s is identified as deposition temperature increases which can be attributed to the increasing film density of  $SiN_x : H$  layers. A similar trend is also

observed for the black Si samples. However, in contrast to the planar wafers, the  $LT$  peak is dominant peak for all black Si samples, which is only found at  $T_S < 350$  °C for the planar samples. Also here, the surface enlargement can explain this effect, leading to an increased surface desorption of hydrogen and, subsequent, the  $LT$  peak, even when the films are dense. This likely approves the assumption of higher surface desorption.

### 7.3.3 Conclusion and outlook

The surface roughness due to plasma texturing seems to be a major challenge for the passivation quality of  $SiN_x : H$  layers. The results show that the Si-rich  $SiN_x : H$  layer provides the best passivation for the black Si samples.

The first hypothesis that the hydrogen concentration increases due to the surface enhancement could be proved by effusion measurements. Higher  $LT$  peak indicates the higher surface desorption of hydrogen from the plasma textured samples. This can be attributed to the larger surface area deposited by the  $SiN_x : H$  layers. Moreover, a higher  $LT$  peak reveals more water chemisorption on the surface.

The second assumption, that more hydrogen improves the passivation quality after firing, is not fully supported by the results. Although the hydrogen amount effused from the black silicon samples is higher than from the planar samples, the effective charge carrier lifetimes are significantly lower after firing. This results can be explained by the high concentration of defects induced by the plasma, leading to strong surface degradation, which covers any other possible positive effects by hydrogen passivation.

For further improvement of the passivation quality, following points can be considered for further investigations.

1. Using only an inductively-coupled plasma (ICP) source for the fabrication of the black Si which can inhibit the ion bombardment during the etching process and reduce the surface degradation of Si.
2. An advanced cleaning process is essential for the intensive removal of impurities induced by the plasma.
3. Deposition of high quality thin layer of ALD-deposited  $AlO_x$  can improve the surface passivation, however, as it is mentioned in last chapter, it may limit the diffusion of hydrogen into the bulk during the firing [123].

# Chapter 8

## Summary

In **Chapter 5**, a new setup for effusion mass spectroscopy is described and discussed focusing on PV applications and in particular on the firing process, in order to study the hydrogen passivation mechanisms at high temperatures. A series of samples are measured by effusion measurements and compared with the results of NRA measurements. The results show excellent agreements with a coefficient of determination ( $R^2$ ) above 96 %. **This finding leads to the conclusion that the effusion mass spectroscopy is an alternative cost-effective and available tool for hydrogen effusion analysis.**

While comparing the two methods, the appearance of hydrogen sharp peaks (SP) in the effusion spectra is observed. A correlation between the film density and the microstructure of the a-Si:H films and the appearance of the sharp peaks at certain annealing temperatures is found. A surface deterioration is further observed for the samples showing an SP in their effusion spectra, which is caused by interfacial bubbles leading to an increased pressure and a subsequent abrupt release of hydrogen from the films with relatively high densities. A model is proposed to describe the correlation between the position of the SP and the surface deterioration.

The aim of developing the effusion setup is to investigate the influence of the firing process on the hydrogen dynamics and the passivation mechanisms. Since the time scale of the firing and the effusion experiments are different, it is necessary to investigate whether the effusion measurement could be a good reference for analyzing the firing step. For this purpose, the firing process is simulated within the effusion system and the samples are exposed to a temperature of 700 °C, close to the firing temperature, for a few minutes and the effusion of hydrogen is monitored as a function of time. The results show that the effusion of hydrogen is strongly temperature dependent and that the main part of effusion occurs at a certain temperature within the first few seconds. **Therefore, it is proved that the rapid firing process can be investigated and compared with the effusion measurements at constant heating rates which confirms the Hypothesis (1).**

In **Chapter 6**, a comprehensive investigation of the RTA process on hydrogenated passivation layers with the focus on using effusion mass spectroscopy and comparing it with standard methods such as FTIR or NRA with the aim of expanding the knowledge of

passivation mechanisms for PV applications has not yet been carried out. First, the structural analysis of  $SiN_x : H$  layers as a host material for hydrogen is investigated and discussed. A systematic analysis of PECVD-deposited  $SiN_x : H$  passivation layers is carried out, focusing on the influence of the film properties on the hydrogen effusion/diffusion mechanisms at high temperatures. Two deposition parameters, the gas flow ratio of  $[NH_3]/[NH_3 + SiH_4]$  and the substrate temperature, are identified as significant factors which strongly influence the properties of the  $SiN_x : H$  layers. **As a conclusion of the compositional study and the corresponding hydrogen effusion mechanisms, the  $SiN_x : H$  films are classified into three main groups, (1) Si-rich SiN, (2) intermediate SiN, and (3) N-rich SiN.**

The maximum of the passivation quality is achieved by the Si-rich films, however, the low density of this layer leads to a high release of hydrogen to the ambient during firing. On the other hand, layers with higher N contribution show a lower tendency to release hydrogen at firing temperatures. As conclusion, N-gradient layers stack of  $SiN_x : H$  are provided inhibiting the hydrogen out-diffusion and consequently increasing the amount of hydrogen for improved passivation of defects. **The reduction of the hydrogen effusion could be achieved by using layers stack which verifies partially the hypothesis (2b), but no significant increase of the passivation quality (effective carrier lifetime) is observed when keeping more hydrogen inside the samples. Therefore, the influence of hydrogen as described by the Hypothesis (2a) cannot be experimentally confirmed.**

In addition, for the first time the effusion mass spectroscopy is used to investigate the influence of hydrogen on the light and elevated temperature degradation (LeTID). For this purpose, two different sets of samples, (1) with different thicknesses of  $SiN_x : H$  layers and (2) with different stacked layers of  $SiN_x : H$  and  $AlO_x$  are considered. The results are compared with commonly used LeTID tests. **The results from effusion measurements confirm that the LeTID is enhanced when the hydrogen concentration increases within the  $SiN_x : H$  which also confirm the assumption that LeTID is a H-driven process. Moreover, the  $AlO_x$  can act as a barrier for hydrogen inhibiting the diffusion during the firing.**

In **Chapter 7**, the role of hydrogen in the  $SiN_x : H$  passivation of plasma-textured surfaces or so-called black Si is investigated. The role of the surface area enlargement and defects induced by the plasma are considered and the differences of the passivation mechanisms in comparison to planar surfaces are discussed. For plasma texturing, a combination of inductively-coupled and capacitively-coupled plasma (ICP+CCP) sources are applied. The measured effective lifetimes of the textured samples are in general lower than those of the polished wafers, however, the relative reduction in different samples varied. This could be attributed to the different defect concentrations induced by the plasma particles during texturing. Regarding the effusion measurements of the plasma textured samples, a similar trend could be observed for the hydrogen effusion as for the planar samples when the same deposition recipe for  $SiN_x : H$  is used. **Increase of hydrogen effusion at the low temperatures ( $LT_A$  peak) are observed for textured samples, indicating a higher total hydrogen release in comparison with planar counterparts which verifies partially the Hypothesis (3a). This can be attributed to the increased effective surface area in textured**

**samples that enhances the volume of the deposited  $SiN_x : H$  layers, leading to higher concentration of effused hydrogen.** Moreover, higher chemisorption of water molecules on a larger surface area can lead to more hydrogen effusion at low temperatures in the form of  $H_2$  molecules. **In conclusion, we cannot entirely confirm the hypothesis (3a) that more hydrogen in  $SiN_x : H$  films due to a larger film volume improves the passivation quality after firing. The high degradation of the plasma textured wafers is possibly due to the complexity of defects at the surface or near-surface induced by the plasma, which supports the hypothesis (3b).**



# Appendix A

## Appendix

### Design of Experiment (DoE)

*The influence of deposition parameters on optical and electrical properties of PECVD deposited  $SiN_x : H$  layers is investigated by using a statistical design of experiment (DoE) and the results is presented in section 6.1.1.I of this work. For this purpose, a full-factorial design is used and the result is provided here in more detail.*

Figure A.1 and A.2 show the Pareto diagram plotted for hydrogen bond densities [Si-H] and [N-H] in  $SiN_x : H$ , respectively. The bond densities are calculated as deposited and after the firing process normalized to film thicknesses (See Sec. 4.1). The deposition factors are marked with the letters A to E as indicated by the scale in Figure A.1. The Y-axis shows all the individual deposition factors (A, B,...), the interaction of two factors (AB, AC,...) and interaction of three factors (ABC, ACD,...). The standardized effect of each factor is indicated by the blue bar charts. The factor will be considered statistically significant, if its effect crosses the reference line, represented by a red dotted line. In a normal bell-shape distribution of data, the standard deviation from the zero can be expanded to which the 95 % of data are included (95 % confidence level). Any individual data out of this range at the tail of the bell-shape distribution could be significant [124]. The responses out of 95 % confidence level cross the reference line ( $\alpha = 0.05$  %).

The results after deposition of  $SiN_x : H$  layers and after the firing process (RTA) for the [Si-H] bond densities are shown in Figure A.1a and b, respectively. An analogue for [N-H] bonds is shown in Figure A.2a and b. In figure A.1a, factor D, which represents the gas flow ratio  $R$ , shows the strongest effect on [Si-H] bond density with a big difference compared to other effects. The reference bar is crossed by a number of other factors, but compared to factor D their effects are negligible. The most important factors in the PECVD process are also investigated after firing, since the actual measure is the quality of the solar cells after contact firing process. It is interesting to note that in all cases the role of the factors changes by considering the samples after the firing process.

After firing process, four factors D, B and ABD and BE cross the reference line in Figure A.1b. They represent the gas flow ratio  $R$ , gas pressure, interaction of deposition temperature, gas pressure and gas flow ratio and interaction of gas pressure and total gas flow. The gas flow ratio  $R$  still shows the greatest influence on the density of the [Si-H] bond after firing. On the

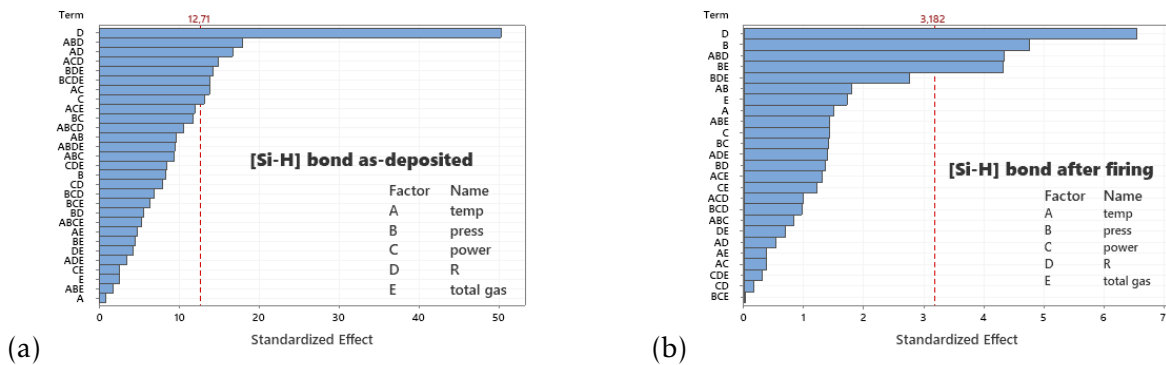


Figure A.1: The effect of deposition factors and their interactions is presented in Pareto diagram for [Si-H] bond densities in  $SiN_x : H$  films a) as deposited and b) after industrial firing process RTA.

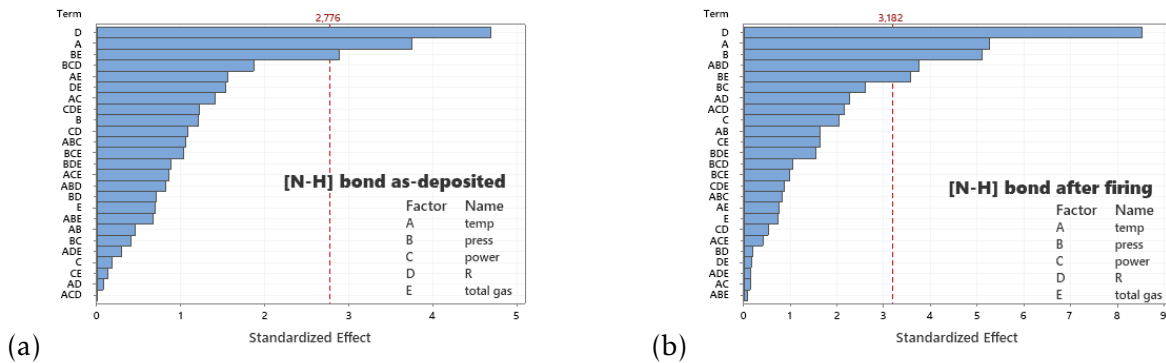


Figure A.2: The effect of deposition factors and their interactions is presented in Pareto diagram for [N-H] bond densities in  $SiN_x : H$  films a) as deposited and b) after industrial firing process RTA.

other, hand in figure A.2a [N-H] bonds as-deposited are influenced by D, A, BE, gas flow ratio, substrate temperature and the interaction of gas pressure and total gas flow respectively, whereby after firing besides these factors, B the gas pressure, and ABD the interaction of temperature, gas pressure and gas flow ratio, are being added to the significant factors.

In all four Pareto diagrams in Figure A.1 and A.2, the gas flow ratio  $R$  is the most significant factor for managing the configuration of the hydrogen bonds. Substrate temperature  $T_S$  and gas pressure are the next important factors in most cases. It can be concluded that the initial configuration of the hydrogen bonds after the deposition and also after the firing process is strongly dependent on the compound and the ratio of the gas flow during the deposition.

### DoE: The significant deposition parameters for good passivation quality

After deposition of  $SiN_x : H$  films on both sides of FZ-Si wafers, the effective lifetimes are determined by quasi-steady state photoconductance decay (QSSPC) method using a WCT-120 Sinton system. The effective lifetime is defined for carrier injection level (excess carrier intensity upon the wafer) of  $1 \times 10^{15} \text{ cm}^{-3}$  provided by bias light intensity. The Pareto effect plot of the measured effective minority carrier lifetime  $\tau_{eff}$  as-deposited is shown in Figure



A.3a and after firing A.3b. It can be seen that the substrate temperature  $T_S$  during the

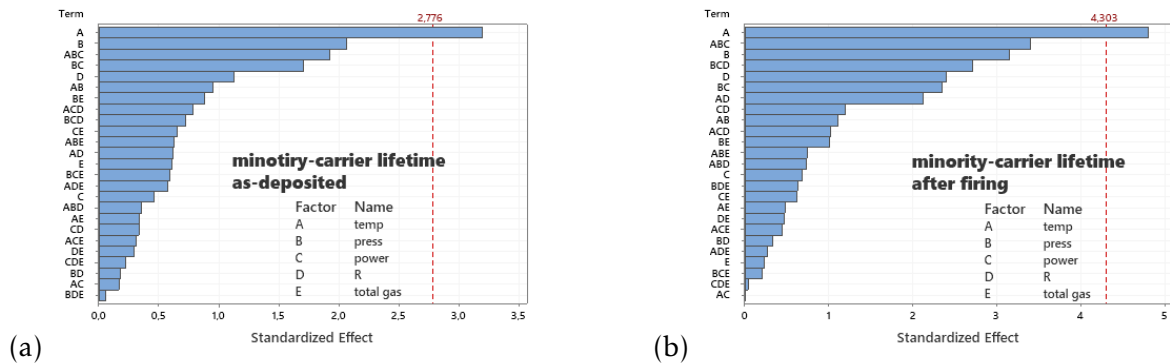


Figure A.3: The effect of deposition factors and their interactions is presented in Pareto diagram for measured effective carrier lifetime performed on polished FZ-Si wafers deposited by  $a-SiN:H$  films a) as deposited and b) after industrial firing process RTA.

deposition has a significant impact on passivation quality of  $a-SiN:H$ . The same impact is observed for measured carrier lifetime of samples after firing. The result clearly demonstrates the importance of the substrate temperature  $T_S$  as a key factor for achieving the maximum lifetime of the minority carriers. This reveals that the influence of post firing is overcome by the impact of the substrate temperature during deposition.

#### DoE: The impact of significant deposition parameters hydrogen bond density and film density

In this section a further analysis is performed to determine the influence of the obtained significant factors (inputs) on the properties of  $a-SiN_x:H$  films (outputs) such as hydrogen bonding configuration and minority carrier lifetime.

Regarding last section, the substrate temperature  $T_S$  and the gas flow ratio  $R$  influence significantly the properties of the PECVD deposited  $SiN_x:H$  films.

Figure A.4 shows the calculated  $[Si-N]$  as a relative film density of  $SiN_x:H$  that are normalized to the film thickness deduced from FT-IR spectroscopy. The 3D surface plot shows the  $[Si-N]$  as a function of two significant factors, the substrate temperature  $T_S$  and the gas flow ratio  $R$ , after deposition in Figure A.4a and after firing in Figure A.4b. It can be seen that at the deposition temperature of 300 °C and the  $R=0.5$  (center point, see Table 6.1), the  $[Si-N]$  reaches a peak both as-deposited and after firing. Moreover, a slight increase of  $[Si-N]$  is observed as  $T_S$  increases from 200 °C to 400 °C and  $R$  increases from 0.1 to 0.9. After firing the  $[Si-N]$  increased in nearly all samples but a sharper increase is observed in the peak, hence the center point recipe resulted in greater film density. The result suggest that both  $R$  and  $T_S$  strongly affect the concentration of  $[Si-N]$  bond. Furthermore, the firing leads to release of hydrogen and the deification in the network, shown by increase of  $[Si-N]$ , but the film structure after firing shows similarity to its initial after deposition.

Similar to  $[Si-N]$  bond, the  $[Si-H]$  and  $[N-H]$  bond densities are calculated in all films and normalized to their thicknesses. The 3D surface plots in Figures A.5 and A.6 demonstrates

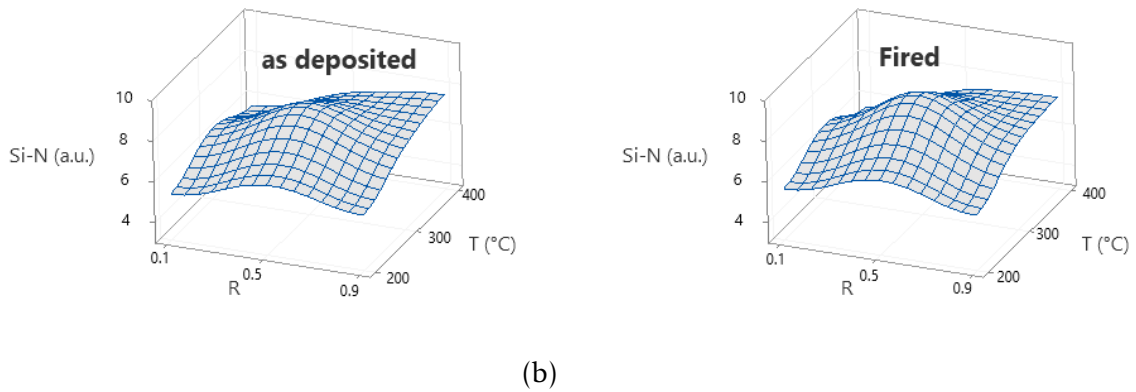


Figure A.4: Surface plot of Si-N bond density vs. deposition temperature and gas flow ratio for  $SiN_x:H$  coated FZ-Si wafers a) as deposited and b) after the firing process (RTA) at 800 °C for about 1 min.

respectively the [Si-H] and [N-H] as a function of substrate temperature  $T_S$  and gas flow ratio  $R$ . The results after deposition and after firing are labeled by a and b in the figures. Figures A.5a and A.5b show a very similar behavior, the [Si-H] bond concentration reduces drastically as  $R$  increases from 0.1 to 0.9. A similar peak to that observed in Figure A.4 is revealed at center point ( $T_S$  of 300 °C and  $R$  of 0.5) both as-deposited and after firing. However, the maximum of [Si-H] is observed at  $R$  of 0.1 independent on the substrate temperature.

In Figure A.6a, [N-H] bond concentration increases with  $R$  in contrast to [Si-H] bond

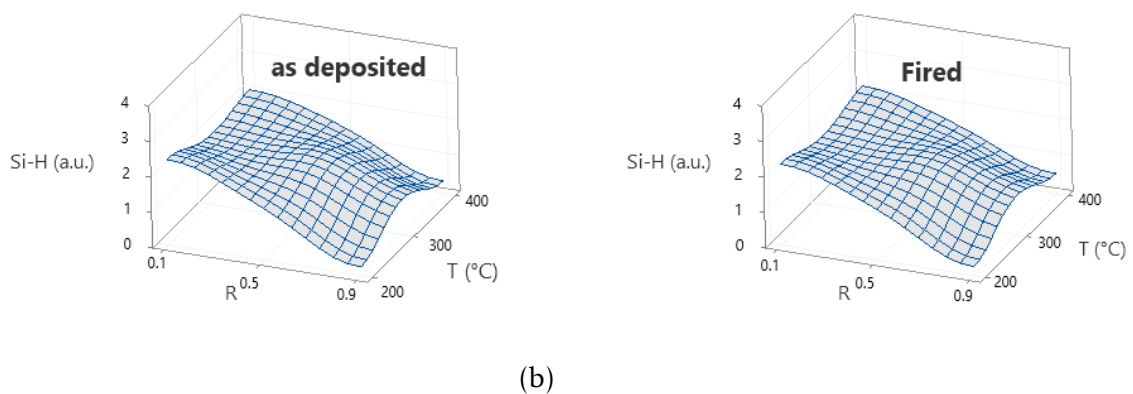


Figure A.5: Surface plot of Si-H bond density vs. deposition temperature and gas flow ratio for  $a-SiN_x:H$  coated FZ-Si wafers a) as deposited and b) after the firing process (RTA) at 800 °C for about 1 min.

concentration. After firing the trend remains unchanged. Moreover, a concavity on the 3D surface of [N-H] bond concentration has appeared at center point which is inverse to what observed for [Si-N] and [Si-H] bond density at this point. Results suggest that the influence of

gas flow ratio  $R$  is more significant than substrate temperature  $T_S$  on the bonds configuration in  $SiN_x:H$  films. Applying the deposition recipe of center point results in a denser  $SiN_x:H$  films with maximum of [Si-N] bonds, however, the hydrogen bond densities [Si-H] and [N-H] are highly influenced with increase of gas flow ratio. The role of firing is overcome by the deposition recipe and impact of significant factors.

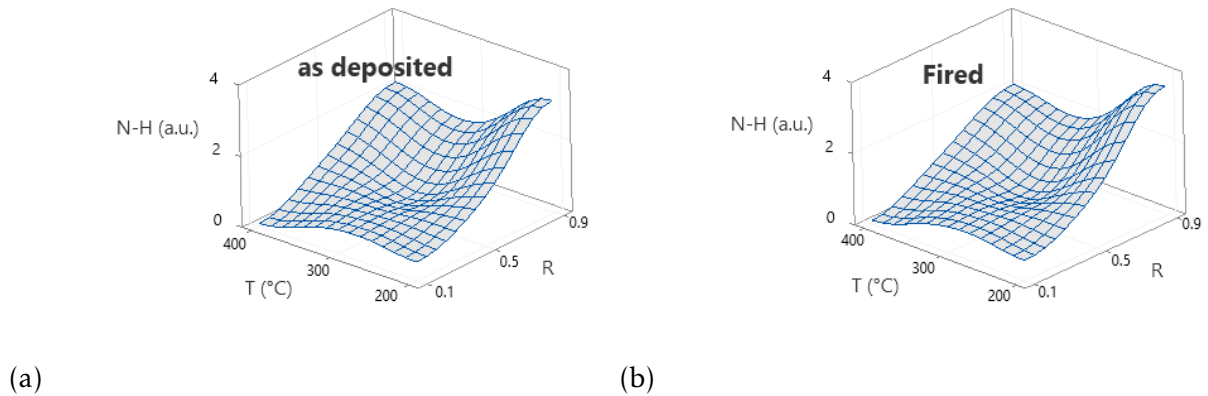


Figure A.6: Surface plot of [N-H] bond density vs. deposition temperature and gas flow ratio for  $SiN_x:H$  coated FZ-Si wafers a) as deposited and b) after the firing process (RTA) at 800 °C for about 1 min.

#### DoE: The impact of significant parameters on effective minority carrier lifetime

A further investigation on the impact of significant factors on the passivation quality of  $SiN_x:H$  films are performed by plotting the measured effective carrier lifetime  $\tau_{eff}$  as a function of gas flow ratio  $R$  and substrate temperature  $T_S$ . Figure A.7a and A.7b shows the effective carrier lifetime obtained from QSSPC method at the minority carrier intensity of  $10^{15} \text{ cm}^{-3}$  after the deposition and after the RTA treatment. After deposition, the maximum of  $\tau_{eff}$  is revealed at  $T_S$  of 400 °C and  $R$  of 0.1. It can be noted that only at the  $T_S$  of 400 °C, the reduction of  $R$  results in a large increase of  $\tau_{eff}$ . After firing, the maximum of  $\tau_{eff}$  remained at  $T_S$  of 400 °C and  $R$  of 0.1 similar to initial value after deposition. However, the firing strongly improved the  $\tau_{eff}$  of samples deposited by the center point's recipe. It can be concluded that a relatively high substrate temperature  $T_S$  above 300 °C during the deposition of the  $SiN_x:H$  layers is essential for achieving a good quality passivation and a high effective carrier lifetime.

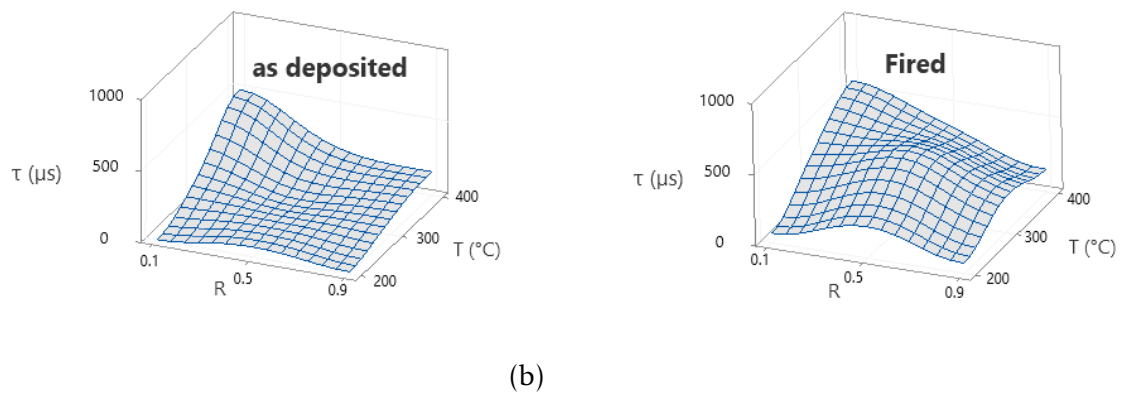


Figure A.7: Surface plot of effective minority carrier lifetime  $\tau$  vs. deposition temperature and gas flow ratio for  $\text{SiN}_x : \text{H}$  coated FZ-Si wafers a) as deposited and b) after the firing process (RTA) at  $800^{\circ}\text{C}$  for about 1 min.

# List of Figures

|     |  |    |
|-----|--|----|
| 2.1 | Different recombination processes in semiconductor. . . . .  | 6  |
| 2.2 | Illustration of surface states at the surface of silicon with band gap of $E_g$ at its interface with dissimilar materials such as $SiN_xH$ with $E'_g$ . . . . .  | 8  |
| 2.3 | Impact of two mechanisms of passivation (1) chemical passivation of surface states $D_{it}$ (red line) and (2) field-effect passivation (dashed line) [17]. . . . .  | 9  |
| 2.4 | A schematic of the band bending at the interface of $Si/SiN_x : H$ in thermal equilibrium (in dark) due to the positive fixed charges related to $K^+$ centers [26].   | 10 |
| 3.1 | Schematic of Oxford Plasmalab 100 PECVD system. . . . .  | 14 |
| 3.2 | An illustration of plasma etch chamber (RIE) with inductively- (ICP) and capacitively-coupled plasma (CCP) sources. . . . .  | 15 |
| 3.3 | An example of a rapid thermal annealing process with a set peak temperature of 885 °C measured on a passivated mc-Si wafer. It can be clearly seen that the measured sample temperature is significantly lower than the peak temperature [41]. . . . .   | 16 |
| 4.1 | IR absorption spectra of $SiN_x : H$ film as function of wave number indicating three main peaks of $Si - N$ , $Si - H$ and $N - H$ in stretching mode. . . . .  | 17 |
| 4.2 | A schematic of a photoconductance charge carrier lifetime tester <i>WCT-120</i> . . . . .  | 19 |
| 4.3 | Circuit diagram of the C-V measurement system, Keithley 4200-CVU [49]. . . . .   | 21 |
| 4.4 | Interaction of electrons with atoms and the signals that are generated in various depth of the sample. . . . .   | 22 |
| 5.1 | A photograph of gas effusion mass spectrometer setup at Fraunhofer CSP, the main compartments are labeled. . . . .   | 25 |
| 5.2 | Schematic illustration of the effusion mass spectroscopy. . . . .  | 26 |
| 5.3 | A screen shot of software program. . . . .   | 27 |
| 5.4 | A screen shot of software program Easy view. . . . .   | 27 |
| 5.5 | An example of hydrogen effusion spectrum of PECVD deposited $SiN_x : H$ and $a - Si_x : H$ films. The normalized partial pressure of molecular hydrogen is measured as a function of heating temperature. The peaks' position in the effusion spectrum are composition-dependent and shift to higher temperatures with incorporation of more nitrogen in film. . . . . | 28 |

|      |   |    |
|------|---|----|
| 5.6  | a) The partial pressure of effused hydrogen from five different $SiN_x : H$ layers decreases exponentially when the samples are exposed to a constant temperature of 700 °C for a few minutes. b) hydrogen effusion spectra of identical samples at constant heating rate $\beta$ of 20 °C/min. . . . .   | 30 |
| 5.7  | The partial pressure of effused hydrogen decreased exponentially when the samples are exposed to a constant temperature of 700 °C for a few minutes. The time integral of normalized partial pressure of effused hydrogen $P_{H_2}$ at constant temperature is proportional to the temperature integral of normalized $P_{H_2}$ at constant heating rate, shown by gray areas under exponential fits and the insert effusion spectra. . . . . | 31 |
| 5.8  | Flow chart of the experimental and the characterization procedure. . . . .  | 32 |
| 5.9  | Normalized partial pressure of effused hydrogen from $a - Si_x : H$ film deposited at various substrate temperatures $T_S$ of 100 °C to 400 °C as a function of annealing temperature $T_A$ [67]. The samples are divided into two groups (I and II) according to their appearance: Group I includes samples A1 and A2 without a sharp peak and Group II includes samples A3-A6 with a sharp peak, see section 5.5. . . . .                   | 34 |
| 5.10 | Comparison of integrated area under the hydrogen spectra measured by effusion mass spectroscopy with hydrogen concentration measured by NRA as a reference measurement. . . . .   | 35 |
| 5.11 | The spike of hydrogen effusion as a function of a) substrate temperature $T_S$ and b) annealing temperature $T_A$ [67]. The dash lines are a guide for the eyes. . . . .  | 37 |
| 5.12 | Light microscope images of sample's surfaces acquired a) as-deposited (left column) and b) after effusion measurement (right column) of $a - Si : H$ films A1 – A6 deposited at various substrate temperatures from 100 °C to 400 °C, respectively. The green box shows group I with samples A1 and A2 and the red box group II with samples A3...A6. . . . .   | 38 |
| 5.13 | A cross-sectional view of the sample A1 deposited at substrate temperature $T_S$ of 100 °C as deposited obtained from secondary electron microscopy SEM. . . . .  | 39 |
| 5.14 | Gaussian fit of the hydrogen evolution spectra of a) sample A2 from group 1 and b) sample A4 from group 2 [67]. . . . .   | 40 |
| 5.15 | The visual model of a sharp release of hydrogen due to the excessive pressure inside interface bubbles in a film deposited at high substrate temperature $T_S > 200$ °C which leads to the film damage [67]. . . . .  | 41 |
| 6.1  | Step by step experimental flow chart of design of experiment (DoE). . . . .   | 44 |
| 6.2  | Influence of five adjustable PECVD deposition factors on the hydrogen bond densities and the passivation quality of $a - SiNx : H$ layers. . . . .  | 46 |
| 6.3  | a) Refractive index $n$ and calculated $Si/N$ as a function of gas flow ratio $R$ used during deposition, b) optical band gap $E_g$ of $a - SiNx : H$ films vs. $R$ . The lines connecting points are a guide to the eyes. . . . .  | 47 |

|      |  |    |
|------|--|----|
| 6.4  | FT-IR absorption spectrum of polished FZ silicon wafers deposited by $SiN_x : H$ at various gas flow ratios $R$ a) as-deposited b) after firing process. . . . .   | 48 |
| 6.5  | [Si-H] bonds in stretching vibration modes obtained from FTIR measurement performed on polished FZ Si wafers deposited by $a - SiN_x : H$ at various gas flow ratios $R$ a) as-deposited b) after firing process. . . . .  | 49 |
| 6.6  | Light intensity dependent effective carrier lifetime of different $SiN_x : H$ layers deposited on planar FZ-Si wafers with various gas flow ratios $R$ a) as deposited b) after firing process. . . . .  | 49 |
| 6.7  | Partial pressure of effused $H_2$ gas molecules from $SiN_x : H$ films deposited at various gas flow ratios $R$ normalized to the film volume as a function of annealing temperature. . . . .  | 50 |
| 6.8  | a) Refractive index $n$ and calculated $Si/N$ as a function of substrate temperature $T_S$ during deposition, b) optical band gap $E_g$ of $SiN_x : H$ films vs. $T_S$ . The lines connecting points are a guide to the eyes. . . . .                                      | 51 |
| 6.9  | IR absorption peak of Si-N stretching mode obtained from FTIR measurement performed on polished FZ-Si wafers deposited by $SiN_x : H$ at various substrate temperatures $T_S$ as-deposited and after firing process. . . . .   | 52 |
| 6.10 | IR absorption peak of [Si-H] and [N-H] stretching mode obtained from FTIR measurement performed on polished FZ-Si wafers deposited by $a - SiN : H$ at various substrate temperatures $T_S$ as-deposited (straight lines) and after firing process (dashed lines). . . . . | 52 |
| 6.11 | Effective minority carrier lifetime of planar FZ-Si wafers deposited by $a - SiN_x : H$ films at various substrate temperatures $T_S$ a) as-deposited layers b) after firing process. . . . .  | 53 |
| 6.12 | Partial pressure of effused $H_2$ gas molecules from the $SiN_x : H$ films deposited at various substrate temperatures $T_S$ normalized to film volume as a function of annealing temperature. . . . .   | 54 |
| 6.13 | The influence of a) the gas flow ratio $R$ (at $T_S = 400$ °C) and b) the substrate temperature $T_S$ (with $R = 0.5$ ) during the deposition on the optical and the electrical properties of the PECVD-deposited $SiN_x : H$ passivation layers. . . . .                  | 55 |
| 6.14 | Three mechanisms of hydrogen effusion are observed depending on their film stoichiometry related to $Si/N$ ratio. . . . .  | 60 |
| 6.15 | a) The height and b) position of two hydrogen effusion peaks ( $LT_A$ and $HT_A$ ) as a function of substrate temperature used during film deposition of $SiN_x : H$ . Lines are guide for the eyes. . . . .   | 62 |
| 6.16 | Total amount of hydrogen ( $N_{H_2}$ ) diffused out of the $SiN_x : H$ layers deposited at a) various gas flow ratios ( $R$ ) and b) various substrate temperatures ( $T_S$ ). . . . .   | 63 |

|      |   |    |
|------|---|----|
| 6.17 | The film properties of PECVD-deposited $SiN_x : H$ are categorised into three main groups depending on the $Si/N$ ratio with different H-effusion mechanisms. These three groups are highlighted by different colours. The dependence of the $Si/N$ values on the gas flow ratio $R$ is shown in a), and the change in hydrogen bond density of the Si-H and N-H bonds as a function of the $Si/N$ values is plotted in b). . . . .   | 64 |
| 6.18 | Comparison the $Si/N$ values determined by X-ray photoelectron spectroscopy with Dauwe model [24] using the refractive index of the $SiN_x : H$ films (equation 6.2). . . . .   | 66 |
| 6.19 | a) schematic of MIS device ( $Al/SiN_x : H/c - Si$ ) prepared for C-V characteristics and b) the band diagram of MIS structure when a voltage ( $V_g$ ) is applied. . . . .   | 66 |
| 6.20 | C-V characteristics for the three $SiN_x : H$ groups measured in forward-bias sweep (full lines) and reverse-bias sweep (dashed lines). The measurement frequency is 1 MHz and the voltage sweep interval is 15 mV. . . . .   | 67 |
| 6.21 | Schematic model of the hydrogen transport mechanisms during annealing for N-rich, medium SiN and Si-rich films, with various compositions ( $Si/N$ ratios). Reduction of $Si/N$ increases the probability of hydrogen bonds with higher binding energies ( $E_b$ ) which postpone the effusion/diffusion of hydrogen to higher temperatures (larger $HT_A$ peak in effusion spectra). An example of densification due to annealing is illustrated in low density Si-rich layer. <sup>(1)</sup> $Si_3$ -Si-H configuration can be found at the interface of $c - Si/SiN_x : H$ . . . . . | 70 |
| 6.22 | a) Schematic of the layer stacks of three classes of silicon nitrides, the Si-rich, the medium (Si~N) and the N-rich SiN layer deposited on both sides of the c-Si wafer. . . . .   | 73 |
| 6.23 | Cross sectional SEM image of the layers stack of $SiN_x : H$ deposited on the silicon wafer. . . . .  | 74 |
| 6.24 | Partial pressure of molecular hydrogen effused from different $SiN_x : H$ layers as well as the layers stack normalized to the film volumes as a function of annealing temperature, the firing temperature of $\sim 800$ °C is shown by a dashed line. . . . .  | 75 |
| 6.25 | Absorption spectra obtained from the FTIR spectroscopy for the silicon wafers deposited with different layers of $SiN_x : H$ and the layers stack after deposition and after the firing. . . . .  | 76 |
| 6.26 | Effective charge carrier lifetime of $SiN_x : H$ layers stack deposited on Si wafers with various gas flow ratios $R$ a) after deposition deposited and b) after the firing. . . . .  | 77 |
| 6.27 | The experimental flow chart for sample preparation. [106]. . . . .  | 80 |
| 6.28 | FTIR data performed on polished FZ Si samples passivated with different thickness of $SiN_x : H$ , before and after firing at a set peak firing temperature of 935 °C. The inset shows the data on a different scale. [105]. . . . .  | 81 |
| 6.29 | a) Normalized defect density (NDD) test of mc-Si samples deposited by multiple $SiN_x : H$ thicknesses as a function of cumulative laser time under accelerated degradation condition of $26.6 \text{ kW/m}^2$ at 130 °C [105] b) Hydrogen effusion spectra of samples passivated with $SiN_x : H$ of various thicknesses. . . . .  | 82 |



|  |     |
|--|-----|
| 6.30 a) NDD evolution of mc-Si sample that are passivated with various $SiN_x : H$ and $AlO_x$ stacks under illumination intensity of $38 \text{ kW/m}^2$ at $130 \text{ }^\circ\text{C}$ [105] b) Partial pressure of molecular hydrogen $H_2$ effused from set 2 of samples. . . . .   | 82  |
| 6.31 Maximum normalized defect densities ( $NDD_{max}$ ) of the samples passivated with multiple thicknesses of $SiN_x : H$ layers vs. integrated area under the effusion spectra up to temperature of $\sim 850 \text{ }^\circ\text{C}$ . The line is a guide to the eyes. . . . .  | 84  |
| 6.32 $NDD_{max}$ of sample passivated with variable $SiN_x : H$ and $AlO_x : H$ stacks as a function of integrated area under the effusion spectra up to temperature of $\sim 850 \text{ }^\circ\text{C}$ . . . . .  | 85  |
| 7.1 Cross-section image of plasma-textured black silicon after 10 min ICP+CCP etching process. . . . .   | 90  |
| 7.2 SEM cross-section view images of plasma-textured black silicon deposited by $SiN_x : H$ layer using gas flow ratio $R0.5$ . . . . .  | 91  |
| 7.3 Effective charge carrier lifetime of textured samples deposited with $SiN_x : H$ with various gas flow ratios $R$ a) before and b) after the firing process. . . . .   | 91  |
| 7.4 Hydrogen effusion a) on planar and b) black Si samples deposited with the $SiN_x : H$ layers with various gas flow ratio $R$ . . . . .   | 92  |
| 7.5 Effective charge carrier lifetime of textured samples deposited with $SiN_x : H$ with various deposition temperatures $T_S$ a) before and b) after the firing process. . . . .   | 93  |
| 7.6 Hydrogen effusion from the $SiN_x : H$ layers deposited with various substrate temperature ( $T_S$ ) a) on planar FZ-Si and b) on the plasma textured black Si wafers. . . . .   | 94  |
| 7.7 Light intensity dependent effective carrier lifetime of $SiN_x : H$ stack deposited on plasma textured FZ-Si wafers with various gas flow ratios $R$ a) as deposited b) after firing process. . . . .  | 95  |
| 7.8 Surface impurities and defects are formed during plasma texturing process at the surface or beneath the surface and suppress the passivation quality of $SiN_x : H$ layers in comparison with the planar samples [40]. The $SiN_x : H$ coated planar- and textured-Si sample are shown to visualize the surface enhancement as well as the increased surface defects due to the plasma texturing. . . . .                              | 96  |
| 7.9 $\Delta\tau$ is the percent reduction of effective charge carrier lifetime in the black silicon compared to the planar samples as a function of various gas flow ratios $R$ and substrate temperatures $T_S$ used during the $SiN_x : H$ deposition. Although identical $SiN_x : H$ passivation films are deposited on both planar- and plasma textured- Si wafers, the minority carrier lifetime is significantly difference. . . . . | 98  |
| A.1 The effect of deposition factors and their interactions is presented in Pareto diagram for [Si-H] bond densities in $SiN_x : H$ films a) as deposited and b) after industrial firing process RTA. . . . .  | 106 |

|     |  |     |
|-----|--|-----|
| A.2 | The effect of deposition factors and their interactions is presented in Pareto diagram for [N-H] bond densities in $SiN_x : H$ films a) as deposited and b) after industrial firing process RTA. . . . .   | 106 |
| A.3 | The effect of deposition factors and their interactions is presented in Pareto diagram for measured effective carrier lifetime performed on polished FZ-Si wafers deposited by $a - SiN : H$ films a) as deposited and b) after industrial firing process RTA. . . . . | 107 |
| A.4 | Surface plot of Si-N bond density vs. deposition temperature and gas flow ratio for $SiN_x : H$ coated FZ-Si wafers a) as deposited and b) after the firing process (RTA) at 800 °C for about 1 min. . . . .   | 108 |
| A.5 | Surface plot of Si-H bond density vs. deposition temperature and gas flow ratio for $a - SiNx : H$ coated FZ-Si wafers a) as deposited and b) after the firing process (RTA) at 800 °C for about 1 min. . . . .  | 108 |
| A.6 | Surface plot of [N-H] bond density vs. deposition temperature and gas flow ratio for $SiN_x : H$ coated FZ-Si wafers a) as deposited and b) after the firing process (RTA) at 800 °C for about 1 min. . . . .  | 109 |
| A.7 | Surface plot of effective minority carrier lifetime $\tau$ vs. deposition temperature and gas flow ratio for $SiN_x : H$ coated FZ-Si wafers a) as deposited and b) after the firing process (RTA) at 800 °C for about 1 min. . . . .                                  | 110 |

# List of Tables

|     |  |    |
|-----|--|----|
| 5.1 | The time integral of normalized partial pressure of effused hydrogen $P_{H_2}$ at constant temperature and the temperature integral of normalized $P_{H_2}$ at constant heating rate decrease proportionally. The values are shown in arbitrary units. . . . . | 32 |
| 5.2 | The film thicknesses $d$ and NRA measured hydrogen concentration $C_H$ of PECVD deposited $a - Si : H$ films on $c - Si$ wafers at various substrate temperatures $T_S$ [66]. . . . .  | 33 |
| 5.3 | Mean value and standard deviation (SD) of the integrated area under the hydrogen effusion peaks $A_{eff}$ , peak position of $LT$ , $HT$ and sharp peaks $SP$ of $a_{Si} : H$ layers deposited at various substrate temperatures $T_S$ . . . . .               | 33 |
| 5.4 | List of some widely used characterization methods for hydrogen detection. . . . .  | 35 |
| 5.5 | Peak position and normalized integrated effusion intensity for the Gaussian components of effusion spectra for samples A2 and A4. . . . .  | 40 |
| 6.1 | List of deposition factors used for PECVD deposited $a - SiN_x : H$ films with two-level full factorial design including the center points. . . . .  | 45 |
| 6.2 | A list of measured and calculated optical properties of a-SiN <sub>x</sub> :H films deposited with various gas flow ratios $R$ on polished FZ-Si wafers. . . . .   | 46 |
| 6.3 | The effective carrier lifetime measured at a minority carrier density of $10^{15} cm^{-3}$ for polished FZ-Si wafers deposited by $SiN_x : H$ films with various gas flow ratios $R$ . . . . .   | 48 |
| 6.4 | A list of optical properties of $SiN_x : H$ films deposited with various substrate temperatures $T_S$ . . . . .  | 51 |
| 6.5 | Effective minority carrier lifetime obtained for SiN coated planar FZ-Si with various substrate temperature $T_S$ as deposited ( $\tau_{as\ deposited}$ ) and after firing ( $\tau_{Fired}$ ). . . . .   | 53 |
| 6.6 | Three different mechanisms of hydrogen release related to the film structure of $SiN_x : H$ are introduced. The possible reactions for the first ( $LT_A$ ) and second ( $HT_A$ ) peaks of effusion are proposed. . . . .                                      | 61 |
| 6.7 | The properties of Al and c-Si wafers applied for the calculation of positive fixed charges in $SiN_x : H$ films. . . . .   | 67 |
| 6.8 | A list of quantities measured by a high frequency C-V measurements of three different type of $a - SiN_x : H$ films. . . . .   | 68 |

|      |   |    |
|------|---|----|
| 6.9  | The film thicknesses $d$ , deposition rate $G$ and deposition variables, gas flow ratio ( $R$ ) and deposition time, used during deposition of $SiN_x : H$ layers. . . . .  | 74 |
| 6.10 | fraction of the molecular hydrogen effused at the annealing temperature between the room temperature (RT) and the firing temperature (800 °C) from the different $SiN_x : H$ layers including the layers stack. . . . .   | 75 |
| 6.11 | Effective charge carrier lifetime measured at minority carrier density of $10^{15}cm^{-3}$ for Si wafers deposited by different layers $SiN_x : H$ and the layers stack with various gas flow ratios $R$ a) after deposition and b) after the firing. . . . .     | 76 |
| 6.12 | The relative difference of the hydrogen concentration in the the $SiN_x : H$ layers and stack calculated from the FTIR spectra and from the hydrogen effusion measurement. . . . .  | 77 |
| 7.1  | Effective minority charge carrier lifetime $\tau$ obtained for SiN coated black Si samples with various gas flow ratio $R$ as deposited and after firing. . . . .   | 92 |
| 7.2  | Effective charge carrier lifetime measured at the minority charge carrier density of $10^{15} cm^{-3}$ for plasma textured Si samples deposited with $SiN_x : H$ layers with various substrate temperature $T_S$ before and after firing. . . . .                 | 93 |
| 7.3  | Effective charge carrier lifetime measured at the minority charge carrier density of $10^{15}cm^{-3}$ for black Si wafers deposited by single layers and a stack of $SiN_x : H$ films with various gas flow ratios $R$ a) before and b) after the firing. . . . . | 95 |

# Bibliography

- [1] S. Jafari, J. Hirsch, D. Lausch, M. John, N. Bernhard, and S. Meyer, "Composition limited hydrogen effusion rate of a-sinx: H passivation stack," in *AIP Conference Proceedings*, vol. 2147, p. 050004, AIP Publishing LLC, 2019.
- [2] S. Jafari, U. Varshney, B. Hoex, S. Meyer, and D. Lausch, "Understanding light-and elevated temperature-induced degradation in silicon wafers using hydrogen effusion mass spectroscopy," *IEEE Journal of Photovoltaics*, 2021.
- [3] "Climate change, <https://www.un.org/en/sections/issues-depth/climate-change/>."
- [4] D. H. Wirth and I. Fraunhofer, "Aktuelle fakten zur photovoltaik in deutschland. 2020."
- [5] R. Ohl, "Light-sensitive electric device'us patent no. 2, 402, 622; light-sensitive device including silicon," *US Patent*, vol. 2, 1941.
- [6] K. Yamamoto, K. Yoshikawa, H. Uzu, and D. Adachi, "High-efficiency heterojunction crystalline si solar cells," *Japanese Journal of Applied Physics*, vol. 57, no. 8S3, p. 08RB20, 2018.
- [7] "<https://www.irena.org/publications/2020/jun/renewable-power-costs-in-2019/>"
- [8] A. G. Aberle, "Overview on sin surface passivation of crystalline silicon solar cells," *Solar energy materials and solar cells*, vol. 65, no. 1-4, pp. 239–248, 2001.
- [9] B. Sopori, Y. Zhang, R. Reedy, K. Jones, Y. Yan, M. Al-Jassim, B. Bathey, and J. Kalejs, "A comprehensive model of hydrogen transport into a solar cell during silicon nitride processing for fire-through metallization," in *Conference Record of the Thirty-first IEEE Photovoltaic Specialists Conference, 2005.*, pp. 1039–1042, IEEE, 2005.
- [10] T. Lauinger, J. Moschner, A. G. Aberle, and R. Hezel, "Optimization and characterization of remote plasma-enhanced chemical vapor deposition silicon nitride for the passivation of p-type crystalline silicon surfaces," *Journal of Vacuum Science & Technology A: Vacuum, Surfaces, and Films*, vol. 16, no. 2, pp. 530–543, 1998.
- [11] M. J. Kerr and A. Cuevas, "Recombination at the interface between silicon and stoichiometric plasma silicon nitride," *Semiconductor science and technology*, vol. 17, no. 2, p. 166, 2002.

- [12] A. Van Wieringen and N. Warmoltz, "On the permeation of hydrogen and helium in single crystal silicon and germanium at elevated temperatures," *physica*, vol. 22, no. 6-12, pp. 849–865, 1956.
- [13] M. Sheoran, D. S. Kim, A. Rohatgi, H. Dekkers, G. Beaucarne, M. Young, and S. Asher, "Hydrogen diffusion in silicon from pecvd silicon nitride," in *2008 33rd IEEE Photovoltaic Specialists Conference*, pp. 1–4, IEEE, 2008.
- [14] A. Luque and S. Hegedus, *Photovoltaic science and engineering*. Wiley Online Library, 2003.
- [15] W. Shockley, "On the surface states associated with a periodic potential," *Physical review*, vol. 56, no. 4, p. 317, 1939.
- [16] R. B. Girisch, R. P. Mertens, and R. F. De Keersmaecker, "Determination of si-sio/sub 2/interface recombination parameters using a gate-controlled point-junction diode under illumination," *IEEE Transactions on Electron Devices*, vol. 35, no. 2, pp. 203–222, 1988.
- [17] S. Glunz, R. Preu, and D. Biro, "Crystalline silicon solar cells: state-of-the-art and future developments," *Comprehensive renewable energy*, vol. 1, pp. 353–387, 2012.
- [18] R. Hezel and R. Schörner, "Plasma si nitride—a promising dielectric to achieve high-quality silicon mis/il solar cells," *Journal of Applied Physics*, vol. 52, no. 4, pp. 3076–3079, 1981.
- [19] J. Schmidt and M. Kerr, "Highest-quality surface passivation of low-resistivity p-type silicon using stoichiometric pecvd silicon nitride," *Solar Energy Materials and Solar Cells*, vol. 65, no. 1-4, pp. 585–591, 2001.
- [20] B. J. Hallam, S. R. Wenham, P. G. Hamer, M. D. Abbott, A. Sugianto, C. E. Chan, A. M. Wenham, M. G. Eadie, and G. Xu, "Hydrogen passivation of bo defects in czochralski silicon," *Energy Procedia*, vol. 38, pp. 561–570, 2013.
- [21] B. Sopori, Y. Zhang, R. Reedy, K. Jones, Y. Yan, M. Al-Jassim, J. Kalejs, and B. Bathey, "On the mechanism of hydrogen diffusion in si solar cells using pecvd sin: H," *MRS Online Proceedings Library*, vol. 813, no. 1, pp. 621–627, 2004.
- [22] A. Herguth, G. Schubert, M. Kaes, and G. Hahn, "A new approach to prevent the negative impact of the metastable defect in boron doped cz silicon solar cells," in *2006 IEEE 4th World Conference on Photovoltaic Energy Conference*, vol. 1, pp. 940–943, IEEE, 2006.
- [23] V. Verlaan, A. Verkerk, W. Arnoldbik, C. van der Werf, R. Bakker, Z. Houweling, I. Romijn, D. Borsa, A. Weeber, S. Luxembourg, *et al.*, "The effect of composition on the bond structure and refractive index of silicon nitride deposited by hwcvd and pecvd," *Thin Solid Films*, vol. 517, no. 12, pp. 3499–3502, 2009.

- [24] S. Dauwe, L. Mittelstadt, A. Metz, J. Schmidt, and R. Hezel, "Low-temperature rear surface passivation schemes for  $\geq$  20% efficient silicon solar cells," in *3rd World Conference on Photovoltaic Energy Conversion, 2003. Proceedings of*, vol. 2, pp. 1395–1398, IEEE, 2003.
- [25] H. Mäckel and R. Lüdemann, "Detailed study of the composition of hydrogenated silicon layers for high-quality silicon surface passivation," *Journal of applied physics*, vol. 92, no. 5, pp. 2602–2609, 2002.
- [26] J. Schmidt and A. G. Aberle, "Carrier recombination at silicon–silicon nitride interfaces fabricated by plasma-enhanced chemical vapor deposition," *Journal of Applied Physics*, vol. 85, no. 7, pp. 3626–3633, 1999.
- [27] V. A. Singh, C. Weigel, J. Corbett, and L. Roth, "Vibrational and electronic structure of hydrogen-related defects in silicon calculated by the extended hückel theory," *physica status solidi (b)*, vol. 81, no. 2, pp. 637–646, 1977.
- [28] S. Pearton, J. Corbett, and T. Shi, "Hydrogen in crystalline semiconductors," *Applied Physics A*, vol. 43, no. 3, pp. 153–195, 1987.
- [29] F. Giorgis, F. Giuliani, C. Pirri, E. Tresso, C. Summonte, R. Rizzoli, R. Galloni, A. Desalvo, and P. Rava, "Optical, structural and electrical properties of device-quality hydrogenated amorphous silicon-nitrogen films deposited by plasma-enhanced chemical vapour deposition," *Philosophical Magazine B*, vol. 77, no. 4, pp. 925–944, 1998.
- [30] C. Herring, N. Johnson, and C. G. Van de Walle, "Energy levels of isolated interstitial hydrogen in silicon," *Physical Review B*, vol. 64, no. 12, p. 125209, 2001.
- [31] M. Gläser and D. Lausch, "Towards a quantitative model for boron regeneration by means of charge state control of hydrogen," *Energy Procedia*, vol. 77, pp. 592–598, 2015.
- [32] H. Reiss, "Theory of the ionization of hydrogen and lithium in silicon and germanium," *The Journal of Chemical Physics*, vol. 25, no. 4, pp. 681–686, 1956.
- [33] S. J. Pearton and J. W. Lee, "Hydrogen in wide bandgap semiconductors," in *Processing of wide band gap semiconductors*, pp. 429–505, Elsevier, 2000.
- [34] K. Fujiwara, "Surface states and reactivity of hydrogen chemisorption on thermally cleaned silicon (111) surfaces: New evidence for rough-surface models," *Physical Review B*, vol. 24, no. 4, p. 2240, 1981.
- [35] M. Knotek, G. Loubriel, R. Stulen, C. Parks, B. Koel, and Z. Hussain, "Hydrogen surface segregation on silicon (111) by photon-stimulated desorption at the silicon k edge," *Physical Review B*, vol. 26, no. 4, p. 2292, 1982.
- [36] M. Bachman, "Rca-1 silicon wafer cleaning," *INRF application note Engineering of Microworld at the University of California. Irvine*, 1999.

- [37] H. Sterling and R. Swann, "Chemical vapour deposition promoted by rf discharge," *Solid-State Electronics*, vol. 8, no. 8, pp. 653–654, 1965.
- [38] M. A. Green, "Solar cells: operating principles, technology, and system applications," *Englewood Cliffs*, 1982.
- [39] H. Jansen, M. de Boer, R. Legtenberg, and M. Elwenspoek, "The black silicon method: a universal method for determining the parameter setting of a fluorine-based reactive ion etcher in deep silicon trench etching with profile control," *Journal of Micromechanics and Microengineering*, vol. 5, no. 2, p. 115, 1995.
- [40] M. Gaudig, "Physikalische mechanismen der bildung von schwarzem silizium bei maskenfreiem plasmaätzen," 2018.
- [41] U. Varshney, *Examining the influence of surface dielectric layers and bulk properties in light- and elevated temperature-induced degradation in crystalline silicon*. PhD thesis, Photovoltaics Renewable Energy Engineering, Faculty of Engineering, UNSW, 2021.
- [42] M. Neubert, *Die Rolle des Sauerstoffanteils in Titandioxid bei Tantal-Dotierung zur Verwendung als transparentes leitfähiges Oxid*. PhD thesis, Universitätsbibliothek Chemnitz, 2016.
- [43] E. Bustarret, M. Bensouda, M. Habrard, J. Bruyere, S. Poulin, and S. Gujrathi, "Configurational statistics in a-si x n y h z alloys: A quantitative bonding analysis," *Physical Review B*, vol. 38, no. 12, p. 8171, 1988.
- [44] W. Lanford and M. Rand, "The hydrogen content of plasma-deposited silicon nitride," *Journal of applied physics*, vol. 49, no. 4, pp. 2473–2477, 1978.
- [45] Z. Yin and F. Smith, "Optical dielectric function and infrared absorption of hydrogenated amorphous silicon nitride films: Experimental results and effective-medium-approximation analysis," *Physical Review B*, vol. 42, no. 6, p. 3666, 1990.
- [46] G. Jellison Jr and F. Modine, "Parameterization of the optical functions of amorphous materials in the interband region," *Applied Physics Letters*, vol. 69, no. 3, pp. 371–373, 1996.
- [47] H. Nagel, C. Berge, and A. G. Aberle, "Generalized analysis of quasi-steady-state and quasi-transient measurements of carrier lifetimes in semiconductors," *Journal of Applied Physics*, vol. 86, no. 11, pp. 6218–6221, 1999.
- [48] D. K. Schroder, "Surface voltage and surface photovoltage: history, theory and applications," *Measurement Science and Technology*, vol. 12, no. 3, p. R16, 2001.
- [49] K. Instruments, "" model 4200-scs semiconductor characterization system reference manual," tech. rep., 4200-901-01 Rev. Q/April 2016, 2016.



- [50] L. Reimer, "Scanning electron microscopy: physics of image formation and microanalysis," 2000.
- [51] R. Hezel and K. Jaeger, "Low-temperature surface passivation of silicon for solar cells," *Journal of the Electrochemical Society*, vol. 136, no. 2, p. 518, 1989.
- [52] S. Wilking, A. Herguth, and G. Hahn, "Influence of hydrogenated passivation layers on the regeneration of boron-oxygen related defects," *Energy Procedia*, vol. 38, pp. 642–648, 2013.
- [53] N. Nampalli, B. Hallam, C. Chan, M. Abbott, and S. Wenham, "Role of hydrogen in the permanent passivation of boron-oxygen defects in czochralski silicon," in *2015 IEEE 42nd Photovoltaic Specialist Conference (PVSC)*, pp. 1–3, IEEE, 2015.
- [54] A. Triska, D. Dennison, and H. Fritzsche, "Hydrogen content in amorphous-ge and si prepared by rf decomposition of  $geH_4$  and  $siH_4$ ," in *Bulletin of the American Physical Society*, vol. 20, pp. 392–392, AMER INST PHYSICS CIRCULATION FULFILLMENT DIV, 500 SUNNYSIDE BLVD, WOODBURY . . . , 1975.
- [55] P. Redhead, "Thermal desorption of gases," *Vacuum*, vol. 12, no. 4, pp. 203–211, 1962.
- [56] W. Beyer and H. Wagner, "Hydrogen evolution from plasma-deposited amorphous silicon films," *Le Journal de Physique Colloques*, vol. 42, no. C4, pp. C4–783, 1981.
- [57] W. Beyer and F. Einsele, "Hydrogen effusion experiments," *Advanced Characterization Techniques for Thin Film Solar Cells*, vol. 2, pp. 569–595, 2016.
- [58] W. Beyer and H. Mell, "Composition and thermal stability of glow-discharge a-si: C: H and a-si: N: H alloys," in *Disordered Semiconductors*, pp. 641–658, Springer, 1987.
- [59] D. Murley, I. French, S. Deane, and R. Gibson, "The effect of hydrogen dilution on the aminosilane plasma regime used to deposit nitrogen-rich amorphous silicon nitride," *Journal of non-crystalline solids*, vol. 198, pp. 1058–1062, 1996.
- [60] W. Beyer and H. Dekkers, "Microstructure characterization of amorphous silicon-nitride films by effusion measurements," *MRS Online Proceedings Library Archive*, vol. 910, 2006.
- [61] H. Lüth, *Surfaces and interfaces of solid materials*. Springer Science & Business Media, 2013.
- [62] A. Chambers, *Basic vacuum technology*. CRC Press, 1998.
- [63] W. Beyer and H. Wagner, "Determination of the hydrogen diffusion coefficient in hydrogenated amorphous silicon from hydrogen effusion experiments," *Journal of Applied Physics*, vol. 53, no. 12, pp. 8745–8750, 1982.
- [64] J. Robertson, "Defects and hydrogen in amorphous silicon nitride," *Philosophical magazine B*, vol. 69, no. 2, pp. 307–326, 1994.

- [65] M. Wilde and K. Fukutani, "Hydrogen detection near surfaces and shallow interfaces with resonant nuclear reaction analysis," *Surface science reports*, vol. 69, no. 4, pp. 196–295, 2014.
- [66] J. Steffens, H.-W. Becker, S. Gerke, S. Joos, G. Hahn, and B. Terheiden, "Replacing nra by fast gd-oes measurements as input to a model based prediction of hydrogen diffusion in a-si," *Energy Procedia*, vol. 124, pp. 180–187, 2017.
- [67] S. Jafari, J. Steffens, M. Wendt, B. Terheiden, S. Meyer, and D. Lausch, "Occurrence of sharp hydrogen effusion peaks of hydrogenated amorphous silicon film and its connection to void structure," *physica status solidi (b)*, 2020.
- [68] I. Jonak-Auer, R. Meisels, and F. Kuchar, "Determination of the hydrogen concentration of silicon nitride layers by fourier transform infrared spectroscopy," *Infrared physics & technology*, vol. 38, no. 4, pp. 223–226, 1997.
- [69] C. Magee and E. Botnick, "Hydrogen depth profiling using sims—problems and their solutions," *Journal of Vacuum Science and Technology*, vol. 19, no. 1, pp. 47–52, 1981.
- [70] J.-F. Lelièvre, E. Fourmond, A. Kaminski, O. Palais, D. Ballutaud, and M. Lemitte, "Study of the composition of hydrogenated silicon nitride sinx: H for efficient surface and bulk passivation of silicon," *Solar Energy Materials and Solar Cells*, vol. 93, no. 8, pp. 1281–1289, 2009.
- [71] M. Brodsky, M. Frisch, J. Ziegler, and W. Lanford, "Quantitative analysis of hydrogen in glow discharge amorphous silicon," *Applied Physics Letters*, vol. 30, no. 11, pp. 561–563, 1977.
- [72] W. Lanford, "Analysis for hydrogen by nuclear reaction and energy recoil detection," *Nuclear Instruments and Methods in Physics Research Section B: Beam Interactions with Materials and Atoms*, vol. 66, no. 1-2, pp. 65–82, 1992.
- [73] F. Pászti, E. Kótai, G. Mezey, A. Manuaba, L. Pócs, D. Hildebrandt, and H. Strusny, "Hydrogen and deuterium measurements by elastic recoil detection using alpha particles," *Nuclear Instruments and Methods in Physics Research Section B: Beam Interactions with Materials and Atoms*, vol. 15, no. 1-6, pp. 486–491, 1986.
- [74] J. Steffens, J. Rinder, G. Hahn, and B. Terheiden, "Correlation between the optical bandgap and the monohydride bond density of hydrogenated amorphous silicon," *Journal of Non-Crystalline Solids: X*, vol. 5, p. 100044, 2020.
- [75] H. Shanks and L. Ley, "Formation of pin holes in hydrogenated amorphous silicon at high temperatures and the yield strength of a-si: H," *Journal of Applied Physics*, vol. 52, no. 2, pp. 811–813, 1981.
- [76] A. Smets, W. Kessels, and M. Van de Sanden, "Vacancies and voids in hydrogenated amorphous silicon," *Applied physics letters*, vol. 82, no. 10, pp. 1547–1549, 2003.

- [77] D. Biegelsen, R. A. Street, C. C. Tsai, and J. C. Knights, "Hydrogen evolution and defect creation in amorphous si: H alloys," *Physical Review B*, vol. 20, no. 12, p. 4839, 1979.
- [78] J. Melskens, A. H. Smets, M. Schouten, S. W. Eijt, H. Schut, and M. Zeman, "New insights in the nanostructure and defect states of hydrogenated amorphous silicon obtained by annealing," in *2012 IEEE 38th Photovoltaic Specialists Conference (PVSC) PART 2*, pp. 1–8, IEEE, 2012.
- [79] W. Beyer, H. Wagner, J. Chevallier, and K. Reichelt, "Comparative study of hydrogen evolution from amorphous hydrogenated silicon films," *Thin Solid Films*, vol. 90, no. 2, pp. 145–152, 1982.
- [80] B. Macco, J. Melskens, N. J. Podraza, K. Arts, C. Pugh, O. Thomas, and W. M. Kessels, "Correlating the silicon surface passivation to the nanostructure of low-temperature a-si: H after rapid thermal annealing," *Journal of Applied Physics*, vol. 122, no. 3, p. 035302, 2017.
- [81] W. Beyer and H. Wagner, "The role of hydrogen in a-si: H—results of evolution and annealing studies," *Journal of Non-Crystalline Solids*, vol. 59, pp. 161–168, 1983.
- [82] A. Matsuda, K. Nomoto, Y. Takeuchi, A. Suzuki, A. Yuuki, and J. Perrin, "Temperature dependence of the sticking and loss probabilities of silyl radicals on hydrogenated amorphous silicon," *Surface Science*, vol. 227, no. 1-2, pp. 50–56, 1990.
- [83] A. Smets and M. Van De Sanden, "Relation of the si h stretching frequency to the nanostructural si h bulk environment," *Physical Review B*, vol. 76, no. 7, p. 073202, 2007.
- [84] J. Tauc, *Amorphous and liquid semiconductors*. Springer Science & Business Media, 2012.
- [85] G. Scardera, T. Puzzer, G. Conibeer, and M. Green, "Fourier transform infrared spectroscopy of annealed silicon-rich silicon nitride thin films," *Journal of Applied Physics*, vol. 104, no. 10, p. 104310, 2008.
- [86] A. Sinha and E. Lugujo, "Lorentz-lorenz correlation for reactively plasma deposited si-n films," *Applied Physics Letters*, vol. 32, no. 4, pp. 245–246, 1978.
- [87] D. L. Smith, A. S. Alimonda, C.-C. Chen, S. E. Ready, and B. Wacker, "Mechanism of  $\text{Si}_x\text{H}_y$  deposition from  $\text{NH}_3\text{-SiH}_4$  plasma," *Journal of the Electrochemical Society*, vol. 137, no. 2, p. 614, 1990.
- [88] D. Murley, R. Gibson, B. Dunnett, A. Goodyear, and I. French, "Influence of gas residence time on the deposition of nitrogen-rich amorphous silicon nitride," *Journal of non-crystalline solids*, vol. 187, pp. 324–328, 1995.
- [89] A. Weeber, H. Rieffe, W. Sinke, and W. Soppe, "Structural and passivating properties of  $\text{Si}_x\text{H}_y$  deposited using different precursor gases," in *Proceedings of the 19th European Photovoltaic solar energy conference*, vol. 1005, pp. 7–11, 2004.

- [90] S. Rein, *Lifetime spectroscopy: a method of defect characterization in silicon for photovoltaic applications*, vol. 85. Springer Science & Business Media, 2006.
- [91] S. Gatz, F. Einsele, T. Dullweber, and R. Brendel, "Firing stability of sily/sinx surface passivation stacks for crystalline silicon solar cells," in *26th European Photovoltaic Solar Energy Conference*, pp. 1132–1136, 2011.
- [92] C. Boehme and G. Lucovsky, "Dissociation reactions of hydrogen in remote plasma-enhanced chemical-vapor-deposition silicon nitride," *Journal of Vacuum Science & Technology A: Vacuum, Surfaces, and Films*, vol. 19, no. 5, pp. 2622–2628, 2001.
- [93] W. Beyer, "Hydrogen effusion: a probe for surface desorption and diffusion," *Physica B: Condensed Matter*, vol. 170, no. 1-4, pp. 105–114, 1991.
- [94] S. De Wolf, G. Agostinelli, G. Beaucarne, and P. Vitanov, "Influence of stoichiometry of direct plasma-enhanced chemical vapor deposited sin x films and silicon substrate surface roughness on surface passivation," *Journal of Applied Physics*, vol. 97, no. 6, p. 063303, 2005.
- [95] D. K. Schroder, *Semiconductor material and device characterization*. John Wiley & Sons, 2015.
- [96] Z. Shu, *Low temperature surface passivation of crystalline silicon and its application to interdigitated back contact silicon heterojunction (ibc-shj) solar cell*. 2013.
- [97] S. Fujita and A. Sasaki, "Dangling bonds in memory-quality silicon nitride films," *Journal of the electrochemical society*, vol. 132, no. 2, p. 398, 1985.
- [98] H. Schmidt, W. Gruber, G. Borchardt, M. Bruns, M. Rudolphi, and H. Baumann, "The diffusion of ion implanted hydrogen in amorphous si<sub>3</sub>n<sub>4</sub>: H films," *Journal of Physics: Condensed Matter*, vol. 16, no. 24, p. 4233, 2004.
- [99] A. C. née Wenham, S. Wenham, R. Chen, C. Chan, D. Chen, B. Hallam, D. Payne, T. Fung, M. Kim, S. Liu, *et al.*, "Hydrogen-induced degradation," in *2018 IEEE 7th World Conference on Photovoltaic Energy Conversion (WCPEC)(A Joint Conference of 45th IEEE PVSC, 28th PVSEC & 34th EU PVSEC)*, pp. 0001–0008, IEEE, 2018.
- [100] D. Chen, P. G. Hamer, M. Kim, T. H. Fung, G. Bourret-Sicotte, S. Liu, C. E. Chan, A. Ciesla, R. Chen, M. D. Abbott, *et al.*, "Hydrogen induced degradation: A possible mechanism for light-and elevated temperature-induced degradation in n-type silicon," *Solar Energy Materials and Solar Cells*, vol. 185, pp. 174–182, 2018.
- [101] J. Schmidt, D. Bredemeier, and D. C. Walter, "On the defect physics behind light and elevated temperature-induced degradation (letid) of multicrystalline silicon solar cells," *IEEE Journal of Photovoltaics*, vol. 9, no. 6, pp. 1497–1503, 2019.

- [102] F. Fertig, R. Lantsch, A. Mohr, M. Schaper, M. Bartzsch, D. Wissen, F. Kersten, A. Mette, S. Peters, A. Eidner, *et al.*, “Mass production of p-type cz silicon solar cells approaching average stable conversion efficiencies of 22%,” *Energy Procedia*, vol. 124, pp. 338–345, 2017.
- [103] D. Chen, M. Kim, B. V. Stefani, B. J. Hallam, M. D. Abbott, C. E. Chan, R. Chen, D. N. Payne, N. Nampalli, A. Ciesla, *et al.*, “Evidence of an identical firing-activated carrier-induced defect in monocrystalline and multicrystalline silicon,” *Solar Energy Materials and Solar Cells*, vol. 172, pp. 293–300, 2017.
- [104] M. Padmanabhan, K. Jhaveri, R. Sharma, P. K. Basu, S. Raj, J. Wong, and J. Li, “Light-induced degradation and regeneration of multicrystalline silicon al-bsf and perc solar cells,” *physica status solidi (RRL)–Rapid Research Letters*, vol. 10, no. 12, pp. 874–881, 2016.
- [105] U. Varshney, M. Abbott, A. Ciesla, D. Chen, S. Liu, C. Sen, M. Kim, S. Wenham, B. Hoex, and C. Chan, “Evaluating the impact of sin x thickness on lifetime degradation in silicon,” *IEEE Journal of Photovoltaics*, vol. 9, no. 3, pp. 601–607, 2019.
- [106] U. Varshney, B. Hallam, P. Hamer, A. Ciesla, D. Chen, S. Liu, C. Sen, A. Samadi, M. Abbott, C. Chan, *et al.*, “Controlling light-and elevated-temperature-induced degradation with thin film barrier layers,” *IEEE Journal of Photovoltaics*, vol. 10, no. 1, pp. 19–27, 2019.
- [107] D. N. Payne, C. E. Chan, B. J. Hallam, B. Hoex, M. D. Abbott, S. R. Wenham, and D. M. Bagnall, “Rapid passivation of carrier-induced defects in p-type multi-crystalline silicon,” *Solar Energy Materials and Solar Cells*, vol. 158, pp. 102–106, 2016.
- [108] S. Glunz, S. Rein, J. Lee, and W. Warta, “Minority carrier lifetime degradation in boron-doped czochralski silicon,” *Journal of Applied Physics*, vol. 90, no. 5, pp. 2397–2404, 2001.
- [109] D. Abou-Ras, T. Kirchartz, and U. Rau, *Advanced characterization techniques for thin film solar cells*. John Wiley & Sons, 2016.
- [110] D. Bredemeier, D. Walter, S. Herlufsen, and J. Schmidt, “Lifetime degradation and regeneration in multicrystalline silicon under illumination at elevated temperature,” *Aip Advances*, vol. 6, no. 3, p. 035119, 2016.
- [111] D. Bredemeier, D. C. Walter, and J. Schmidt, “Possible candidates for impurities in mc-si wafers responsible for light-induced lifetime degradation and regeneration,” *Solar RRL*, vol. 2, no. 1, p. 1700159, 2018.
- [112] M. A. Jensen, A. E. Morishige, S. Chakraborty, R. Sharma, H. S. Laine, B. Lai, V. Rose, A. Youssef, E. E. Looney, S. Wieghold, *et al.*, “Solubility and diffusivity: important metrics in the search for the root cause of light-and elevated temperature-induced degradation,” *IEEE Journal of Photovoltaics*, vol. 8, no. 2, pp. 448–455, 2018.

- [113] G. Dingemans, F. Einsele, W. Beyer, M. Van de Sanden, and W. Kessels, "Influence of annealing and  $\text{Al}_2\text{O}_3$  properties on the hydrogen-induced passivation of the Si/SiO<sub>2</sub> interface," *Journal of Applied Physics*, vol. 111, no. 9, p. 093713, 2012.
- [114] G. Dingemans, B. Hoex, M. van de Sanden, W. M. Kessels, P. Engelhart, R. Seguin, and F. Einsele, "Stability of  $\text{Al}_2\text{O}_3$  and  $\text{Al}_2\text{O}_3/\text{a-Si}_x\text{H}_y$ : H stacks for surface passivation of crystalline silicon," *Journal of Applied Physics*, vol. 106, no. 11, 2009.
- [115] M. Otto, M. Algasinger, H. Branz, B. Gesemann, T. Gimpel, K. Fuchsler, T. Käsebier, S. Kontermann, S. Koynov, X. Li, *et al.*, "Black silicon photovoltaics," *Advanced optical materials*, vol. 3, no. 2, pp. 147–164, 2015.
- [116] J. Oh, H.-C. Yuan, and H. M. Branz, "An 18.2%-efficient black-silicon solar cell achieved through control of carrier recombination in nanostructures," *Nature nanotechnology*, vol. 7, no. 11, pp. 743–748, 2012.
- [117] H. Savin, P. Repo, G. Von Gastrow, P. Ortega, E. Calle, M. Garín, and R. Alcubilla, "Black silicon solar cells with interdigitated back-contacts achieve 22.1% efficiency," *Nature nanotechnology*, vol. 10, no. 7, pp. 624–628, 2015.
- [118] J. Hirsch, M. Gaudig, M. Gläser, S. Großer, N. Bernhard, and D. Lausch, "Industrial  $\text{Si}_x\text{N}_y$  surface passivation of maskless inductively coupled plasma (ICP) formed black-silicon without additional self-bias," in *31st European Photovoltaic Solar Energy Conference and Exhibition*, pp. 3–664, 2015.
- [119] K. Eriguchi, "Defect generation in electronic devices under plasma exposure: Plasma-induced damage," *Japanese Journal of Applied Physics*, vol. 56, no. 6S2, p. 06HA01, 2017.
- [120] E. Yablonovitch, D. Allara, C. Chang, T. Gmitter, and T. Bright, "Unusually low surface-recombination velocity on silicon and germanium surfaces," *Physical review letters*, vol. 57, no. 2, p. 249, 1986.
- [121] I. Oh, J. Kye, and S. Hwang, "Enhanced photoelectrochemical hydrogen production from silicon nanowire array photocathode," *Nano letters*, vol. 12, no. 1, pp. 298–302, 2012.
- [122] B. Sopori, X. Deng, J. Benner, A. Rohatgi, P. Sana, S. Estreicher, Y. Park, and M. Roberson, "Hydrogen in silicon: A discussion of diffusion and passivation mechanisms," *Solar Energy Materials and Solar Cells*, vol. 41, pp. 159–169, 1996.
- [123] M. Gaudig, J. Hirsch, J. Ziegler, T. Schneider, M. Werner, A. Sprafke, N. Bernhard, and R. B. Wehrspohn, "Investigation of the optoelectronic properties of crystalline silicon textured by maskless plasma etching at different ignition modes," in *29th European Photovoltaic Solar Energy Conference and Exhibition*, 2014.
- [124] M. J. Anderson and P. J. Whitcomb, *DOE simplified: practical tools for effective experimentation*. CRC press, 2016.

# Nomenclatures and Abbreviations

|              |                              |                |                            |
|--------------|------------------------------|----------------|----------------------------|
| $R$          | gas flow ratio               | $\omega$       | angular frequency          |
| $R_S$        | surface recombination rate   | $f$            | frequency                  |
| $T_S$        | substrate temperature        | $N_A$          | Avogadro number            |
| $T_A$        | annealing temperature        | $N$            | atom concentration         |
| $\beta$      | heating rate                 | $E_D$          | diffusion energy           |
| $\psi_S$     | surface potential            | $R_0$          | exponential decay constant |
| $\tau_{eff}$ | effective carrier lifetime   | $\Delta$       | wave phase                 |
| $t$          | time                         | $\psi$         | wave amplitude             |
| $e^-$        | electron, negatively charged | $A^+$          | acceptor                   |
| $h^+$        | hole, positively charged     | $D^-$          | donor                      |
| $n$          | electron density             | $Q$            | heat                       |
| $p$          | hole density                 | $\mu$          | chemical potential         |
| $n_i$        | intrinsic                    | $\Delta\sigma$ | sheet conductivity         |
| $G$          | generation rate              | $C$            | capacitance                |
| $E_g$        | band gap energy              | $V$            | voltage                    |
| $E_i$        | intrinsic energy             | $P$            | pressure                   |
| $E_C$        | conduction band energy       | $I$            | current                    |
| $E_V$        | valence band energy          | $v$            | volume                     |
| $k$          | Boltzmann constant           | $Z$            | impedance                  |
| $\Delta n$   | excess carrier density       | $n$            | refractive index           |
| $v_{th}$     | thermal velocity             | $k$            | extinction coefficient     |
| $\sigma$     | capture cross section        | $A$            | area                       |
| $D_{it}$     | interface defects            | $\mu_e$        | electron mobility          |
| $Q_f$        | fixed charges                | $\mu_p$        | hole mobility              |
| $d$          | film thickness               | $q$            | electron charge            |
| $D$          | diffusion coefficient        | $\alpha$       | absorption                 |
| $m$          | mass                         |                |                            |
| $\omega$     | wave number                  |                |                            |

## Abbreviations

|       |  |
|-------|--|
| PECVD | plasma enhanced chemical vapor deposition          |
| RIE   | reactive ion etching                               |
| RTA   | rapid thermal annealing                            |
| FTIR  | Fourier transform infrared                         |
| SE    | spectroscopic ellipsometry                         |
| SEM   | scanning electron microscope                       |
| NRA   | nuclear reaction analysis                          |
| DoE   | design of experiment                               |
| LeTID | light and elevated temperature induced degradation |
| ICP   | inductively coupled plasma                         |
| CCP   | capacitively coupled plasma                        |
| UN    | united nation                                      |
| IPCC  | intergovernmental panel on climate change          |
| PV    | photovoltaics                                      |
| HjT   | heterojunction                                     |
| ARC   | anti reflective coating                            |
| QSSPC | quasi-steady state photoconductance                |
| SRH   | Schockley Reed Hall                                |
| SRV   | surface recombination velocity                     |
| FZ    | float zone   |
| Cz    | Czochralski  |
| RCA   | radio corporation of America                       |
| RF    | radio frequency                                    |
| DC    | direct current                                     |
| AC    | alternative current                                |
| PVD   | physical vapor deposition                          |
| MIS   | metal insulator semiconductor                      |
| IR    | infrared   |
| PCD   | photoconductance decay                             |
| AM    | air mass   |
| DUT   | device under test                                  |
| HCUR  | high current                                       |
| LCUR  | low current  |
| HPOT  | high potential                                     |
| LPOT  | low potential                                      |
| RMS   | root mean square                                   |
| UHV   | ultra high vacuum                                  |
| QMS   | quadrapole mass spectroscopy                       |
| LT    | low temperature                                    |
| HT    | high temperature                                   |



|       |                                   |
|-------|-----------------------------------|
| SP    | sharp peak                        |
| SIMS  | secondary ion mass spectroscopy   |
| ERDA  | elastic recoil detection analysis |
| EMS   | effusion mass spectroscopy        |
| ANOVA | analysis of variance              |



# Acknowledgement

First and foremost, I would like to express my gratitude to my supervisors, Prof. Dr. Joerg Schilling, Prof. Dr. Ralf Wehrspohn, Dr. Dominik Lausch and Dr. Sylke Meyer, for their valuable guidance and feedback, their continuous support and their patience during my PhD study and the preparation of this dissertation.

I would like to express my special thanks to Dr. Dominik Lausch for his support and encouragement during this work. His immense knowledge and plentiful experience have encouraged me throughout this research. Without his support and trust, this work would not have been possible.

I would like to offer many thanks to Dr. Wolfgang Beyer for his kind support and valuable knowledge and experience during the establishment and development of the gas effusion mass spectroscopy.

I would also like to thank Dr. Maria Gaudig, Dr. Bodo Fuhrmann, Dr. Frank Heyroth, Dr. Jens Hirsch, Mr. Jansen Dwan, Mr. Marcus Gläser, Mr. Torsten Büchner, Dr. Marco John, Mrs. Alena Akhorsina, Dr. Paul Miclea, Dr. Stephan Krause, Dr. Volker Naumann, Dr. Susanne Richter, Mr. Stefan Eiternik, Mr. Michael Wendt, Mr. Stephan Hensel and Mr. Sebastian Timmel for laboratory support and advice during my study.

I also had great pleasure of working with Dr. Utkarsha Varshney and Prof. Dr. Bram Hoex from university of New South Wales (UNSW), Australia, Dr. Jonathan Steffens and Dr. Barbara Terheiden from university of Konstanz and Dr. Ujwall K. Das, Prof. Dr. Steve Hegedus, Prof. Dr. Birkmire and the wonderful group members at Institute of Energy Conversion (IEC), university of Delaware, the USA.

I would like to thank my friends and colleagues in Fraunhofer Center for Photovoltaics CSP. It is their friendship and support that turned my study and life in Halle (Saale) into a delightful time.

Last but not least, I would like to express my gratitude to my husband, Dominik, my parents, my parents in-law and my friends. Without their tremendous understanding and encouragement in the past few years, it would not be possible to complete my study.



# List of Publications

- S. Jafari, U. Varshney, B. Hoex, S. Meyer, D. Lausch, "Understanding Light-and Elevated Temperature-Induced Degradation in Silicon Wafers Using Hydrogen Effusion Mass Spectroscopy.", *IEEE Journal of Photovoltaics*, p. 1-7, 2021.
- S. Jafari, J. Steffens, M. Wendt, B. Terheiden, S. Meyer, D. Lausch, "Occurrence of Sharp Hydrogen Effusion Peaks of Hydrogenated Amorphous Silicon Film and Its Connection to Void Structures", *Journal of Physica Status Solidi PSS (b)*, 257(9), p. 2000097, 2020.
- S. Jafari, J. Hirsch, M. John, D. Lausch, N. Bernhard, S. Meyer, "Composition limited hydrogen effusion rate of a-SiN<sub>x</sub>:H passivation stack", *AIP Publishing LLC*, Vol. 2147, No. 1, p. 050004, 2019.
- U. K. Das, S. Jafari, S. Hegedus, "Si surface passivation by sulfur and reduction of interface defect recombination", *IEEE 7th World Conference on Photovoltaic Energy Conversion (WCPEC)(A Joint Conference of 45th IEEE PVSC, 28th PVSEC & 34th EU PVSEC)*, pp. 3076-3079, 2018.
- S. Jafari, C. Chaitanya, J. Hirsch, "Composition-Dependent Hydrogen Effusion and Diffusion Mechanism within a-SiN<sub>x</sub>:H", *Conference Proceedings 34th EUPVSEC*, p. 686 – 689, 2018.
- S. Jafari, M. Gläser, N. Bernhard, D. Lausch, "Effect of High Temperature Firing on the Bond Configuration and Composition of a-SiN:H Passivation Layer Deposited by PECVD", *Conference Proceedings 33rd EUPVSEC*, p. 553-556, 2017.
- M. Gläser, S. Jafari, M. Gaudig, J. Hirsch, D. Lausch, "Influence of Silicon Nitride Passivation Layers on the Kinetics of Boron Oxygen Degradation and Regeneration", *Visual presentation 32nd EUPVSEC*, June 2016.



# Curriculum Vitae

Name, Surname (Birth name): Sahar, Lausch (Jafari)

## Education

- 2017-present Physics, Ph.D., Martin-Luther University Halle-Wittenberg, Germany  
Thesis: Study the Effect of High Temperature Firing Process on Passivation Mechanism of Hydrogenated Amorphous  $SiN_x : H$  Layers with Focus on Hydrogen Effusion Measurements
- 2013-2016 Technology of Photovoltaic, M.Sc. Technical University of Ilmenau, Germany  
Thesis: Impact of co-firing process on passivation mechanism of  $SiN_x : H$  layer
- 2006-2010 Physics, B.Sc., Ferdowsi University of Mashhad, Iran

## Working experience

- 03.2021-present Physicist Battery development, NORCSi GmbH Battery company, Halle, Germany
- 03.2021-06.2021 Research Scientist, Martin-Luther university Halle-Wittenberg, Halle, Germany
- 12.2017-06.2020 Researcher Scientist, Fraunhofer Center for Photovoltaic CSP, Halle, Germany
- 07.2016-03.2020 Research Scientist, Anhalt University of Applied Sciences, Köthen, Germany
- 02.2018-05.2018 Research Scholar, University of Delaware, Newark, The USA
- 09.2015-06.2016 Student Assistant and Intern, Fraunhofer Center for Photovoltaic CSP, Halle, Germany
- 05.2015-08.2015 Project Assistant, Fraunhofer Institute for Electronic Nano-System ENAS, Chemnitz, Germany





# DECLARATION

Herewith I confirm that this thesis is entirely my own work and has been written without any help of others and that are used the mentioned sources and indicated all kind of citations correctly.

Hiermit erkläre ich, dass ich die vorliegende Arbeit selbstständig und ohne fremde Hilfe verfasst und andere als die von mir angegebenen Quellen und Hilfsmittel nicht benutzt und die den benutzten Werken wörtlich oder inhaltlich entnommenen Stellen als solche kenntlich gemacht habe.

Sahar Lausch geb. Jafari

Halle (Saale), October 11, 2023